Investigation of Low Lasing Threshold Organic Semiconductors and their Integration into Planar and Defect Microcavities

being a thesis submitted in fulfilment of the

requirements for the degree of

Doctor of

Philosophy

in the University of Hull & University of Sheffield

by

Peter J. Claronino

November 2023

I dedicate this thesis to my loving family who have supported me throughout my studies. A special feeling of gratitude to my sister, parents and Nana for always encouraging me to pursue my passions. Last and not least I am dedicating this to my incredible girlfriend Yan Chen, words cannot express all that you do for me and how amazing you are. I truly could not have done this without you, I love you so much.

Acknowledgements

Throughout my PhD I have had the pleasure of working with so many remarkable people, without whom I could have never finished this thesis. Their support and friendship have made this whole journey fun and unforgettable.

Firstly, I would like to offer my sincerest gratitude to both of my supervisors, Ali Adawi and David Lidzey, who have guided me throughout my PhD with their expertise and enthusiasm. A special thanks for Ali for giving me constant support, even during the pandemic with weekly meetings, and David for welcoming me into the EPMM group at Sheffield.

I thank Donatello Pagnotto, Rahul Jayaprakash and Kirsty Mcghee for training me in all fabrication techniques at both the University of Hull and the University of Sheffield. I truly appreciate your patience and kindness.

I also want to thank the wonderful, past and present members of the EPMM group. You have all been so welcoming and supportive; this PhD would not have been as fun without you all. In particular, I thank Timothy Thornber and Robert Gordon for all the evenings at the University Arms.

Front of Matter

Declaration of Originality

I declare that the work presented in this thesis is of my own original work undertaken at the University of Hull and the University of Sheffield between September 2019 and November 2023 under the supervision of Dr Ali Adawi and Professor David Lidzey. Any results and contributions from other researchers have been acknowledged for their work.

Peter Jose Claronino (November 2023)

Thesis Format

This thesis is composed of 7 chapters of which the experimental work, analysis and writing was primarily carried out by myself. The work on the material BN-PFO detailed in Chapter 4 and 6 has been published in *Journal of Materials Chemistry C* in collaboration with the University of Wuppertal. The manuscript of the publication has been reformatted and split between Chapters 4 and 6 with the supplementary information and additional data added to adapt to a thesis format. The contribution from each author is outlined below.

Experimental characterisation of materials, thin films and microcavities was performed by Peter Claronino[a,b], Rahul Jayaprakash[a], and Rachel C. Kilbride[c] under the supervision of David G. Lidzey[a]. BN-PFO was synthesized by Till Jessewitsch[d] under the supervision of Ullrich Scherf[e]. Data visualisation was performed by Peter Claronino and assisted by Timothy Thornber[a] and Robert D. J. Oliver[a]. Numerical simulations were calculated by Alina Muravitskaya[b]. The manuscript was written by Peter Claronino., Rachel C. Kilbride, Ali M. Adawi and David G. Lidzey, with all other authors contributing to its final version.

Affiliations

a. Department of Physics and Astronomy, The University of Sheffield, Hicks Building, Hounsfield Road, Sheffield S3 7RH, United Kingdom

b. Department of Physics and Mathematics, University of Hull, Robert Blackburn, Hull HU6 7RX, United Kingdom

c. Department of Chemistry, The University of Sheffield, Dainton Building, Brook Hill, Sheffield, S3 7HF, United Kingdom

d. Organic Functional Molecules, Organic Chemistry, University of Wuppertal, Gaußstrasse 20, 42119 Wuppertal, Germany

e. Macromolecular Chemistry Group and Wuppertal Center for Smart Materials & Systems (CM@S), Bergische Universität Wuppertal, Gauss-Strasse 20, 42119 Wuppertal, Germany

Publications and Conference Presentation

Publications

Peter Claronino, Rahul Jayaprakash, Till Jessewitsch, Rachel C. Kilbride, Timothy Thornber, Alina Muravitskaya, Robert D. J. Oliver, Ullrich Scherf, Jean-Sebastien G. Bouillard, Ali M. Adawi and David G. Lidzey "Organic copolymer lasing from single defect microcavity fabricated using laser patterning" J. Mater. Chem. C, 2023, Advance Article

Charalambos Louca, Armando Genco, Salvatore Chiavazzo, Thomas P. Lyons, Sam Randerson, Chiara Trovatello, **Peter Claronino**, Rahul Jayaprakash, Kenji Watanabe, Takashi Taniguchi, Stefano Dal Conte, David G. Lidzey, Giulio Cerullo, Oleksandr Kyriienko, Alexander I. Tartakovskii "Nonlinear interactions of dipolar excitons and polaritons in MoS2 bilayers" Nat. Commun, 2023

Maxim Makhonin, Anthonin Delphan, Tommi Isoniemi, **Peter Claronino**, Paul Walker, Maurice Skolnick, Alexander Tartakovskii, Dmitry Krizhanovskii, Kok Wee Song, Oleksandr Kyriienko, Konstantinos Orfanakis, Sai Kiran Rajendran, Hamid Ohadi, Manfred Bayer, Marc Assmann and Julian Heck otter "Nonlinear Rydberg exciton-polaritons in Cu2O microcavities", Light: Science & Applications (under review)

Conference Presentations

UK Semiconductors 2022, Sheffield – oral presentation

Abstract

This thesis presents a study into organic semiconductor laser materials and the design and fabrication of distributed Bragg reflector microcavities that can achieve low threshold lasing. A range of organic laser materials were investigated, where the molecular packing for each material was probed using X-ray scattering to understand the effect on the amplified spontaneous emission (ASE) threshold. It was found that increasing the concentration of a fluorescent dye (Fluorescent Orange) dispersed in an inert polystyrene matrix caused aggregation. This was observed by an increase in the molecular disorder and quenching, and at high concentrations, supressed ASE. The lowest threshold measured in solution processed Fluorescent Orange was 259 μJ cm^{-2}. This threshold was reduced to 55 μJ cm^{-2} by using co-thermal evaporation with BCP. The ASE for the copolymer BN-PFO was also explored where increasing the relative fraction of BN to PFO resulted in the increase in molecular disorder. This enhanced disorder led to a reduction in the ASE threshold to 19 μJ cm^{-2}. Finally, the lowest threshold (13.8 μJ cm^{-2}) measured was from the small molecule, BSBCz. The two lowest ASE threshold materials (BN-PFO 12.7% and BSBCz) were then integrated within planar microcavities to achieve low-threshold lasing (12 μJ cm^{-2} and 1.7 μJ cm^{-2}). This resulted in the lowest lasing threshold reported for a polymer microcavity. This record lasing threshold was reduced further by adding lateral confinement using laser patterning to write defects into the microcavity. This additional confinement resulted in a reduction in the lasing threshold from 11 μJ cm^{-2} to 7 μJ cm^{-2}. This laser patterning approach offers a quick and simple way to fabricate micro-scale organic lasers that have improved lasing thresholds and a four times enhancement in the Q factor.

Contents

List of Figures

List of Tables

Glossary of Acronyms

ADC - Analogue-to-digital converter

AFM - Atomic force microscope

ASE - Amplified spontaneous emission

BCP - Bathocuproine

BN - Binaphthyl

BSBCz - 2,4’-Bis(4-(9H-carbazol-9-yl)styryl)biphenyl

CBP - 4,4′ -Bis(N-carbazolyl)-1,1′ -biphenyl

CCD - Charge-coupled device

CFD - Constant function discriminator

CW - Continuous wave

DBR - Distributed Bragg reflector

DCM - Dichloromethane

DFB - Distributed feedback grating

FDTD - Finite-difference time-domain

FIB - Focused ion beam

FO - Fluorescent orange

FWHM - Full width half maximum

GIWAXS - grazing incidence wide-angle X-ray scattering

HOMO - Highest occupied molecular orbital

IC - Internal conversion

ISC - Intersystem crossing

LASER - Light amplification by stimulated emission of radiation

LED - Light emitting diode

LUMO - Lowest occupied molecular orbital

Nd:YAG - Neodymium-doped yttrium aluminium garnet

OLED- Organic light emitting diode

OSL - Organic semiconductor laser

PFO - Polyfluorene 2, 7-(9,9-dioctylfluorene

PGA - Programmable gain amplifier

PL - photoluminescence

PLQY - photoluminescence quantum yield

PMMA - Polymethyl methacrylate

PPV - Poly(p–phenylenevinylene)

PS - Polystyrene

QCM - Quartz-Crystal microbalance

RMS - root mean square

TAC - Time-to-amplitude converter

TCSPC - Time Correlated Single Photon Counting

TMM - Transfer Matrix Method

WGM - Whispering gallery mode

Chapter 1: Introduction

The application of lasing, since its first discovery in 1960 with a ruby laser [1], has been spread over a wide range of industries, where it is now essential for communication, medicine and measurement. Most lasers in circulation today are made from inorganic materials, however, organic semiconductors offer an attractive alternative. Organic semiconductors offer high optical gain, broad-tuneable emission and processability [2-4]. The high optical gain is due to the large absorption cross-sectional area of organic semiconductors, therefore, only a thin film a few hundreds of nanometres is required to achieve lasing. Organic semiconductor lasers (OSL) have therefore been an attractive area of research, and since the 60s, many key milestones have been achieved (shown in Table 1.1). One of the most significant discoveries being the organic light emitting diode (OLED) [5], that has revolutionised the display industry, asking the question of how organic semiconductors could change the commercial laser market?

Table 1.1: Milestones in the development of organic semiconductor lasers

Year	Discovery
1917	Stimulated emission proposed by Einstein [6]
1960	First reported laser, using ruby [1]
1967	First organic dye solid-state laser [7]
1972	First organic crystal laser [8]
1987	First OLED emitter [5]
1996	First organic semiconductor laser [9]
2008	LED pumped laser [10]
2011	First biological laser [11]
2017	continuous-wave organic laser [12]

2018	NIR TADF emitter [13]
2019	electrically pumped organic laser [14]
2023	OLED pumped organic laser [15]

OSL can either be excited optically or electrically, the latter being the most challenging as this requires electrical contacts and charge recombination in the gain layer. Additional absorption from electrical contacts, polarons and the formation of triplet states are detrimental to the lasing process [16]. Accounting for the losses associated with electrical pumping, the predicted lasing threshold exceeds 500 A cm^{-2} [17]. At such high current densities, Joule heating strongly affects the performance of the device [18, 19]. Currently there have been two approaches to overcome this: indirectly exciting by using an OLED [15], and directly exciting the gain medium, which has good triplet management, with high charge densities created by reducing the size of the device [14]. This exceptional triplet management is another important breakthrough for OSL [12], as triplets can also be generated through optical pumping via intersystem crossing under continuous wave operation [20]. The material used for direct electrical excitation is one of the few organic semiconductors that has demonstrated quasi-continuous wave operation under optical pumping. However, this limits the wavelength tunability for this device as only this material has been reported for direct pulsed electrical excitation. Indirect operation has the benefit of being able to change the gain layer with other materials that have absorption overlapping the emission of the OLED. Additionally, OLEDs with high brightness are possible for a wide range of wavelengths.

Both reports for electrical operation use distributed feedback gratings (DFG) as the resonator as this structure has widely reported low-threshold lasing. The next challenge to overcome for electrical operation is the long-term stability of the OSL device. Both indirect and direct operation require high charge density to work above the lasing threshold. Another resonator architecture that has yet to successfully claim electrical operation is the microcavity, despite the planar structure of a microcavity favouring the stacked structure of an OLED. Planar microcavities are well known for their vertical confinement, however lasing from modified microcavities that also offer lateral confinement has not been so extensive.

1.1 Thesis Outline

Chapter 2 provides the background theory behind the work undertaken in this project. The basic structure of organic semiconductors is explained, describing how orbital hybridisation leads to the conjugation of an organic molecule. This electron delocalisation across the molecular backbone of the compound gives rise to the optical properties of organic semiconductors. These optical transitions made possible provide multiple energy levels that can support a population inversion and therefore, allow amplified stimulated emission. This stimulated emission enhanced with a resonator structure forms a laser. Finally, this chapter covers the different resonator architectures that have been used for optically pumped organic lasers.

Chapter 3 covers the experimental methods and techniques used to fabricate and characterise all the samples used in this study. Starting with basic cleaning procedures and deposition techniques, then detailing the setups used for optical characterisation.

Chapter 4 is the first experimental results chapter, where a range of organic compounds were characterised using an amplified spontaneous emission setup. The materials investigated were a pigment dye dispersed in a matrix, a copolymer (BN-PFO), and a small molecule (BSBCz). The amplified spontaneous emission behaviour of the films was corroborated with their morphology by probing with X-ray scattering. Using this, the optimal composition of each material was found by measuring the ASE threshold. From this, two materials that gave the lowest ASE thresholds were identified.

Chapter 5 continues the study on the two materials that showed the lowest ASE thresholds from Chapter 4 (BN-PFO 12.7% and BSBCz). Here the two materials were integrated into two planar microcavities to investigate their lasing behaviour. Transfer matrix modelling was used to optimise the design of the cavities before fabrication. The lasing performance of the two microcavities is compared with an added section including OLED performance to see which material offers more promise for electrical operation. The lasing thresholds for BN-PFO 12.7% and BSBCz were 12 and 1.5 μJ cm^{-2} respectively. Compared to the literature (17 μJ cm^{-2}) [21], BN-PFO 12.7% was observed to have the lowest polymer microcavity lasing threshold. The lasing threshold for BSBCz measured was comparable to previously reported microcavity that used a CBP matrix (1.7 μJ cm^{-2}) [22].

Chapter 6 describes a laser patterning technique that writes defect structures into a polystyrene film. By using a laser focused through an objective, micro-dimples are melted into the polystyrene film, creating a Gaussian shaped defect. Growing the microcavity structure used in Chapter 4 on top of the defects, allows the whole structure to conform to the Gaussian profile. Therefore, the defect profile is also apparent in the active layer of the microcavity. This provides additional confinement and reduces the mode volume of the resonator, causing a decrease in the lasing threshold to 7 μJ cm^{-2}. This is comparable to other organic micro lasers that report thresholds of 20 μJ cm^{-2} and 4.2 μJ cm^{-2} with the latter having more complicated fabrication involving e-beam lithography and focused ion beam [23, 24].

Chapter 7 provides a summary of all the work that is detailed in the thesis and discusses ideas of the future work.

1.2 References

[1] M. T. H., “Stimulated emission of radiation in ruby,” Nature, vol. 187, pp. 493–494, 1960

[2] I. D. W. Samuel and G. A. Turnbull, “Organic semiconductor lasers,” Chem. Rev., vol. 107, no. 4, pp. 1272–1295, Apr. 2007, doi: 10.1021/CR050152I/ASSET/IMAGES/LARGE/CR050152IF00022.JPEG.

[3] F. Chen, D. Gindre, and J.-M. Nunzi, “Tunable circularly polarized lasing emission in reflection distributed feedback dye lasers,” Opt. Express, vol. 16, no. 21, p. 16746, Oct. 2008, doi: 10.1364/OE.16.016746.

[4] L. Zhou et al., “Screen-Printed Poly(3,4-Ethylenedioxythiophene):Poly(Styrenesulfonate) Grids as ITO-Free Anodes for Flexible Organic Light-Emitting Diodes,” Adv. Funct. Mater., vol. 28, no. 11, p. 1705955, Mar. 2018, doi: 10.1002/adfm.201705955.

[5] C. W. Tang and S. A. Vanslyke, “Organic electroluminescent diodes,” Appl. Phys. Lett., vol. 51, no. 12, pp. 913–915, Sep. 1987, doi: 10.1063/1.98799.

[6] A. Landé, “Zur Quantentheorie der Strahlung,” Zeitschrift für Phys., vol. 35, no. 5, pp. 317–322, 1926, doi: 10.1007/BF01380146.

[7] B. H. Soffer and B. B. McFarland, “continuously tunable, narrow - band organic dye lasers,” Appl. Phys. Lett., vol. 10, no. 10, pp. 266 - 267, May 1967, doi: 10.1063/1.1754804.

[8] N. Karl, “Laser emission from an organic molecular crystal,” Phys. Status Solidi, vol. 13, no. 2, pp. 651–655, Oct. 1972, doi: 10.1002/PSSA.2210130237.

[9] G. Canazza, F. Scotognella, G. Lanzani, S. De Silvestri, M. Zavelani-Rossi, and D. Comoretto, “Lasing from all-polymer microcavities,” Laser Phys. Lett., vol. 11, no. 3, p. 035804, Mar. 2014, doi: 10.1088/1612-2011/11/3/035804.

[10] Y. Yang, G. A. Turnbull, and I. D. W. Samuel, “Hybrid optoelectronics: A polymer laser pumped by a nitride light-emitting diode,” Appl. Phys. Lett., vol. 92, no. 16, pp. 2006–2009, 2008, doi: 10.1063/1.2912433.

[11] M. C. Gather and S. H. Yun, “Single-cell biological lasers,” Nat. Photonics 2011 57, vol. 5, no. 7, pp. 406–410, Jun. 2011, doi: 10.1038/nphoton.2011.99.

[12] A. S. D. Sandanayaka et al., “Toward continuous-wave operation of organic semiconductor lasers,” Sci. Adv., vol. 3, no. 4, pp. 1–8, 2017, doi: 10.1126/sciadv.1602570.

[13] D. H. Kim et al., “High-efficiency electroluminescence and amplified spontaneous emission from a thermally activated delayed fluorescent near-infrared emitter,” Nat. Photonics 2018 122, vol. 12, no. 2, pp. 98–104, Jan. 2018, doi: 10.1038/s41566-017-0087-y.

[14] A. S. D. Sandanayaka et al., “Indication of current-injection lasing from an organic semiconductor,” Appl. Phys. Express, vol. 12, no. 6, p. 061010, Jun. 2019, doi: 10.7567/1882-0786/ab1b90.

[15] K. Yoshida, J. Gong, A. L. Kanibolotsky, P. J. Skabara, G. A. Turnbull, and I. D. W. Samuel, “Electrically driven organic laser using integrated OLED pumping,” Nat. 2023 6217980, vol. 621, no. 7980, pp. 746–752, Sep. 2023, doi: 10.1038/s41586-023-06488-5.

[16] J. Clark and G. Lanzani, “Organic photonics for communications,” Nat. Photonics, vol. 4, no. 7, pp. 438–446, Jul. 2010, doi: 10.1038/nphoton.2010.160.

[17] C. Karnutsch et al., “Improved organic semiconductor lasers based on a mixed-order distributed feedback resonator design,” Appl. Phys. Lett., vol. 90, no. 13, pp. 1–4, 2007, doi: 10.1063/1.2717518.

[18] K. Yoshida, T. Matsushima, Y. Shiihara, H. Kuwae, J. Mizuno, and C. Adachi, “Joule heat-induced breakdown of organic thin-film devices under pulse operation,” J. Appl. Phys., vol. 121, no. 19, p. 195503, May 2017, doi: 10.1063/1.4983456/13180762/195503_1_ACCEPTED_MANUSCRIPT.PDF.

[19] K. Hayashi et al., “Suppression of roll-off characteristics of organic light-emitting diodes by narrowing current injection/transport area to 50 nm,” Appl. Phys. Lett., vol. 106, no. 9, 2015, doi: 10.1063/1.4913461.

[20] N. C. Giebink and S. R. Forrest, “Temporal response of optically pumped organic semiconductor lasers and its implication for reaching threshold under electrical excitation,” Phys. Rev. B - Condens. Matter Mater. Phys., vol. 79, no. 7, pp. 1–4, 2009, doi: 10.1103/PhysRevB.79.073302.

[21] A. Palatnik and Y. R. Tischler, “Solid-State Rhodamine 6G Microcavity Laser,” IEEE Photonics Technol. Lett., vol. 28, no. 17, pp. 1823–1826, Sep. 2016, doi: 10.1109/LPT.2016.2573200.

[22] Y. Hu, F. Bencheikh, S. Chénais, S. Forget, X. Liu, and C. Adachi, “High performance planar microcavity organic semiconductor lasers based on thermally evaporated top distributed Bragg reflector,” Appl. Phys. Lett., vol. 117, no. 15, p. 153301, Oct. 2020, doi: 10.1063/5.0016052.

[23] M. Sudzius, M. Langner, S. I. Hintschich, V. G. Lyssenko, H. Fröb, and K. Leo, “Multimode laser emission from laterally confined organic microcavities,” Appl. Phys. Lett., vol. 94, no. 6, p. 061102, Feb. 2009, doi: 10.1063/1.3080689.

[24] P. B. Deotare, T. S. Mahony, and V. Bulović, “Ultracompact Low-Threshold Organic Laser,” ACS Nano, vol. 8, no. 11, pp. 11080–11085, Nov. 2014, doi: 10.1021/nn504444g.

Chapter 2: Theoretical Background

The first organic semiconductor laser was discovered in 1992 by Moses [1], where a conjugated polymer was used as the active layer. Later in 1996, lasing from an optically pumped organic microcavity was claimed by Tessler [2]. To this day, the predominant method of achieving lasing from an organic semiconductor is through optical pumping [3-5]. Another method of excitation is through electrical excitation [6, 4], which has been demonstrated indirectly through OLED pumping [7]. In this chapter, we explain the semiconducting properties of organic materials, leading to their application as a lasing medium. This starts with the hybridization of orbitals, leading to the formation of π-π^* bonds that delocalize charge over the molecule and establish the HOMO and LUMO energy levels. Energy transfer between the HOMO and LUMO allows the optical transitions essential for lasing.

2.1 Organic Semiconductors

Materials composed of carbon atoms that are bonded together are defined as an organic material. Carbon is at the centre of all organic materials, and it is this unique bonding of carbon atoms that enables their electronic and optical properties. Hydrogen and other heteroatoms can also bond to this carbon structure and can change the electrical and optical properties. These compounds can form long chains called polymers or shorter chains called monomers. The arrangement of the carbon bonds along the chain and the addition of other heteroatoms leads to an almost endless number of molecular configurations that have unique optical properties [8].

2.1.1 The Semiconducting Properties of an Organic Molecule

Atomic orbitals are central to the understanding of the semiconducting properties of organic materials. The location of electrons around a central nucleus is determined by a set of four quantum numbers (*n, l, m and s*) and the Pauli Exclusion Principle. The principal quantum number (*n*) takes a positive, non-zero integer number (1, 2, 3 …) that describes the energy of the electron and therefore the size of the orbital. The angular momentum quantum number (*l*) can take the value 0, 1, 2 … (*n* – 1) where this defines the shape of the orbital. The orbital shape is normally given in its letter notation *s, p, d, f* … an example of the *s* and *p* orbitals is given in Figure 2.1ab. The magnetic quantum number (m_l), which takes the integer value (*-l, …, 0, …, +l*) specifies the orientation of the orbital, as shown in Figure 2.1b where the *p*-orbital can take three different orientations. The spin quantum number ($m_s = \pm 1/2$) allows two possible states: one where the spin is 'up' or one where it is 'down'. This

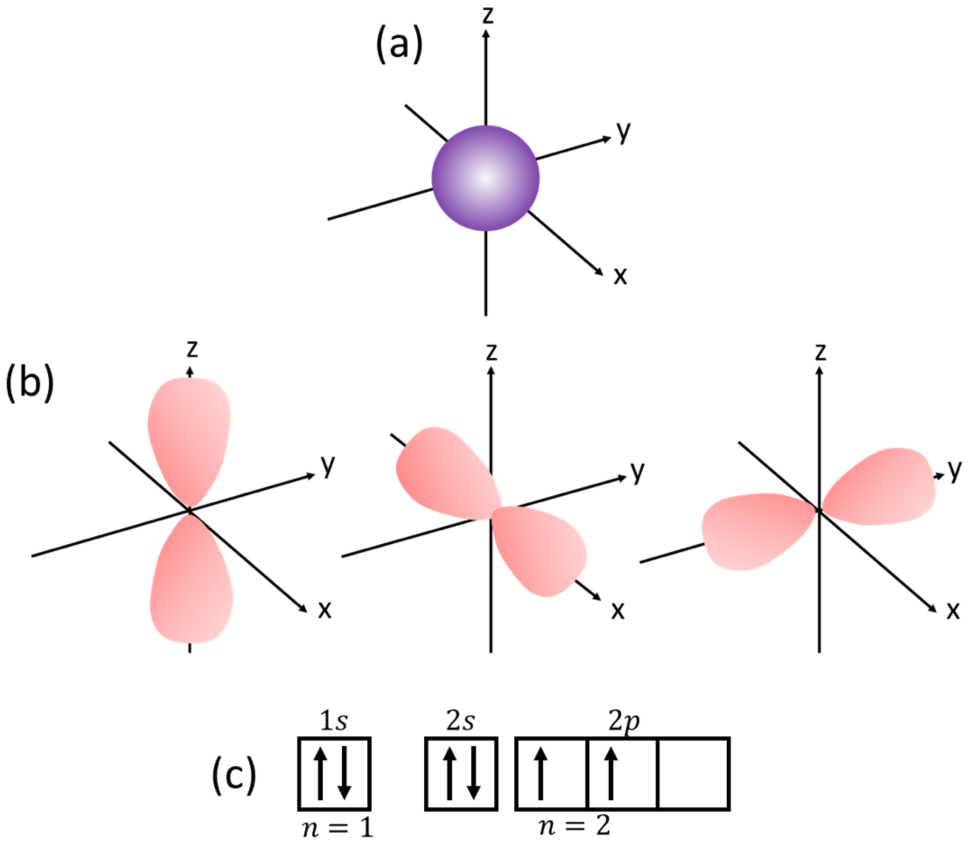

Figure 2.1: Orbital shapes given by the angular momentum quantum number (a) 0→*s* and (b) 1→*p* (c) the electron configuation for a single stable carbon atom, where the principle and orbital quantum numbers are given. The direction of the arrow also give the spin of the electrons.

spin quantum number reflects the Pauli Exclusion Principle which states that two electrons cannot exist in the same quantum state in the same quantum system.

The semiconducting property of organic molecules is due to the arrangement of the electron orbitals across the carbon chain. This originates from the hybridization of orbitals to conform to new bonding geometries. There are three different forms of hybridization that carbon can form, the ground state configuration of a carbon atom (shown in Figure 2.1c) where two core electrons occupy the 1*s* orbital, and the four left over are the valence electrons that occupy the 2*s* and 2*p* orbitals can be expressed as:

$$1s^2 2s^2 2p^2$$

Due to the Pauli exclusion principle the electrons in the 1*s* and 2*s* orbitals are paired or also referred to as antiparallel. The 2*p* electrons are unpaired and are free to form bonds and when a carbon atom bonds it stabilizes with as many bonds as possible. To form more bonds, electrons in the 2*s* orbital can hybridize following Hund's rule to create a new *sp* orbital. Additional electrons from the 2*s* orbital can hybridize to form multiple *sp* orbitals with the following electron configuration:

$$1s^2 sp^3$$

$$1s^2 sp^2 2p_x^1$$
$$1s^2 sp^1 2p_x^1 p_y^1$$

The corresponding orbital arrangement for the above electron configurations is presented in Figure 2.2 in which the orbitals occupy the space that experiences the least repulsion and therefore this is their most stable form.

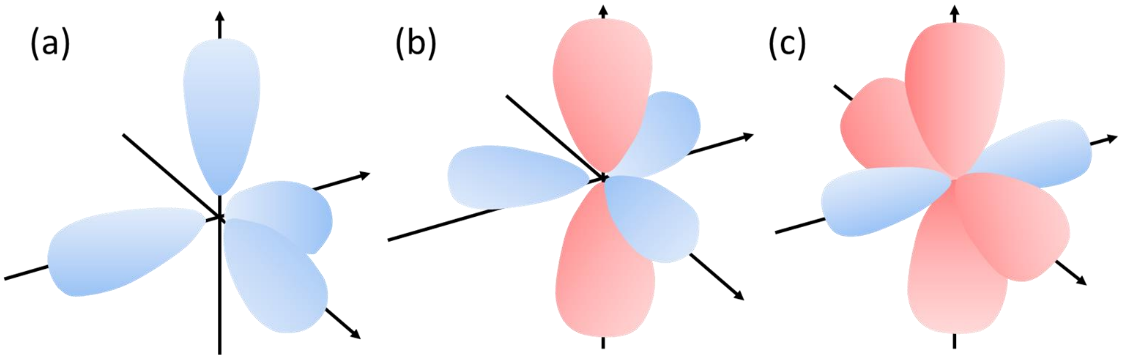

Figure 2.2: Electron orbitals for the hybridization of a carbon atom for different bonding cases: (a) four sigma bonds (*sp*³ hybridization) (b) three sigma bonds (*sp*² hybridization) (c) two sigma bonds (*sp* hybridization).

When bonding to a neighbouring carbon or hydrogen atom, the hybridized *sp* orbitals overlap and form a sigma bond (σ). This sigma bond occupies the space between the bonding atoms and has cylindrical symmetry around the internuclear axis [9]. The carbon atom will hybridize the number of *sp* orbitals to match the number of bonds. For the case of ethylene (shown in Figure 2.3), there will be three sigma bonds per carbon atom, two bonds to hydrogen and one to the other carbon atom. The remaining *p* orbitals will be orthogonal to the sigma bonding plane. These *p* orbitals do not have symmetry around the internuclear axis

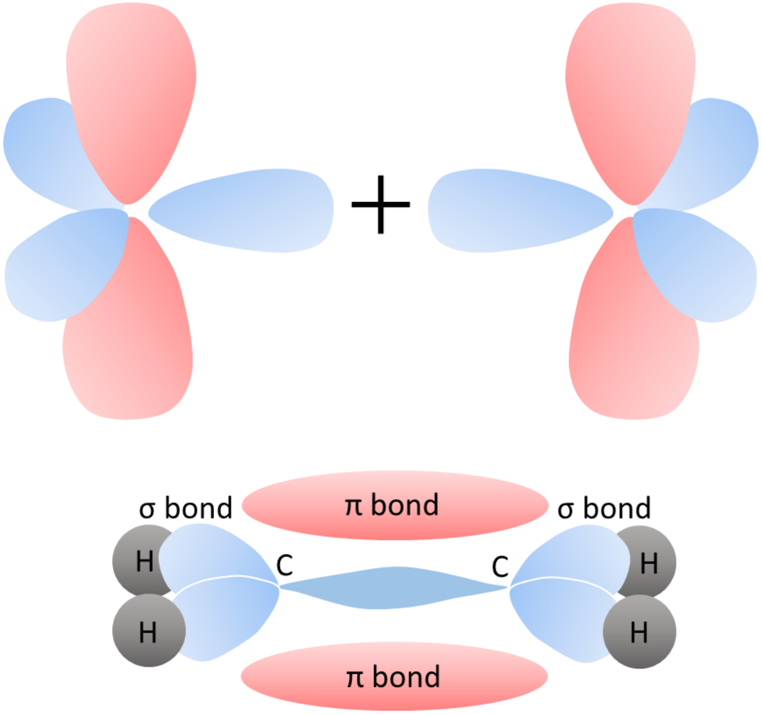

Figure 2.3: Two *sp*² hybridized carbon atoms bonding together to form ethene molecule. Here two π bonds are formed and a single sigma bond.

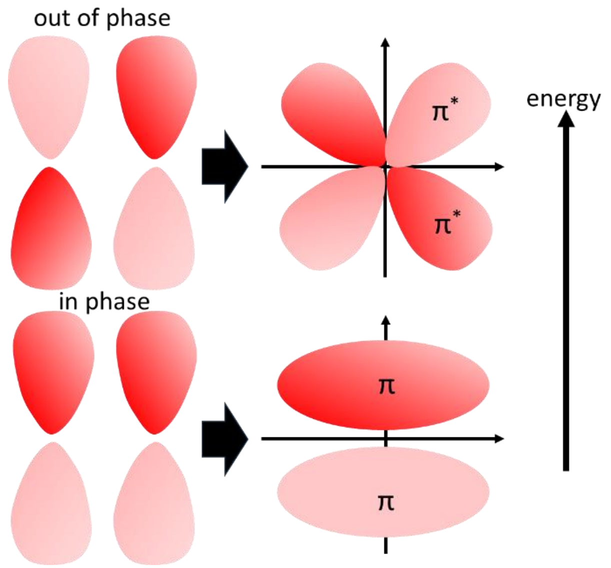

Figure 2.4: In phase bonding (π orbital) and out of phase antibonding (π^* orbital). The energy for the antibonding orbitals is higher than the in-phase case.

and therefore overlap to form a π -bond (or π orbital), and the two carbon atoms are said to be double-bonded. This delocalizes the electron from a single atom over the molecule, giving the molecule semiconducting properties [10, 11]. If this bonding is repeated over a longer carbon chain, then the delocalization will extend over the whole molecule. Examples for *sp* and sp^3 hybridization can be seen in ethane (C_2H_6) and acetylene (C_2H_2) respectively. The bonds formed in ethane are therefore sigma bonds, whereas acetylene has a triple bond between the two carbon atoms.

When two orbitals overlap to form a bond, it must follow that the number of starting orbitals equals the number of bonding orbitals. Above we see the bonding case, but the second possible orbital is the antibonding case (π* orbital), shown in Figure 2.4 [12]. These two bonding and antibonding cases have different energy levels, the bonding being the lowest energy and therefore most likely to be occupied (HOMO), and the antibonding having the highest energy and therefore the least likely occupied (LUMO). In the ground state, only the bonding orbital will be occupied as its energy is lower than the starting 2p orbitals. The difference between the LUMO and HOMO is the band gap and for organic semiconductors ranges between 2 to 5 eV [13].

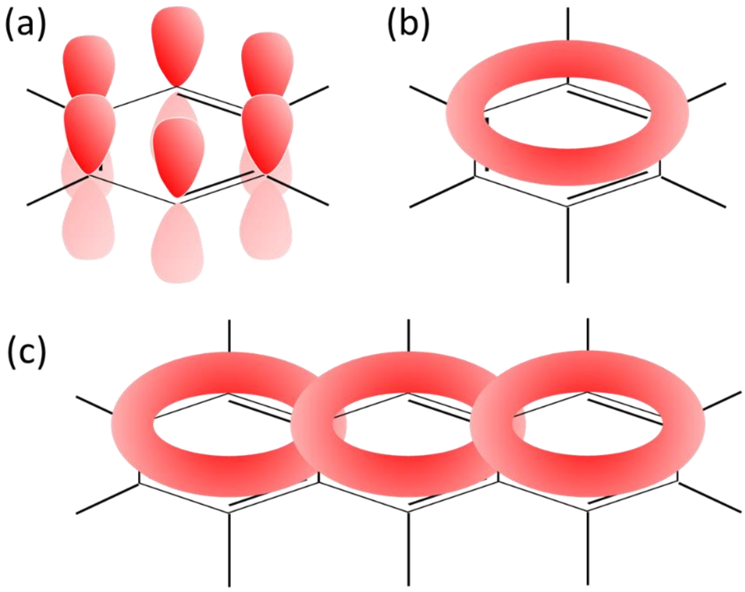

Figure 2.5: (a) *p* orbital orientation for a benzene ring (b) Delocalisation due to overlapping p-orbitals (c) Delocalisation over a whole molecule of anthracene.

For a conjugated molecule with multiple bonded atoms that have different bonding and antibonding orbitals, there will be different energy levels over the molecule. This will widen the energy possible for the bonding and antibonding orbitals. Generally, the longer the chain the wider the energy levels. At 0K the highest molecular orbital that contains electrons is called the HOMO and the lowest molecular orbital that has no electrons is called the LUMO. For a conjugated molecule, the carbon backbone chain will form alternating single and double bonds in which a common structure is likely found called the benzene ring. Figure 2.5a illustrates that around the ring six carbon atoms are bonded in which six *p* orbitals are above and below the molecular plane. These orbitals overlap in Figure 2.5b to form π bonds that delocalize the electrons around the benzene ring. The molecule anthracene is shown in Figure 2.5c and is made from three of these benzene rings that allow electrons to delocalize across the whole molecule.

When an electron is excited to the LUMO, only two electrons can occupy π-π* orbitals and therefore only four electron spin configurations ned to be considered, where an electron is either in the spin up or spin down ($\uparrow\uparrow, \uparrow\downarrow, \downarrow\uparrow, \downarrow\downarrow$). This gives rise to two different states where the electron pair is symmetric or antisymmetric under particle exchange, called the triplet and

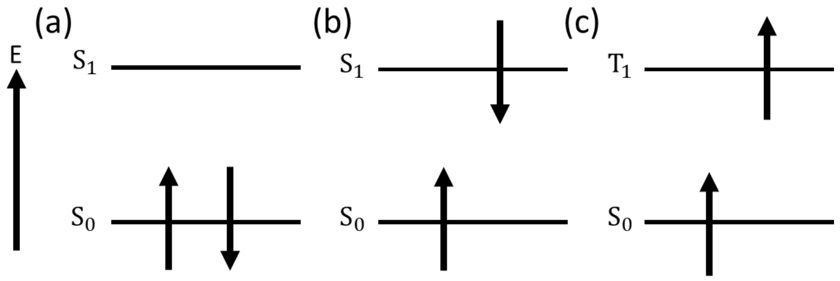

Figure 2.6: Electron spin configuration for (a) singlet ground state (b) singlet excited state (c) triplet excited state. S_0 represents the HOMO energy level and S_1 and T_1 the LUMO. For both singlet cases the two electron spins are antisymmetric (arrows point the opposite direction). The electrons in the triplet state are symmetric, so for the electron to relax back to the ground state, the spin must flip.

singlet state (shown in Figure 2.6). Spin is a quantum number of ½ where the sign of spin is either positive or negative depending on the direction of the angular momentum that can be projected onto the z-axis and is represented as an up or down arrow. When the electron pair is symmetric, the total spin angular momentum is equal to one and is therefore in the triplet state in which there are three possible combinations:

$$T\ (Triplet) \Rightarrow 1 = \begin{cases} |1,1\rangle = \uparrow\uparrow \\ |1,0\rangle = \dfrac{1}{\sqrt{2}}(\uparrow\downarrow + \downarrow\uparrow) \\ |1,-1\rangle = \downarrow\downarrow \,\} \end{cases} \tag{2.1}$$

For the antisymmetric case, the total spin angular momentum is equal to zero and is therefore in the singlet state in which there is one possible combination:

$$|0,0\rangle = \frac{1}{\sqrt{2}}(\uparrow\downarrow - \downarrow\uparrow)\} \Rightarrow S = 0\ (Singlet) \tag{2.2}$$

The ground state of a molecule resides in the HOMO and therefore the two electrons in this orbital must obey the Pauli exclusion principle by forming a singlet state. There are rare cases where the ground state is a triplet, for example, oxygen which has two symmetric electrons in the 2*p* orbital.

2.1.2 Exciton

An exciton is classified as a quasiparticle, formed by the combination of an electron and a hole that is bound through the coulombic force. An exciton can diffuse between molecules and separates it from the definition of just an excited state. It can be formed by exciting an electron from the HOMO to the LUMO where the electron and the vacant hole left behind are paired. This is typical for an optical excitation. In the case of electrical excitation, charge is injected, and the electrons and holes move to occupy the same molecular site where the exciton can be formed.

There are two types of excitons (shown in Figure 2.7), one for electron-hole binding in inorganic semiconductors (Wannier-Mott exciton) and the other for organic semiconductors (Frankel exciton) [14-16]. The main difference between the two is the binding energy between the electron and the hole pair. As inorganic semiconductors generally have a larger dielectric constant (ϵ_r) compared to organics, the following equation shows that this decreases the binding energy (E_b).

$$E_b = \frac{e^2}{4\pi\epsilon_0\epsilon_r d_{e-h}} \tag{2.3}$$

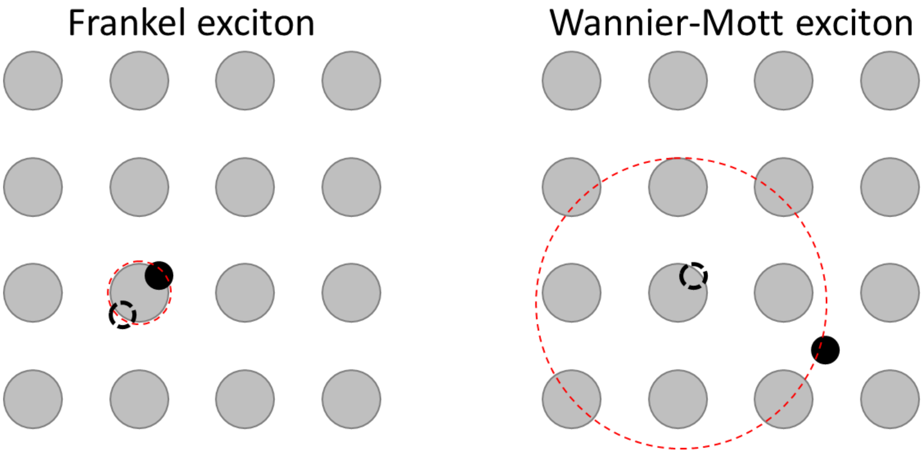

Figure 2.7: Simplified exciton illustration for an organic and inorganic semiconductor. Here the hole is a dashed circle and electron solid circle. The Frankel exciton (left) has a strongly bound electron-hole pair whereas the Wannier-Mott exciton (right) hole-pair are bound across the lattice.

This equation is similar to the energy level equation for the Bohr model of the atom. For inorganics, the large radius spans across multiple atoms and the excitons are not bound to a specific site. As for organics, the exciton radius is strongly confined within a single molecule, however, a combination between the Wennier-Mott and Frenkel exciton is possible for organics called a charge transfer exciton, in which the electron and hole are separated between two separate molecules.

2.1.3 Optical Transitions

For organic semiconductors, optical transitions occur between the HOMO and the LUMO energy levels. The ground state being the lowest energy level (HOMO) is denoted with S_0 and the first excited state given by S_1. Absorption occurs when a photon with energy equivalent to the band gap excites an electron from the S_0 to the S_1 state (shown in Figure 2.8a). An excited state can spontaneously emit a photon with energy equivalent to the transition back to the S_0 state. This spontaneous emission is illustrated in Figure 2.8b. Similar to how an incident photon can induce absorption, a photon can also stimulate an excited state to emit. Figure 2.8c illustrates that the incident photon continues to propagate with the emitted photon and they have identical momentum and frequency. This is the fundamental process for achieving lasing.

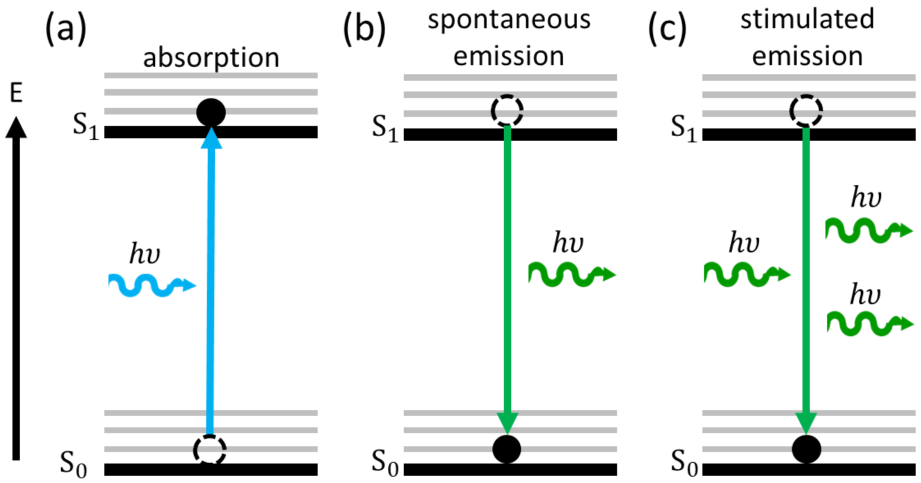

Figure 2.8: Optical transitions: (a) absorption, (b) spontaneous emission, and (c) stimulated emission.

2.1.3.1 Jablonski Diagram

A more realistic model of the optical transitions considers the singlet and triplet energy levels, including the radiative and non-radiative processes. Figure 2.9 shows a typical Jablonski diagram that clearly illustrates all transitions possible in an organic molecule. These molecules have vibrational and rotational sub-energy levels that allow for additional transitions with no photon emission. Another non-radiative process that occurs within the higher energy singlet and triplet states is internal conversion (IC). As given by Kasha's rule [17], emission is dominated by the $S_1 - S_0$, therefore, energy relaxation in higher energy states is typically non-radiative. Not all non-radiative transitions occur between the same spin states, it is possible for a singlet state to become a triplet state via spin-orbit coupling. This is known as intersystem crossing (ISC). As optical excitation conserves the spin, triplets are not created directly through optical pumping. Therefore, for optical excitation triplet states are primarily populated from ISC.

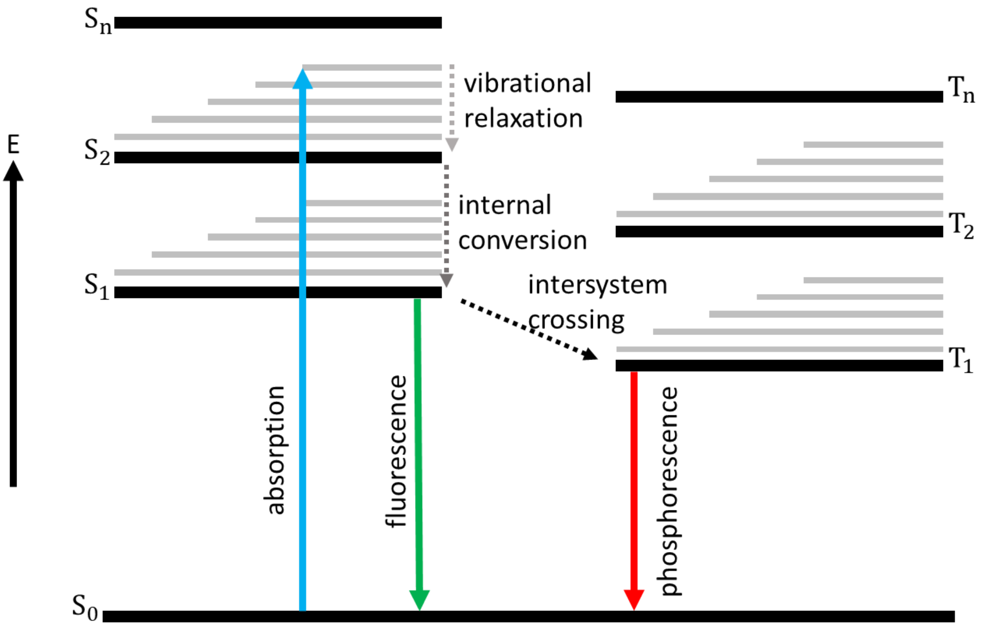

Figure 2.9: Jablonski diagram illustrating the energy states and transitions between them for an organic molecule. Absorption (blue arrow), fluorescence (green arrow) and phosphorescence (red arrow). The non-radiative processes are denoted with curly arrows.

Table 2.1: Radiative and non-radiative transition lifetimes for organic semiconductors.

Transitions	**Lifetime (s)**
Absorption	10^{-15} [18]
Fluorescence	10^{-8} [19]
Phosphorescence	10^{-5} [20]
Vibronic relaxation	10^{-12} [18]
Internal conservation	10^{-11} [18]
Intersystem crossing	10^{-6} [21]

Table 2.1 shows the approximate lifetime for each radiative and non-radiative process. The absorption process happens on a timescale of 10^{-15} s where an electron in the ground state is excited to a higher energy singlet state. This excited state can take multiple paths for deexcitation. If the electron is promoted to a singlet state higher than S_1, it will relax to the lowest vibrational level of that state in the order of 10^{-11} s through intersystem conservation. It can then emit a photon to return to the ground state S_0 (10^{-8} s) or spin-flip to a triplet state where the time for intersystem crossing is of the order of 10^{-6} s. This triplet state can then relax to its lowest vibrational state (T_1), before it then flips its spin to return to the ground state (10^{-5} s). This process has a longer lifetime when compared to fluorescence, due to the multiple spin flips and is called phosphorescence [22]. Fluorescence is a more efficient process where the transition occurs directly from the S_1 to S_0. The radiative and non-radiative transitions control the total emission lifetime of a molecule (τ_{PL}) and can be expressed using the following equation:

$$\tau_{PL} = \frac{1}{k_{rad} + k_{nrad}} \tag{2.4}$$

Where k_{rad} is the radiative decay rate, and k_{nrad} is the non-radiative decay rate. Taking the ratio between these two values represents the ratio between the number of photons emitted and the number of photons absorbed [23]. This ratio is called the photoluminescent quantum yield (ϕ_{PLQY}):

$$\phi_{PLQY} = \frac{k_{rad}}{k_{rad} + k_{nrad}} \tag{2.5}$$

The photoluminescence quantum yield is typically given as a percentage and is a measure of how efficient a material can absorb and re-emit a photon. If $\phi_{PLQY} = 100\ \%$ then every photon that is absorbed creates an exciton that decays radiatively.

2.1.3.2 Stokes Shift

The Stokes Shift refers to the red shift in the emission from the absorption wavelength and for organic molecules this Stokes Shift is relatively large. This shift to a lower energy wavelength suggests that energy is lost via relaxational processes such as vibration and rotation of the molecules. Figure 2.10 shows the Franck-Condon principle which gives a more detailed explanation for this [24-26]. This model uses the Born-Oppenheimer approximation and therefore assumes that the nucleus is stationary when compared to the fast movement of the bound electrons. The potential energy of the electrons as a plot against nuclear radius in Figure 2.10 is simplified for a diatomic molecule where the S_1 (LUMO) state has a higher energy and nuclear position due to the antibonding orbital. The S_0 (HOMO) state represents the ground state and therefore the bonding case for the molecule. The vibrionic energy levels for each of the energy levels is represented with the corresponding wavefunction. Optical transitions are most likely to happen when the wavefunctions of the two vibrational energy levels have the most overlap between them, and therefore the probability of the transition is indicated by the normalized intensity of the absorption and emission. Due to the nuclear coordinate shift of the S_1 excited state, the most likely transition occurs from the lowest vibrational energy level in S_0 to a higher vibrational in S_1. This transition is represented vertically as the time it takes for the photon to be

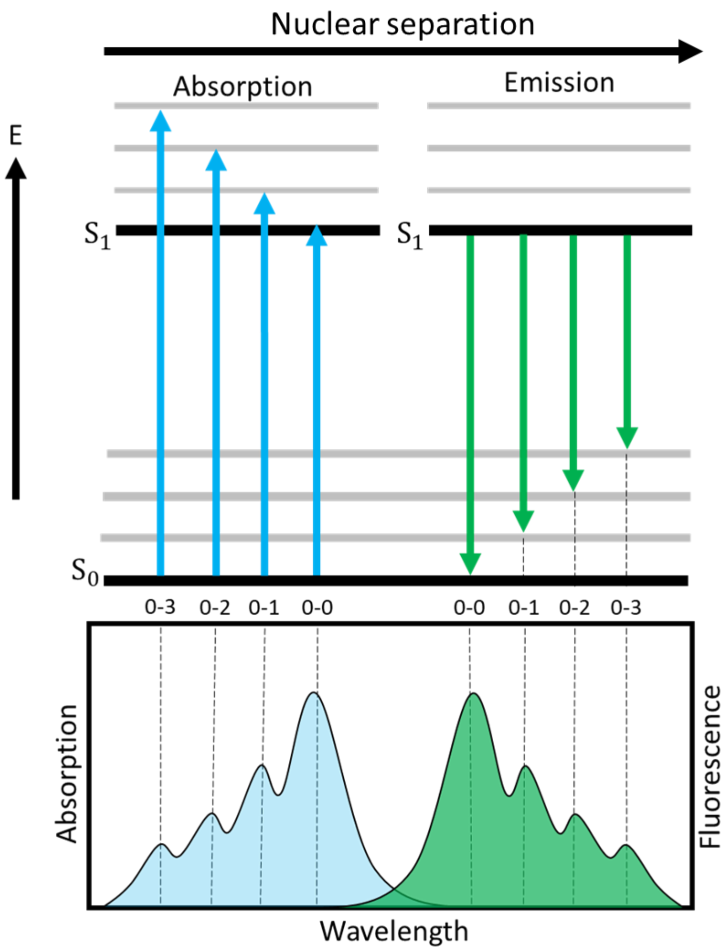

Figure 2.10: Stoke Shift for an organic semiconductor where the emission (green) and absorption (blue) spectra are characteristic of the transition between the S_1 and S_0 states. The vibronic sublevels create multiple transitions that correspond to the separate peaks in the spectra.

absorbed is 10^{-15} s, whereas the relaxation of a molecule to the lowest vibrational energy level takes 10^{-12} seconds. For emission the S_1 excited state must relax into the lowest vibrational energy state before any further transition into the ground state S_0.

2.2 Organic Semiconductor Lasers

2.2.1 Laser Basics

Lasing is the amplification of light through the process of stimulated emission. The amplification of the light happens inside a gain medium that increases the intensity of the output light. Most lasers are composed of three components, a pump source, gain medium

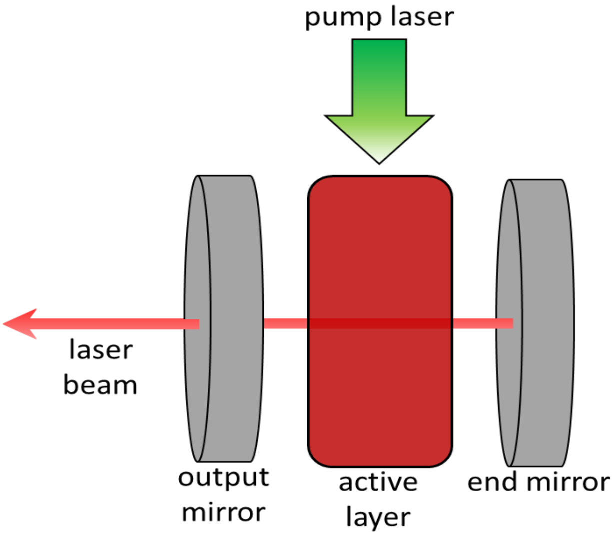

Figure 2.11: Basic optically pumped laser construction consisting of an active layer placed between two mirrors, that is pumped by an external laser.

and a feedback mechanism (Figure 2.11) [3]. The pump source excites the gain medium to sustain amplification, and the feedback mechanism directs the light back into the gain medium for increased amplification. The gain medium is where stimulated emission takes place and is responsible for amplification.

Three optical transitions occur inside the gain medium: absorption, spontaneous emission, and stimulated emission. Through absorption, the gain material absorbs the pump energy to reach an excited state that will then spontaneously emit a photon with less energy. The spontaneously emitted photon will then interact with the gain medium, inducing other excited states to undergo stimulated emission.

2.2.2 Einstein Coefficients

Einstein developed a theoretical model for the absorption and emission of light for a material under optical excitation. It was Einstein who first theorized the process of stimulated emission which would then lead to the discovery of the laser [27]. The transition rates between the ground state and the excited state can be calculated using the Einstein coefficients (illustrated in Figure 2.12). The transition rate for absorption (stimulated absorption) is dependent on the energy density of the pumping photons (u_v) and the

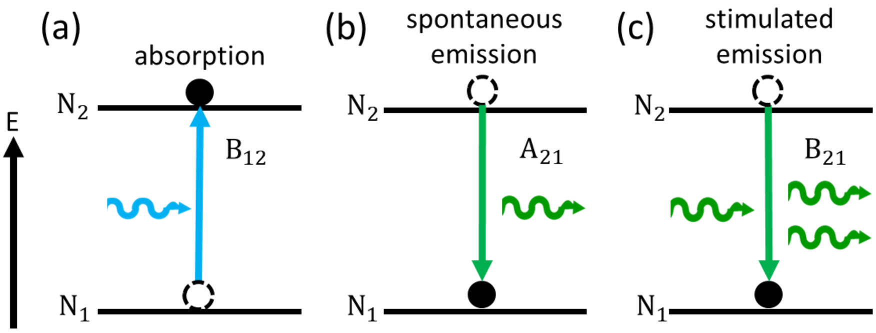

Figure 2.12: Optical transitions and their corresponding Einstein coefficients for (a) absorption, (b) spontaneous and (c) stimulated emission.

population of the ground state (N_1) where the Einstein absorption coefficient is the constant of proportionality (B_{12}):

$$\left(\frac{dN_1}{dt}\right)_{ab} = -B_{12}N_1u_v \tag{2.6}$$

The stimulated emission transition rate is the reverse of absorption and can therefore be calculated using a similar equation where B_{21} is the Einstein stimulated emission coefficient:

$$\left(\frac{dN_2}{dt}\right)_{st} = -B_{21}N_2u_v \tag{2.7}$$

The transition rate for spontaneous emission is a process that does not involve an incident photon and is therefore independent of the energy density of the pumping photons:

$$\left(\frac{dN_2}{dt}\right)_{sp} = -A_{21}N_2 \tag{2.8}$$

The probability for stimulated/spontaneous emission and absorption are proportional to the transition rates by dividing by the population of that state. Therefore, the probability for stimulated/spontaneous emission and absorption are related to the Einstein coefficients A and B.

2.2.3 Energy Level Population

Using Boltzmann's law for a gas in equilibrium in a black box where black-body radiation will induce absorption, spontaneous and stimulated emission, the populations for the excited state and ground state can be calculated:

$$N_1 = N_0 e^{-\frac{E_1}{k_b T}} \tag{2.9}$$

Where N_1 is the number of atoms with energy E_1at temperature T and N_0 is constant with k_b being Boltzmann's constant. This equation tells us that the population decreases for higher energy states when compared to lower energy states. Making N_1 the population of the ground state and N_2 the population of the excited state, the ratio between the two populations becomes:

$$\frac{N_2}{N_1} = \frac{e^{-\frac{E_2}{k_b T}}}{e^{-\frac{E_1}{k_b T}}} \tag{2.10}$$

Therefore, the population for the excited state can be written as:

$$N_2 = N_1 e^{-\frac{hv}{k_b T}} \tag{2.11}$$

Where the energy difference between the ground state and excited state can be substituted for the photon energy (hv) emitted for this transition. For this system to reach equilibrium the previously discussed rate equations must be balanced:

$$B_{12} N_1 u_v = A_{21} N_2 + B_{21} N_2 u_v \tag{2.12}$$

Substituting Planck's formula, $u_v = \frac{2hv^3}{c^2}\left(e^{\frac{hv}{k_b T}} - 1\right)^{-1}$ gives the energy spectrum for a black body:

$$B_{12}\frac{2hv^3}{c^2} = A_{21}(1 - e^{-\frac{hv}{k_bT}}) + B_{21}\frac{2hv^3}{c^2}e^{-\frac{hv}{k_bT}} \quad (2.13)$$

For this equation to be consistent for all temperatures then as $T \rightarrow \infty$ the Einstein coefficients for absorption and stimulated emission must be equal ($B_{21} = B_{12}$). Now when $T \rightarrow 0$ the Einstein coefficients show that a high absorption probability also relates to a high emission probability:

$$A_{21} = \frac{2hv^3}{c^2}B_{21} \quad (2.14)$$

2.2.4 Population Inversion

The acronym for LASER stands for 'Light Amplification by Stimulated Emission of Radiation' which implies that stimulated emission is integral to the lasing process. Stimulated emission is the process of an excited state emitting a photon identical to the photon stimulating the transition. The two photons will have the same wavelength, momentum, polarization and phase. For this process to continue, there must be as many excited states in the gain medium as possible. It is therefore the role of the external pump source to ensure that more states are excited than resting in the ground state. When the population of excited states is greater than that of the ground state it is known as a population inversion. For a population inversion to be created the stimulated emission rate needs to exceed the absorption rate:

$$B_{21}N_2u_v > B_{12}N_1u_v \quad (2.15)$$

Using this relation with equation (2.12), then only when $N_2 > N_1$ there is a population inversion that allows the system to act as an amplifier via stimulated emission.

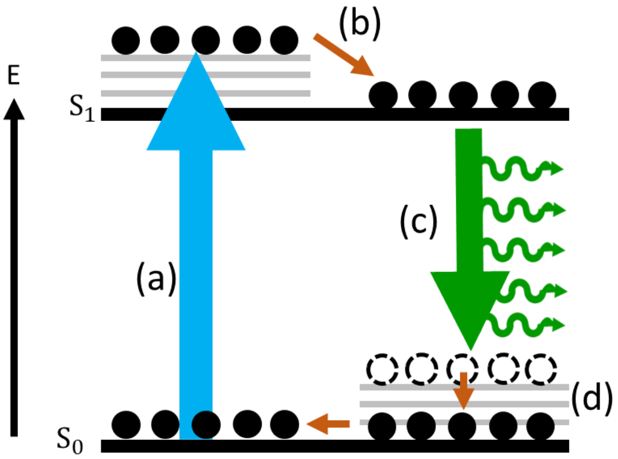

Figure 2.13: Population inversion of a 4-level system undergoing stimulated emission. (a) absorption due to excitation; (b) non-radiative relaxation to the lowest S_1 energy level; (c) stimulated emission (d) non-radiative vibronic relaxation to the lowest ground state.

Einstein stated that a photon has an equal probability of being duplicated via stimulated emission or absorbed by a ground state electron. Therefore, stimulated emission and absorption have equal probabilities. For stimulation to dominate there must be fewer electrons in the ground state and more electrons in the excited state (population inversion). The two-level system in Figure 2.14 cannot achieve a sustained population inversion as absorption and stimulated emission rates are closely related. Figure 2.13 shows a four-level system that can achieve population inversion as the IC from the lower lasing transition state to the ground state is faster than the optical transition. Therefore, more electrons will be in the excited state than the ground state. The four-level system is natural for organic semiconducting materials due to the sub-vibronic energy levels of their excited states [28].

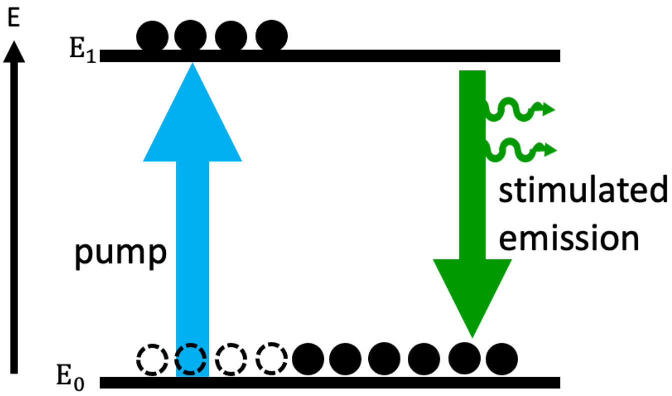

Figure 2.14: Two-level system diagram showing that a population inversion cannot be sustained there is not a substantial difference between the rate of absorption and stimulated emission

2.3 Feedback Structures

A requirement of lasing is that only the gain medium and the resonator should be responsible for the characteristics of the emitted light. The resonator's purpose is to give optical feedback at the stimulated emission wavelength in order to increase amplification. Feedback structures are commonly called resonators or optical cavities, but they all refer to the method by which light is confined into the gain medium. Due to the plastic behaviour of organics, feedback structures can be fabricated in a variety of different shapes (illustrated in Figure 2.15), such as microspheres [29, 30], microdisk [31], microrod [32] and photonic crystal [33]. However, due to their circular design, the emission is multidirectional, which is not beneficial for lasing [34]. The more commonly used resonator architectures are distributed Bragg gratings (DFB) [35-38] and microcavities that confine light using constructive interference [2, 39-44].

The gain of an organic laser is exponentially related to the distance the stimulated emitted light travels through the gain medium. Most optical cavities are approximately hundreds of nanometres in size for single mode confinement, and therefore the distance for a round-trip cycle is extremely limited. The gain is also dependent on the population inversion in the gain

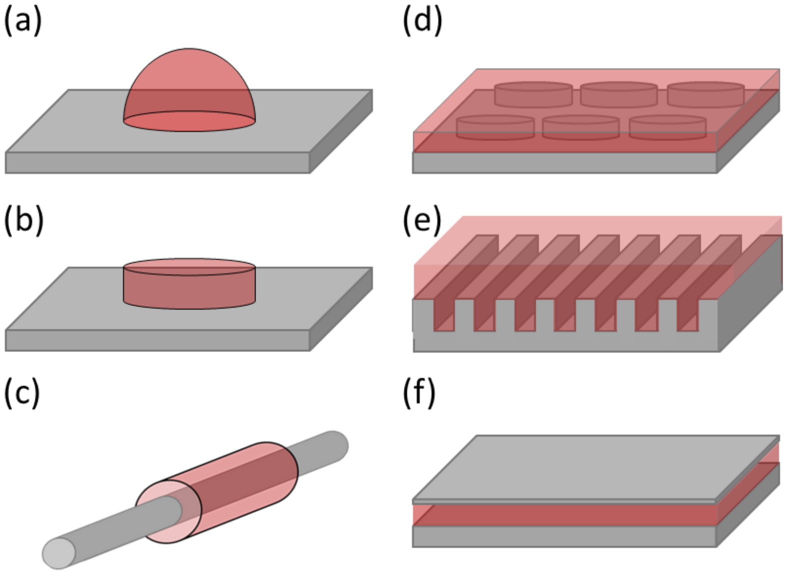

Figure 2.15: Feedback architecture for different resonators: (a) microsphere, (b) microdisk, (c) microrod, (d) 2D crystal, (e) DFB, (f) microcavity.

medium, which is controlled by the pumping intensity. Therefore, by increasing the efficiency of the resonator, less pumping power is needed and therefore lowers the lasing threshold. This is one of the reasons why feedback structures have been widely researched as a resonator that lowers the lasing threshold will make it easier to pump the gain medium.

2.3.1 Microcavities

A simple microcavity is made by sandwiching an organic gain material between two mirrors, where the distance between them is of wavelength scale. This is also known as a Fabry-Perot microcavity and was one of the first feedback structures realized for a diode configuration [45]. This architecture has already been demonstrated in optically pumped lasers and demonstrates a low lasing threshold by using the highly reflective DBR mirror to achieve a high Q factor [39]. Fabry-Perot microcavities are easily fabricated with organics due to their processability. An example design for a Fabry-Perot microcavity is illustrated in Figure 2.16.

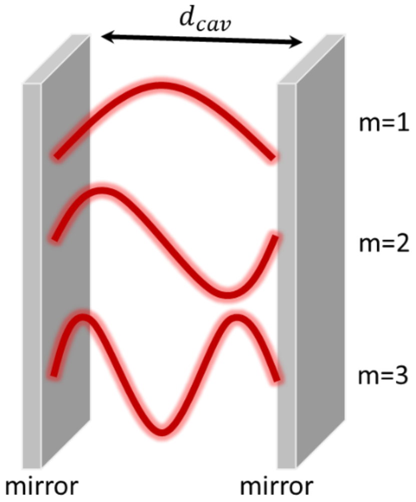

Figure 2.16: Simplified microcavity with a cavity length, d_{cav} supporting multiple modes.

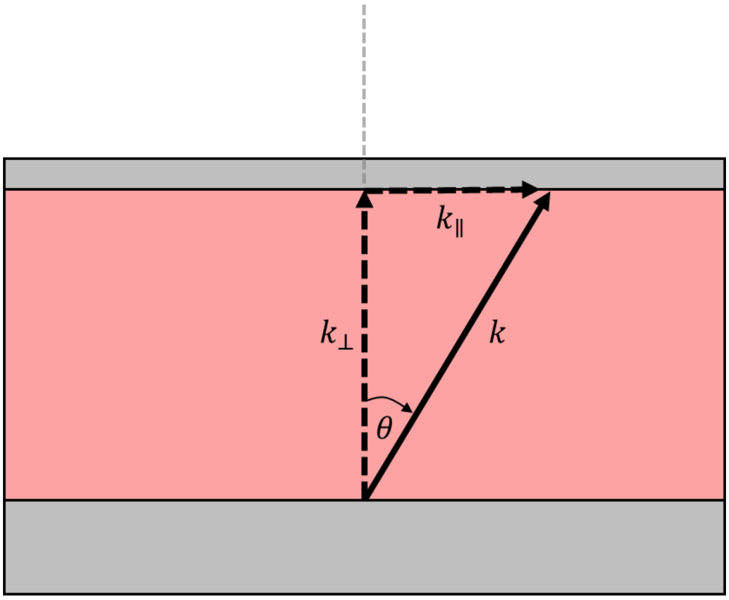

Figure 2.17: Microcavity with wavevector (k) with an angle (θ) from the cavity normal. This wavevector has components parallel ($k_{\|}$) and perpendicular ($k_{\perp}$) to the cavity normal.

A microcavity is created by placing two planar mirrors in close proximity to one another. This distance between the mirrors (d_{cav}) is typically comparable to the wavelength of the light so that a standing wave can be sustained. Figure 2.16 shows this in a very simplified case where only the light perpendicular to the mirrors is considered. For a more complete picture, light with a wavevector component parallel to the mirror needs to be considered. This can be shown in Figure 2.17 where light with a wavevector ($k = 2\pi/\lambda$) can be derived from parallel ($k_{\|}$) and perpendicular ($k_{\perp}$) wavevector components so that:

$$k = \sqrt{k_{\perp}^2 + k_{\|}^2} \tag{2.16}$$

If light propagates through the active layer of the microcavity with an incidence angle of (θ), the $k_{\|}$ and $k_{\perp}$ can be expressed as [46]:

$$k_{\perp} = k\cos(\theta) \tag{2.17}$$

$$k_{\|} = k\sin(\theta) \tag{2.18}$$

The wavelength perpendicular to the mirrors can be given as:

$$\lambda_{\perp} = \frac{2n_{cav}d_{cav}}{m} \tag{2.19}$$

Here n_{cav} is the refractive index of the active layer, and d_{cav} is the cavity length that is controlled by the active layer thickness. m denotes the cavity mode order and has a positive integer value (m >1). Substituting this into $k = 2\pi/\lambda$, the perpendicular wavevector can be derived:

$$k_{\perp} = \frac{\pi m}{n_{cav}d_{cav}} \tag{2.20}$$

Substituting the angular equation for $k_{\perp}$ gives:

$$k = \frac{\pi m}{n_{cav}d_{cav}\cos(\theta)} \tag{2.21}$$

and

$$\lambda = \frac{2n_{cav}d_{cav}\cos(\theta)}{m} \tag{2.22}$$

This is the angle-dependent wavelength of the cavity mode and can be expressed in terms of energy:

$$E = \frac{hc}{\lambda} = \frac{hcm}{2n_{cav}d_{cav}\cos(\theta)} = \frac{E_{\perp}}{\sqrt{1 - \sin^2(\theta)}} \tag{2.23}$$

Here $E_{\perp} = \frac{hcm}{2n_{cav}d_{cav}}$ is the cavity mode energy when observed at normal to the mirror plane. When observing from outside the microcavity with an observation angle of θ_{obs}, Snell's law ($n_{cav}\sin(\theta) = n_{air}\sin(\theta_{obs})$) can be applied to correct for outcoupling:

$$E = \frac{E_{\perp}}{\left(1 - \frac{\sin^2(\theta_{obs})}{n_{cav}^2}\right)^{\frac{1}{2}}} \tag{2.24}$$

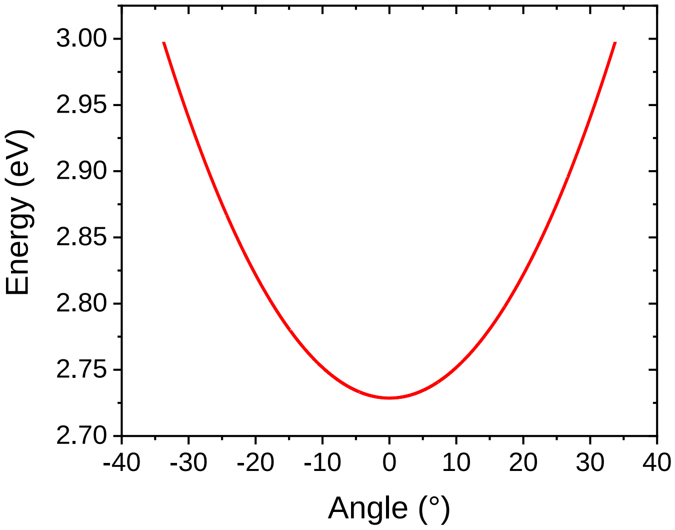

Figure 2.18: Calculated microcavity emission energy as a function of angle. This also considers the critical angle.

Using this equation, the emission energy as a function of angle can be calculated, and this is shown in Figure 2.18. This cavity dispersion is normal for most commonly used microcavities [47-50].

2.3.2 Spontaneous Emission Enhancement

Microcavities are designed to trap light between the two mirrors where the wavelengths of light that are confined within are determined by the cavity length. The lifetime of a photon inside the cavity gives information about the effectiveness of the confinement. This is typically estimated from the ratio of the linewidth of the cavity mode and its associated wavelength. This is commonly referred to as the cavity Q-factor [46]:

$$Q = \frac{\lambda}{\triangle \lambda} \tag{2.25}$$

The constructive interference to create a standing wave within the microcavity amplifies the population of identical wavelength photons inside the cavity. This amplification has the effect of modifying the optical density of states. This effect is strongly related to the microcavity Q-factor as this is a measure of the cavity photon lifetime. As the wavelengths supported by the cavity are related to the effective mode volume, this also contributes to the degree of enhancement. The optimum emission enhancement is given by the Purcell effect (F_p) [51]:

$$F_p = \frac{3}{4\pi^2}\frac{\lambda_c^3}{n^3}\frac{Q}{V_{eff}} \tag{2.26}$$

The Q-factor and the mode volume (V_{eff}) of the cavity can modify the density of optical states for the organic material to emit into, this has the effect of modifying the emission lifetime (τ) when compared to free space (τ_0):

$$\frac{\tau_0}{\tau} = F_p \frac{|\boldsymbol{d} \cdot E(\boldsymbol{r})|^2}{|E_{max}|^2} \frac{\delta\lambda_c^2}{\delta\lambda_c^2 + 4(\lambda_c - \lambda_e)^2} + f \tag{2.27}$$

This is more realistic as this considers the spectral and spatial mismatch. Here $\boldsymbol{d} \cdot E(\boldsymbol{r})$ is the field amplitude aligned to a dipole in the cavity, with a maximum amplitude of E_{max}. The cavity mode and emitter wavelengths are λ_c and λ_e respectively. f takes into account additional losses associated with leaky modes.

In the context of lasing, reducing the number of optical modes for the active layer to emit into causes an increase in the rate of spontaneous emission at the lasing wavelength. This effect is strong for a broad emitter such as an organic semiconductor. The fraction of spontaneous emission that is emitted into the lasing mode is given by the spontaneous emission coupling factor (β). The lasing threshold can be estimated using [46]:

$$E_{th} = \frac{h\omega_c^2}{4\pi Q\beta} \tag{2.28}$$

The low-lasing threshold for microcavities is also due to the narrow thickness of the lasing medium as less energy is needed to excite such a small volume into a population inversion.

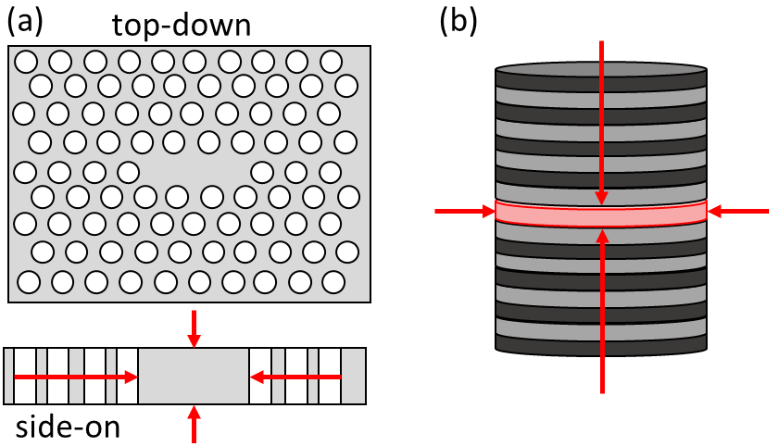

Figure 2.19: Methods to increase lateral confinement in a (a) 2D photonic crystal nanocavity (b) micropillar.

2.3.3 Increase Confinement

Planar microcavities offer confinement in one spatial direction, for additional confinement, the other two spatial directions need to contribute. This can be achieved using a 2D photonic crystal (shown in Figure 2.19a) where lateral confinement is provided by the photonic band gap [52]. Another approach is to use a micropillar structure (see Figure 2.19b), where internal reflection confines light in a whispering gallery mode [53]. This additional confinement in the lateral direction effectively reduces the volume of the microcavity. Decreasing the mode volume (V_{eff}) in combination with a high Q-factor (Q) gives a large enhancement to the Purcell effect and therefore increasing the rate of spontaneous emission compared to free space [54].

2.4 Distinguishing Lasing from Amplified Spontaneous Emission

As discussed before, lasing requires optical confinement from a resonator structure. However, optical gain can also be observed in thin films without such structures. For example, a gain medium can be pumped with a laser that is focused into a stripe. If the pump energy can achieve a population inversion, then the emission that waveguides down the stripe can undergo stimulated emission. The intensity of the emission leaving the end of the stripe $(I(\lambda))$ is given by:

$$I(\lambda) = \frac{A(\lambda)I_p}{g}(e^{gl} - 1) \tag{2.29}$$

Where I_p is the pump intensity, g is the net gain coefficient, l is the length of the stripe, and $A(\lambda)$ is a constant related to the spontaneous emission cross section. Keeping the stripe length constant, the non-linear output intensity is dependent the gain coefficient:

$$g = \Omega(N_2 - N_1) \tag{2.30}$$

Here Ω is the stimulated emission cross section and $(N_2 - N_1)$ is the population inversion. Therefore, the gain is dependent on the pump power of the excitation laser.

To claim lasing, one must provide evidence that the emission has specific characteristics that are unique to lasers. The fundamental process for both lasing and ASE is stimulated emission and the two can be confused with each other due to spectral narrowing. The following recommended list of characteristics must be demonstrated for emission to be regarded as lasing [55]:

1. Narrow emission linewidth due to stimulated emission dominating. For a laser, this process of amplifying identical photons is enhanced by the resonator. Therefore, the linewidth of this emission is typically < 1 nm, where ASE linewidths are substantially wider.
2. Output in the form of a beam that therefore has narrow divergence and good spectral behaviour. As the photons outcoupling from the laser are identical, their momentum is also identical and therefore so is the direction.

3. Clear thresholds for both output intensity and linewidth. Once a population inversion is achieved, the dominant method of emission changes from spontaneous to stimulated emission. This is shown in Figure 2.20 where the threshold for this cross-over is indicated by the sudden increase in output intensity. This increase should also correspond to a collapse in the emission linewidth. Plotting both the linewidth and the emission intensity together is the most used evidence to claim lasing.
4. Only the gain medium and the resonator should be responsible for the characteristics of the emitted light. Previous reports for lasing in organic semiconductors have been misinterpreted as lasing where narrow linewidths have been observed from leaky waveguided modes [56, 57].
5. Strong polarization and temporal coherence. This again is prevalent in ASE and lasing, however with the additional confinement from the resonator this effect is to a higher degree.

ASE can sometimes be confused with lasing – a single pass through a gain medium will give rise to stimulated emission and therefore amplification of the spontaneously emitted photons.

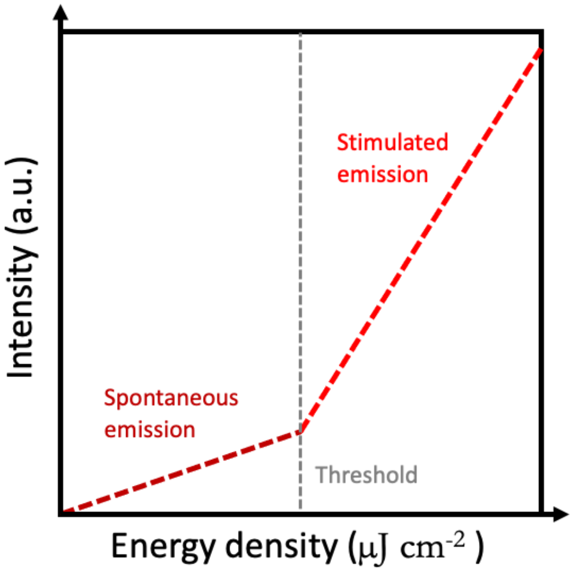

Figure 2.20: Example input-output characteristics for an organic semiconductor laser. The transition between the spontaneous to stimulated emission regime signifies the threshold energy density for lasing.

The results from this would be a narrower linewidth, polarization, and directionality. In this case, there is no resonator, this being the difference between a conventional laser. The emitted light will not have the enhanced characteristics provided by the resonator so the linewidth will be larger (Figure 2.21).

Spectral narrowing can often be misinterpreted as lasing as monochromaticity is one of the most obvious characteristics. Waveguides are very popular for confining light and emerging light can be in the shape of a beam, which can also be mistaken for lasing. However, it is also possible for light to leak out of the waveguide for a specific wavelength, and into the substrate. This "leaky wave" can propagate next to the waveguide and emerge with spectrally narrow emission. Materials surrounding the gain medium can also be accidentally excited and relaxed through the emission of a photon. Optical transitions from a metallic electrode can be very narrow and misinterpreted.

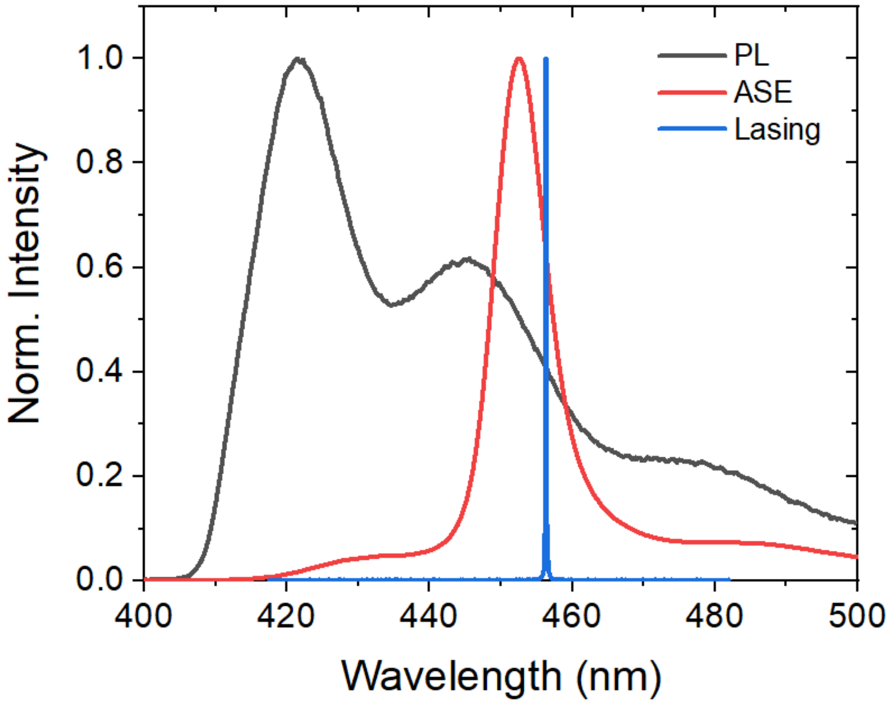

Figure 2.21: Comparison between the three different types of emission: photoluminescence (black), ASE (red) and lasing (blue) from a conjugated polymer.

2.5 References

[1] D. Moses, “High quantum efficiency luminescence from a conducting polymer in solution: A novel polymer laser dye,” Appl. Phys. Lett., vol. 60, no. 26, pp. 3215–3216, Jun. 1992, doi: 10.1063/1.106743.

[2] G. J. D. & R. H. F. N. Tessler, “Lasing from conjugated polymer microcavities,” Nature, vol. 382, no. August, pp. 695–697, 1996.

[3] S. Forget and S. Chénais, “Organic Solid-State Lasers”, vol. 175. in Springer Series in Optical Sciences, vol. 175. Berlin, Heidelberg: Springer Berlin Heidelberg, 2013. doi: 10.1007/978-3-642-36705-2.

[4] Y. Jiang et al., “Organic solid-state lasers: a materials view and future development,” Chem. Soc. Rev., vol. 49, no. 16, pp. 5885–5944, Aug. 2020, doi: 10.1039/D0CS00037J.

[5] N. A. Talik, Y. B. Kar, S. N. M. Tukijan, and C. L. Wong, “Review on recent Developments on Fabrication Techniques of Distributed Feedback (DFB) Based Organic Lasers,” J. Phys. Conf. Ser., vol. 914, no. 1, 2017, doi: 10.1088/1742-6596/914/1/012032.

[6] C. Adachi and A. S. D. Sandanayaka, “The Leap from Organic Light-Emitting Diodes to Organic Semiconductor Laser Diodes,” CCS Chem., vol. 2, no. 4, pp. 1203–1216, Aug. 2020, doi: 10.31635/CCSCHEM.020.202000327.

[7] K. Yoshida, J. Gong, A. L. Kanibolotsky, P. J. Skabara, G. A. Turnbull, and I. D. W. Samuel, “Electrically driven organic laser using integrated OLED pumping,” Nat. 2023 6217980, vol. 621, no. 7980, pp. 746–752, Sep. 2023, doi: 10.1038/s41586-023-06488-5.

[8] P. G. Polishchuk, T. I. Madzhidov, and A. Varnek, "Estimation of the size of drug-like chemical space based on GDB-17 data," J. Comput. Aided. Mol. Des., vol. 27, no. 8, pp. 675–679, Aug. 2013, doi: 10.1007/S10822-013-9672-4/FIGURES/2.

[9] P. W. (Peter W. Atkins, "Atkins' physical chemistry / Peter Atkins, Julio de Paula.," Physikalische Chemie. p. 972, 2010. Accessed: Nov. 16, 2023. [Online]. Available: https://global.oup.com/academic/product/atkins-physical-chemistry-9780198847816?cc=gb&lang=en&

[10] J. Roncali, "Molecular Engineering of the Band Gap of π-Conjugated Systems: Facing Technological Applications," Macromol. Rapid Commun., vol. 28, no. 17, pp. 1761–1775, Sep. 2007, doi: 10.1002/MARC.200700345.

[11] J. L. Brédas, R. Silbey, D. S. Boudreaux, and R. R. Chance, "Chain-Length Dependence of Electronic and Electrochemical Properties of Conjugated Systems: Polyacetylene, Polyphenylene, Polythiophene, and Polypyrrole," J. Am. Chem. Soc., vol. 105, no. 22, pp. 6555–6559, Oct. 1983, doi: 10.1021/JA00360A004.

[12] Y. Wang, "Low Threshold Organic Semiconductor Lasers," 2014, doi: 10.1007/978-3-319-01267-4.

[13] R. Scholz, "Organic Semiconductors," Encycl. Condens. Matter Phys., pp. 206–221, Jan. 2005, doi: 10.1016/B0-12-369401-9/00658-6.

[14] D. Sanvitto and S. Kéna-Cohen, "The road towards polaritonic devices," Nature Materials, vol. 15, no. 10. Nature Publishing Group, pp. 1061–1073, Jul. 18, 2016. doi: 10.1038/nmat4668.

[15] J. van der Horst, P. Bobbert, P. de Jong, M. Michels, G. Brocks, and P. Kelly, "Ab initio prediction of the electronic and optical excitations in polythiophene: Isolated chains

versus bulk polymer," Phys. Rev. B, vol. 61, no. 23, p. 15817, Jun. 2000, doi: 10.1103/PhysRevB.61.15817.

[16] J. L. Brédas, D. Beljonne, V. Coropceanu, and J. Cornil, "Charge-transfer and energy-transfer processes in π-conjugated oligomers and polymers: A molecular picture," Chem. Rev., vol. 104, no. 11, pp. 4971–5003, Nov. 2004, doi: 10.1021/CR040084K/ASSET/IMAGES/MEDIUM/CR040084KE00035.GIF.

[17] M. Kasha, "Characterization of electronic transitions in complex molecules," Discuss. Faraday Soc., vol. 9, no. 0, pp. 14–19, Jan. 1950, doi: 10.1039/DF9500900014.

[18] J. R. Lakowicz, "Principles of fluorescence spectroscopy," Princ. Fluoresc. Spectrosc., pp. 1–954, 2006, doi: 10.1007/978-0-387-46312-4/COVER.

[19] W. Holzer, A. Penzkofer, H. Tillmann, and H. H. Hörhold, "Spectroscopic and travelling-wave lasing characterisation of Gilch-type and Horner-type MEH-PPV," Synth. Met., vol. 140, no. 2–3, pp. 155–170, Feb. 2004, doi: 10.1016/S0379-6779(03)00356-4.

[20] M. Lehnhardt, T. Riedl, T. Weimann, and W. Kowalsky, "Impact of triplet absorption and triplet-singlet annihilation on the dynamics of optically pumped organic solid-state lasers," Phys. Rev. B - Condens. Matter Mater. Phys., vol. 81, no. 16, p. 165206, Apr. 2010, doi: 10.1103/PHYSREVB.81.165206/FIGURES/6/MEDIUM.

[21] J. Yu, R. Lammi, A. J. Gesquiere, and P. F. Barbara, "Singlet-triplet and triplet-triplet interactions in conjugated polymer single molecules," J. Phys. Chem. B, vol. 109, no. 20, pp. 10025–10034, May 2005, doi: 10.1021/JP0506742.

[22] G. N. Lewis and M. Kasha, "Phosphorescence and the Triplet State," J. Am. Chem. Soc., vol. 66, no. 12, pp. 2100–2116, Dec. 1944, doi: 10.1021/JA01240A030/ASSET/JA01240A030.FP.PNG_V03.

[23] N. C. Greenham et al., "Measurement of absolute photoluminescence quantum efficiencies in conjugated polymers," Chem. Phys. Lett., vol. 241, no. 1–2, pp. 89–96, Jul. 1995, doi: 10.1016/0009-2614(95)00584-Q.

[24] J. Franck, E. D.-T. of the F. Society, and undefined 1926, "Elementary processes of photochemical reactions," pubs.rsc.orgJ Fr. EG DymondTransactions Faraday Soc. 1926•pubs.rsc.org, Accessed: Nov. 15, 2023. [Online]. Available: https://pubs.rsc.org/en/content/articlepdf/1926/tf/tf9262100536

[25] E. U. Condon, "Nuclear Motions Associated with Electron Transitions in Diatomic Molecules," Phys. Rev., vol. 32, no. 6, p. 858, Dec. 1928, doi: 10.1103/PhysRev.32.858.

[26] E. U. Condon, "The Franck-Condon Principle and Related Topics," Am. J. Phys, vol. 15, pp. 365–374, 1947, doi: 10.1119/1.1990977.

[27] A. Landé, "Zur Quantentheorie der Strahlung," Zeitschrift für Phys., vol. 35, no. 5, pp. 317–322, 1926, doi: 10.1007/BF01380146.

[28] M. Anthony M. Fox, "Quantum optics : an introduction," p. 378, OUP Oxford, 2006.

[29] J. H. Burroughes D D C Bradley et al., "Solid-state droplet laser made from an organic blend with a conjugated polymer emitter," Adv. Mater., vol. 9, no. 12, pp. 968–971, Jan. 1997, doi: 10.1002/ADMA.19970091208.

[30] M. Kuwata-Gonokami, "Laser emission from dye-doped polystyrene microsphere," Conf. Proc. - Lasers Electro-Optics Soc. Annu. Meet., pp. 300–301, 1993, doi: 10.1109/LEOS.1993.379042.

[31] F. Sasaki et al., “Microdisk and microring lasers of thiophene-phenylene Co-oligomers embedded in Si/SiO2 substrates,” Adv. Mater., vol. 19, no. 21, pp. 3653–3655, Nov. 2007, doi: 10.1002/ADMA.200701008.

[32] S. Frolov, M. Shkunov, Z. Vardeny, and K. Yoshino, “Ring microlasers from conducting polymers,” Phys. Rev. B, vol. 56, no. 8, p. R4363, Aug. 1997, doi: 10.1103/PhysRevB.56.R4363.

[33] M. Meier et al., “Laser action from two-dimensional distributed feedback in photonic crystals,” Appl. Phys. Lett., vol. 74, no. 1, pp. 7–9, Jan. 1999, doi: 10.1063/1.123116.

[34] H. Dong, C. Zhang, and Y. S. Zhao, “Controlling the Output of Organic Micro/Nanolasers,” Adv. Opt. Mater., vol. 7, no. 17, p. 1900037, Sep. 2019, doi: 10.1002/adom.201900037.

[35] N. Moll et al., “Evidence for bandedge lasing in a two-dimensional photonic bandgap polymer laser,” Appl. Phys. Lett., vol. 80, no. 5, pp. 734–736, Feb. 2002, doi: 10.1063/1.1446213.

[36] E. B. Namdas et al., “Low thresholds in polymer lasers on conductive substrates by distributed feedback nanoimprinting: Progress toward electrically pumped plastic lasers,” Adv. Mater., vol. 21, no. 7, pp. 799–802, 2009, doi: 10.1002/adma.200802436.

[37] C. Karnutsch et al., “Improved organic semiconductor lasers based on a mixed-order distributed feedback resonator design,” Appl. Phys. Lett., vol. 90, no. 13, pp. 1–4, 2007, doi: 10.1063/1.2717518.

[38] Y. Yang, G. A. Turnbull, and I. D. W. Samuel, “Hybrid optoelectronics: A polymer laser pumped by a nitride light-emitting diode,” Appl. Phys. Lett., vol. 92, no. 16, p. 163306, Apr. 2008, doi: 10.1063/1.2912433/334780.

[39] Y. Hu, F. Bencheikh, S. Chénais, S. Forget, X. Liu, and C. Adachi, “High performance planar microcavity organic semiconductor lasers based on thermally evaporated top distributed Bragg reflector,” Appl. Phys. Lett., vol. 117, no. 15, p. 153301, Oct. 2020, doi: 10.1063/5.0016052.

[40] O. Mhibik et al., “An ultra-narrow linewidth solution-processed organic laser,” Light Sci. Appl. 2016 52, vol. 5, no. 2, pp. e16026–e16026, Feb. 2016, doi: 10.1038/lsa.2016.26.

[41] M. T. Hill and M. C. Gather, “Advances in small lasers,” Nat. Photonics 2014 812, vol. 8, no. 12, pp. 908–918, Nov. 2014, doi: 10.1038/nphoton.2014.239.

[42] J. Lin, Y. Hu, Y. Lv, X. Guo, and X. Liu, “Light gain amplification in microcavity organic semiconductor laser diodes under electrical pumping,” Sci. Bull., vol. 62, no. 24, pp. 1637–1638, 2017, doi: 10.1016/j.scib.2017.12.010.

[43] M. C. Gather and S. H. Yun, “Bio-optimized energy transfer in densely packed fluorescent protein enables near-maximal luminescence and solid-state lasers,” Nat. Commun. 2014 51, vol. 5, no. 1, pp. 1–8, Dec. 2014, doi: 10.1038/ncomms6722.

[44] M. Koschorreck, R. Gehlhaar, V. G. Lyssenko, M. Swoboda, M. Hoffmann, and K. Leo, “Dynamics of a high- Q vertical-cavity organic laser,” Appl. Phys. Lett., vol. 87, no. 18, pp. 1–3, Oct. 2005, doi: 10.1063/1.2125128/330123.

[45] X. Liu, H. Li, C. Song, Y. Liao, and M. Tian, “Microcavity organic laser device under electrical pumping,” Opt. Lett., vol. 34, no. 4, p. 503, 2009, doi: 10.1364/ol.34.000503.

[46] F. P. L. Alexey V. Kavokin, Jeremy J. Baumberg, Guillaume Malpuech, Microcavities, Second Edi. Oxford Science Publications, 2017.

[47] P. Claronino, R. Jayaprakash, T. Jessewitsch, R. C. Kilbride, T. Thornber, A. Muravitskaya, R. D. J. Oliver, U. Scherf, J. S. G. Bouillard, A. M. Adawi, D. G. Lidsey, “Organic copolymer lasing from single defect microcavity fabricated using laser patterning,” J. Mater. Chem. C, vol. 11, no. 24, pp. 8204–8213, Jun. 2023, doi: 10.1039/D2TC05360H.

[48] D. G. Lidzey and D. M. Coles, “Strong coupling in organic and hybrid-semiconductor microcavity structures,” Org. Hybrid Photonic Cryst., pp. 243–273, Jan. 2015, doi: 10.1007/978-3-319-16580-6_11/COVER.

[49] K. E. McGhee, R. Jayaprakash, K. Georgiou, S. L. Burg, and D. G. Lidzey, “Polariton condensation in a microcavity using a highly-stable molecular dye,” J. Mater. Chem. C, vol. 10, no. 11, pp. 4187–4195, 2022, doi: 10.1039/D1TC05554B.

[50] A. Genco et al., “k-Space Hyperspectral Imaging by a Birefringent Common-Path Interferometer,” ACS Photonics, vol. 9, no. 11, pp. 3563–3572, Nov. 2022, doi: 10.1021/ACSPHOTONICS.2C00959/ASSET/IMAGES/LARGE/PH2C00959_0006.JPEG.

[51] E. M. Purcell, “Spontaneous Emission Probabilities at Radio Frequencies”, Phys. Rev., vol. 69, no. 11–12, pp. 674–674, Jun. 1946.

[52] A. M. Adawi, M. M. Murshidy, P. W. Fry, and D. G. Lidzey, “An optical nanocavity incorporating a fluorescent organic dye having a high quality factor,” ACS Nano, vol. 4, no. 6, pp. 3039–3044, Jun. 2010, doi: 10.1021/NN1001479/ASSET/IMAGES/MEDIUM/NN-2010-001479_0005.GIF.

[53] F. L. Al‐Jashaam, R. Jayaprakash, D. M. Coles, A. J. Musser, K. Georgiou, and D. G. Lidzey, “Optical‐Mode Structure of Micropillar Microcavities Containing a

Fluorescent Conjugated Polymer," Adv. Quantum Technol., vol. 3, no. 2, p. 1900067, Feb. 2020, doi: 10.1002/qute.201900067.

[54] J. B. Khurgin and M. A. Noginov, "How Do the Purcell Factor, the Q - Factor, and the Beta Factor Affect the Laser Threshold?," Laser Photon. Rev., vol. 15, no. 3, p. 2000250, Mar. 2021, doi: 10.1002/lpor.202000250.

[55] I. D. W. Samuel, E. B. Namdas, and G. A. Turnbull, "How to recognize lasing," Nat. Photonics, vol. 3, no. 10, pp. 546–549, 2009, doi: 10.1038/nphoton.2009.173.

[56] D. Yokoyama, M. Moriwake, and C. Adachi, "Spectrally narrow emissions at cutoff wavelength from edges of optically and electrically pumped anisotropic organic films," J. Appl. Phys., vol. 103, no. 12, p. 123104, Jun. 2008, doi: 10.1063/1.2942401/287579.

[57] Y. Tian et al., "Spectrally narrowed edge emission from organic light-emitting diodes," Appl. Phys. Lett., vol. 91, no. 14, Oct. 2007, doi: 10.1063/1.2778358/921147.

Chapter 3: Experimental Methods

This chapter covers the experimental methods used in the preparation, fabrication, and measurement of samples in this thesis. For the most important methodologies, additional theory will be added to provide a detailed description of the underlying physics. Additional information for specific material fabrication parameters (thermal evaporation deposition rates etc.) is given in the following chapters, as each experimental chapter will include a methods section.

3.1 Sample Fabrication

3.1.1 Thin Film Fabrication

3.1.1.1 Substrate Cleaning Procedure

In order to fabricate high quality films, ultra flat substrates are typically used. Here ultra-flat quartz coated (20 nm) substrates were purchased from Ossila with dimensions 15 x 20 mm. Before any processing, substrates were cleaned in the following order: sequential ultrasonic baths of Hellmanex III, deionised water and isopropanol for 10 minutes each. After the isopropanol bath, substrates were dried using a nitrogen gun and then transferred into a glass petri dish where they were exposed to a high-power UV light source that creates Ozone for 15 minutes, removing any organic contaminants.

3.1.1.2 Polymer Spin Coating

The solution processability of organic materials is an attractive property as this offers a variety of fabrication processes such as spray coating. As shown in Figure 3.1, all polymer films were deposited by first dissolving the polymer in a solvent solution and then casting this onto a rotating substrate in ambient conditions. Substrates were vacuum sealed onto the chuck of the spin coater and rotated at a fixed revolutions per minute (rpm). This was usually

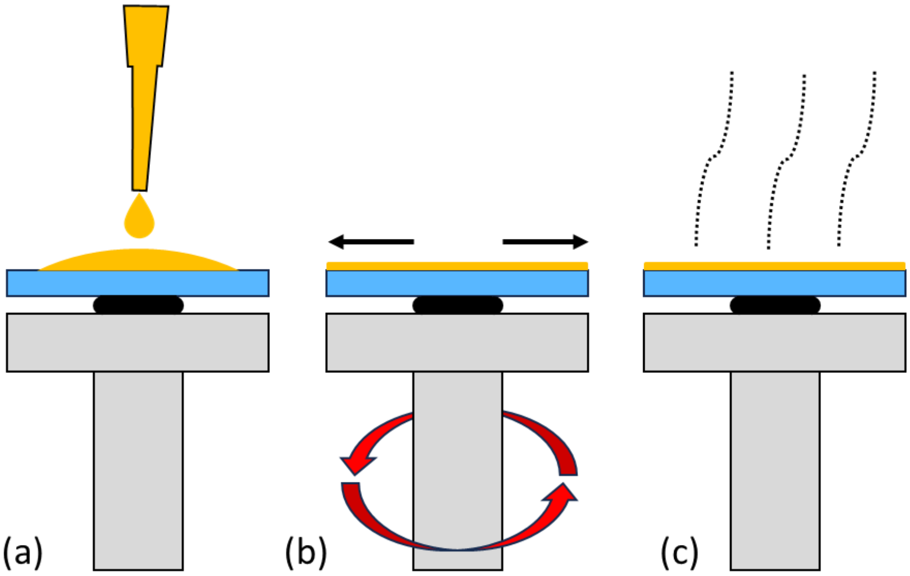

Figure 3.1: Spin coating procedure used to spin coat polymer thin films (a) the deposition with a pipette (b) spinning off the solution across the surface of the substrate (c) evaporating the residual solvent.

set to be over 2000 rpm in order to get sufficient film coverage. The solution was then deposited from a pipette (50-100 μL), onto the rotating sample to create a thin film of the polymer. Once all the solvent has evaporated from the film, a uniform polymer film remains. In order to control the thickness (d) of the film, two variables were controlled, the spin-speed and the solution concentration. The film thickness (d) is related to the spin speed (ω) using $d \propto 1/\sqrt{\omega}$ [1]. If the desired thickness could not be achieved within the available range of spin speeds, the concentration of the solution was changed.

3.1.1.3 Small molecule deposition

An Angstrom Engineering thermal evaporation system (shown in Figure 3.2) was used to deposit all small molecules in this thesis. This deposition method provides accurate control over film thickness and can be used to deposit films with high surface uniformity. Organic small molecules in powder form were loaded into a ceramic crucible that was slowly heated under a vacuum (2.6×10^{-7} mBar) using a Radak source. A wire coiled around the crucible heated the material to the required evaporation temperature. The deposition rate was monitored using a quartz-crystal microbalance (QCM). The deposition rate measured from the QCM gave feedback to the power supplied to the Radak source to maintain a constant

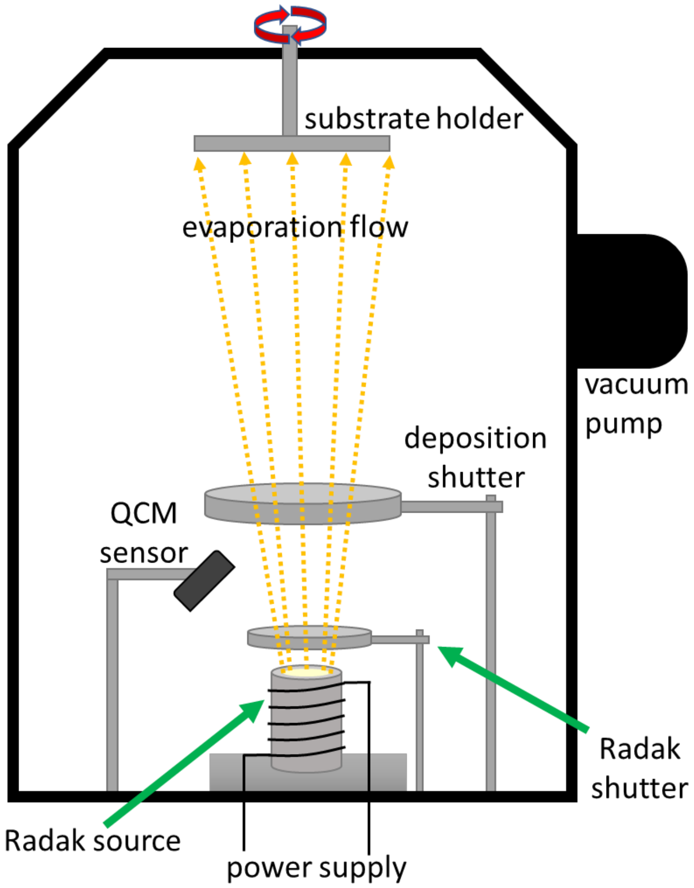

Figure 3.2: Simplified schematic of an Angstrom engineering thermal evaporator used to deposit small molecules. A resistive source was used to heat a ceramic crucible containing the material. The power delivered to heating the source was controlled using a quartz crystal microbalance (QCM) to maintain a constant deposition rate.

deposition rate. For all small molecules, a tooling factor was calculated and used to calibrate film thickness. This was done by comparing measured thickness (d_{meas}) determined using the Dektak stylus profilometer with desired thickness (d_{QCM}). Using these two thicknesses with the equation below, the new tooling factor was calculated.

$$T_{new} = T_{old} \times \frac{d_{meas}}{d_{QCM}} \tag{3.1}$$

3.1.1.4 DBR fabrication

Highly reflective mirrors were used to make microcavities. These were made by depositing alternating layers of, TiO_2 and SiO_2 due to the large difference in their refractive index. The TiO_2 and SiO_2 were deposited using an Angstrom Engineering electron-beam evaporator (shown in Figure 3.3) at a rate of 2 Ås^{-1} with a vacuum chamber base pressure of 4 x 10^{-6}

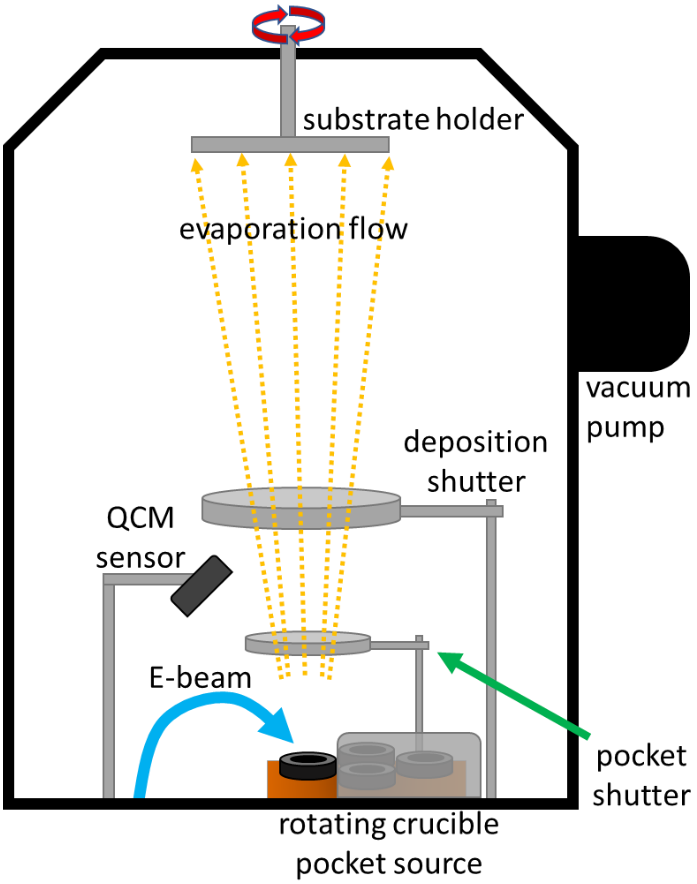

Figure 3.3: Schematic of Angstrom engineering electron-beam evaporation system used to grow DBRs.

mBar. This e-beam system has four rotating pockets allowing the deposition material to be changed while still under vacuum.

As the reflectivity of a DBR mirror is sensitive to the thickness of each of the alternating dielectric layers, the tooling factor for each material was updated before each fabrication attempt. First, the crucible was filled to 70% capacity and conditioned by slowly melting the TiO_2. The chamber was vented and the TiO_2 crucible was filled to 90% and then conditioned again. A silicon wafer was then loaded into the chamber and 100 nm of TiO_2 was deposited. The real thickness and optical constants of the film were measured using a J.A Woolam M-2000 ellipsometer. This real thickness was then used to update the TiO_2 tooling factor. This was then repeated for SiO_2.

After TiO_2 and SiO_2 tooling factors were calculated, the optical constants were used to calculate the thickness of the alternating layers (discussed further in Chapter 5). Once the layer thicknesses were finalised, the substrate were cleaned and loaded into the e-beam chamber for deposition. As the SiO_2 layer is typically thicker than the TiO_2 layer, the SiO_2 source often needed to be refilled. After four pairs had been deposited, the process was halted and the chamber is vented to refill the SiO_2 crucible to 90% capacity. The chamber was then pumped down and the rest of the DBR deposited.

3.1.1.5 Polystyrene laser patterning

In Chapter 6, microcavities were grown above defect structures to increase their lateral confinement. Defects were melted into a polystyrene (PS) film using a, frequency-doubled Ti:sapphire (Coherent MIRA) laser that was focused onto the polystyrene film. The wavelength of the Ti:sapphire laser was selected to be 890 nm that was then frequency doubled to 445 nm. This had a pulse width of 150 fs and a 76 MHz repetition rate. This delivered an average power of 23 mW, with the laser focused using a 50x Mitutoyo Plan Apo SL infinity corrected objective (setup shown in Figure 3.4). A single defect was created by exposing the PS film for 2.3 s. This caused localised melting and an out-flow of the semi-liquid polystyrene, resulting in the creation of a Gaussian-shaped defect 'dip' having a diameter of 2.5 μm and a maximum depth of 40 nm. A similar process is described in more detail in ref [2]. The sample holder was mounted vertically to a motorized linear stage (Newport MFA-CC) in an XY configuration. Both stages were driven by a Newport ESP301 2-axis controller.

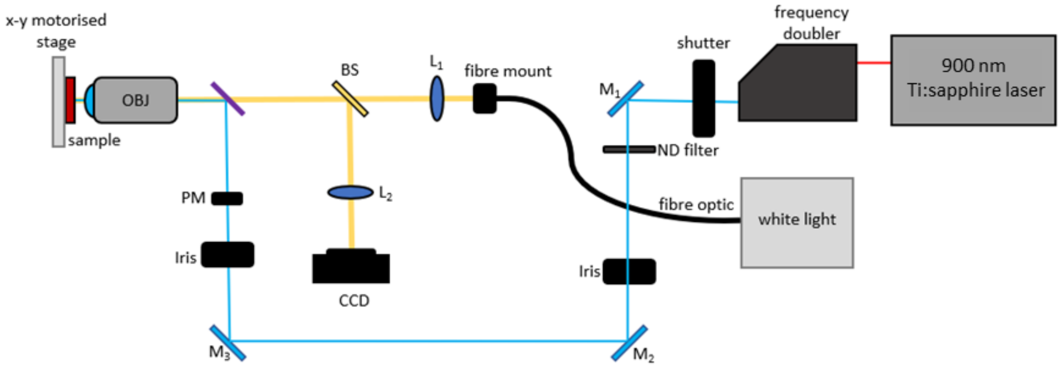

Figure 3.4: Laser patterning setup used for writing defect structures into PS films. Power meter (PM), beam splitter (BS), lens (L_x), mirror (M_x).

3.2 Surface Characterisation

3.2.1 Dektak Thin Film Thickness Measurements

A Bruker Dektak surface profilometer was used to measure film thickness. Figure 3.5 shows an example of a film thickness measurement. The surface of the thin films was scratched through to the quartz substrate and loaded onto the stage. The Dektak stylus then scanned over the scratch with a constant applied force. The variations in the restoring force of the stylus gave an estimate of the film thickness. For each sample, three scratches were measured, with multiple samples used to calculate the standard deviation. This estimation of the film thickness was used to calibrate deposition techniques in order to achieve the desired thicknesses.

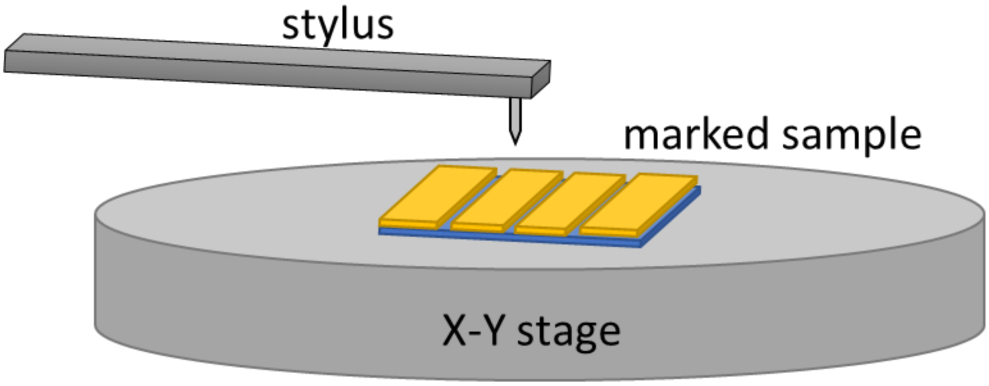

Figure 3.5: Example of a Dektak film thickness measurement. Here the sample is marked at the top, middle and bottom with a razor.

3.2.2 Atomic Force Microscopy

Atomic force microscopy (AFM) is a nanoscale surface measurement technique that can make non-destructive topography maps of a surface. All AFM measurements were performed in tapping mode. Figure 3.6 shows a typical schematic of an AFM setup. An oscillating cantilever taps the surface of the film with a laser focused onto the back of the cantilever and then reflected onto a 4-quadrant photodiode detector. The laser amplitude recorded by the detector changes as the oscillating tip moves across the surface. A feedback loop adjusts the vertical position of the scanner to maintain a constant tip oscillation. An AFM image is made by recording the vertical deflection at each (x, y) point.

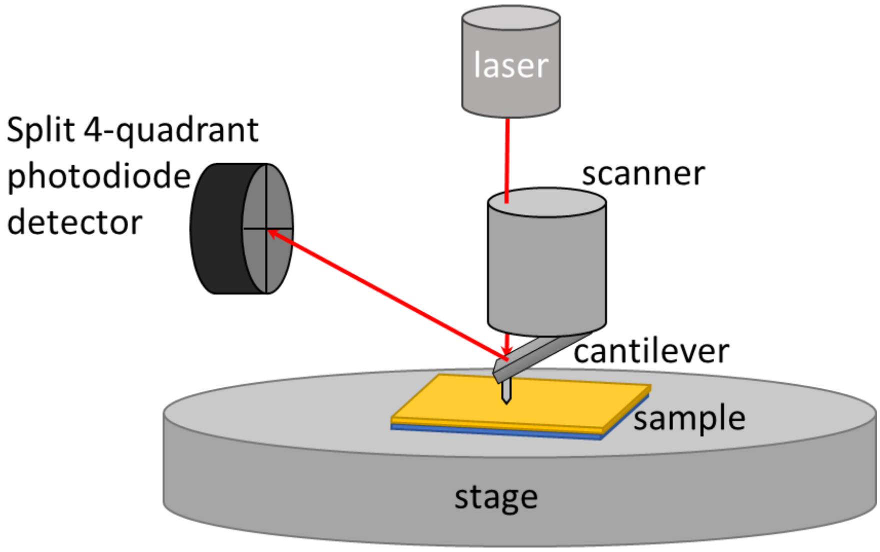

Figure 3.6: Schematic of an atomic force microscope used in tapping mode.

An atomic force microscope in tapping mode with a Nanoscope 3A feedback controller to control a 3100 Dimension scanning probe microscope (Veeco) was used to characterise the surface of films. This was equipped with Scot 350 (NuNano) probes with a spring constant of 42 N/m and a frequency of 350 kHz. Gwyddion software was then used to process the AFM images.

3.2.3 Grazing Incidence X-ray Scattering

A simplified experimental setup used for grazing incidence x-ray wide angle scattering is shown in Figure 3.7. Here X-rays are incident onto a film at a grazing angle of θ_i. Scattering is defined by an in-plane (ϕ) and an out-of-plane angle (θ_f). A 2D detector positioned at a distance l from the sample records these scattered X-rays. The scattering in vector space can be separated into three components Q = (Q_x, Q_y, Q_z).

$$Q_x = \frac{2\pi}{\lambda}\left(\cos(\phi)\cos(\theta_f) - \cos(\theta_i)\right) \tag{3.2}$$

$$Q_y = \frac{2\pi}{\lambda}\left(\sin(\phi)\cos(\theta_f)\right) \tag{3.3}$$

$$Q_z = \frac{2\pi}{\lambda}\left(\sin(\theta_i) + \sin(\theta_f)\right) \tag{3.4}$$

Grazing incidence wide-angle X-ray scattering (GIWAXS) was used to characterise the molecular packing of thin films. The system used was a a Xeuss 2.0 (Xenocs) system that operated with a liquid gallium MetalJet source (Excillum) that produced 9.24keV (λ=1.34Å) X-rays. This X-ray beam was directed at the surface of films prepared on quartz-coated substrates at a grazing angle of 0.15°. A Pilatus3R 1M 2D X-ray detector (Dectris) positioned ~ 300mm from the sample centre measured the X-rays that were scattered. The sample-to-detector distance was calibrated using a silver behenate standard measured in transmission geometry. In order to reduce the background air scatter, the sample chamber was held under vacuum for each measurement. The GIWAXS data was then corrected, reshaped and reduced using the GIXSGUI Matlab toolbox.43 and 1D intensity profiles were generated by azimuthally integrating the 2D patterns as a function of Q=4πsinθ/λ where θ is the angle between the incident and scattered X-ray of wavelength λ. Integrations were performed across the full azimuthal angle (χ) range normal to the incident beam on the detector (0° < χ < 90°). Intensity profiles were normalised to a flat region of background intensity.

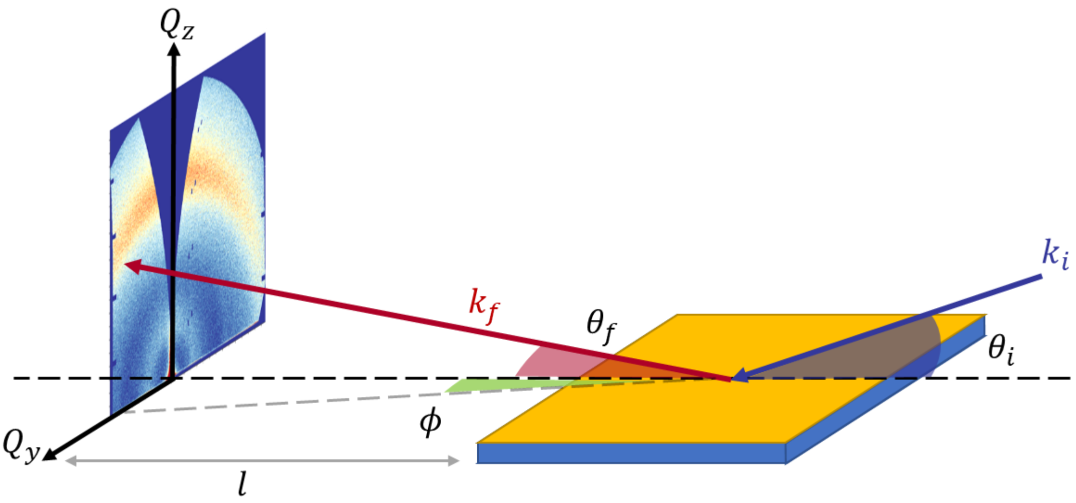

Figure 3.7: Setup for GIWAXS measurements, k_i represents the incident X-ray beam wavevector directed at the sample with an angle θ_i, k_f represents the wavevector of the scattered-rays with component angles ϕ and θ_f.

3.3 Optical Characterisation

3.3.1 Absorption and Photoluminescence Characterisation

Absorption and photoluminescence of organic thin films were characterised using a Horiba Fluoromax-4 fluorometer. The Fluoromax was equipped with a vertically mounted, CW, 150 W Ozone-free xenon arc lamp, where the excitation wavelength was selected using a 1200 mm blazed grating. A J1933 Solid Sample Holder was used to hold samples at normal incidence to the excitation port. Absorption and emission spectra was collected using an F-3031 Transmission Accessory.

3.3.2 k-space Imaging/Real Space

A k-space imaging setup was used to measure the PL emission from the cavities. This setup is detailed in Figure 3.8 where the sample was excited using a 355 nm Nd:YAG (100Hz, 350 ps) laser focused using a lens with a 150 mm focal length. The area of the spot size was measured with a Thorlabs beam profiler at the focal point. The beam profiler measured the semi-major and minor axis of the elliptical spot, and with these two lengths, the area of the laser spot was calculated. A UV filter was placed after the sample to prevent any damage to the objective. Emission from the sample was collected using a 20 × objective in a transmission configuration. The emission was then focused onto the back focal plane of the objective. This is also known as the Fourier plane and the position on this plane correspond to the angle at which the light was emitted. Therefore, this technique provides a detailed image of light emitted as a function of angle. This light was then collimated with a 250 mm focal length lens and focused with a 125 mm focal length lens onto the spectrometer CCD. With this, a dispersion of the emission can be captured as a function of angle and wavelength. The linewidth of the emission can therefore be measured, where the accuracy is dependent on the resolution of the spectrometer. By varying the pump power of the laser excitation, the input-output characteristics of cavities can be used to study the lasing threshold. The power of the laser was adjusted with a neutral-density wheel. This method was used in Chapters 5 and 6.

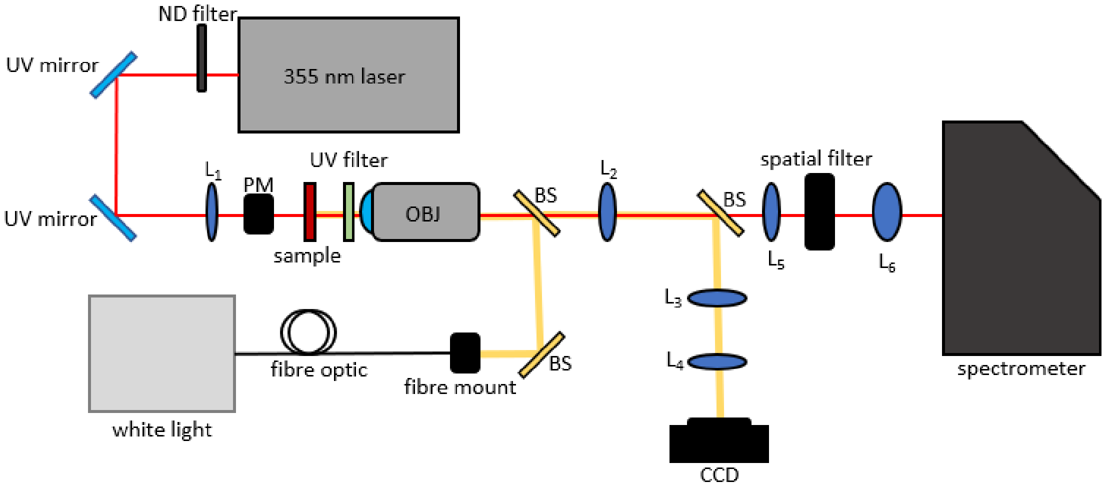

Figure 3.8: Shows k-space setup used for microcavity Fourier imaging PL dispersion allowing the spatial collapse of laser emission to be captured. The yellow path maps the white light imaging optics used to align and inspect the sample area before measurements. The white light source was a DH-2000-BAL Ocean Optics deuterium-halogen lamp coupled to a fibre optic cable. Light from the fibre was reflected through a series of beam splitters (BS) and focused onto the sample through an Edmund Optics 20 × HR infinity corrected objective (OBJ, N.A. = 0.6). The reflected light is then collected by the objective and focused through L2, L3 and L4, onto a ThorLabs CCD camera. To measure PL, the sample was excited by a Teem Photonics pulsed Q-switched 355 nm Nd:YAG laser (PNV-M02510-1 × 0) that was focused onto the sample with L1. Emission from the sample passes through a UV filter and collected by OBJ, L2 collimates the beam and L6 focuses it on the spectrometer CCD.

3.3.3 Photoluminescence Quantum Yield

The photoluminescence quantum yield (PLQY) is the ratio of the number of emitted photons to the number of absorbed photons by a material [3]. This can be measured using an integrating sphere, where the PL of the sample is randomly emitted in all directions and a fraction of the light is collected orthogonal to the sample surface. The absorption and the emission of a reference and the sample were used with a correction factor (C.F) in the following equation to calculate the PLQY:

$$QY(\%) = C.F\frac{(Emission_{sample} - Emisison_{reference})}{(Absorption_{sample} - Absorption_{reference})} \times 100 \tag{3.5}$$

The PLQY was measured using an integrating sphere attached to a Fluoromax-4 with the collection made using a photomultiplier. To prevent the saturation of the detector, a 0.5 % neutral density filter was placed just before it. Quartz cuvettes were used to contain the sample solvent solution with the reference being only the solvent.

3.3.4 Time-resolved Photoluminescence

For fluorescence lifetime measurements a Time Correlated Single Photon Counting (TCSPC) Becker and Hickl HPM-100 detector, coupled to a horiba microHR spectrometer was used. For this measurement, a sample was excited with a pulse of light having a duration shorter than the radiative decay lifetime (405 nm, 40 ps pules duration and 20 MHz reputation rate). The excitation pulse triggered an electronic signal that passed through a constant function discriminator (CFD) that measured the arrival time of the pulse. This same signal was then sent through a time-to-amplitude converter (TAC) that responds to the signal by generating a voltage that increased linearly as a function of time. Once the excitation pulse induces a photon to be emitted from the sample, the emitted photon is detected through a second channel. This channel sent a signal to the CFD that measures the arrival time. This triggers the TAC to stop increasing the voltage and the voltage difference was used to accurately calculate the time delay between excitation and emission. For this, the voltage is amplified

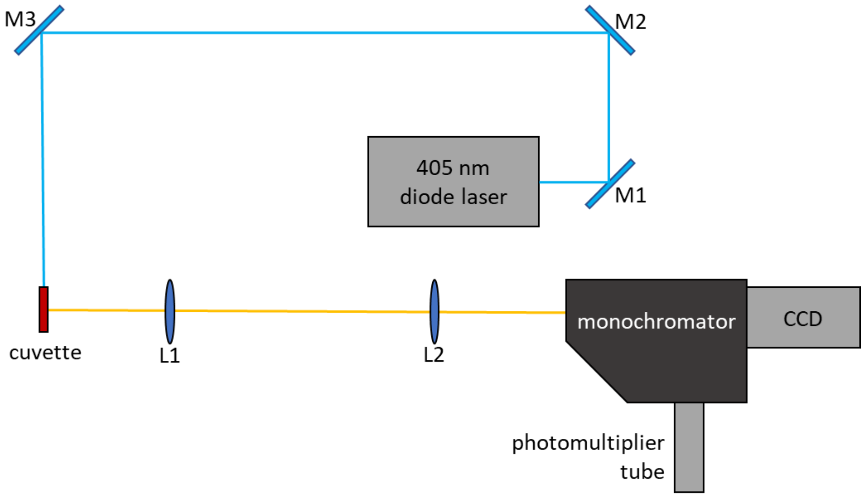

Figure 3.9: Fluorescence lifetime measurement experimental setup. The blue beam marks the excitation path and the yellow beam marks the collection path from the sample. Mirrors M1, M2 and M3 directs excitation laser to cuvette. Lenses L1 and L2 focus the emission from the sample into the monochromator.

by a programmable gain amplifier (PGA) and then converted from analogue to digital using an analogue-to-digital converter (ADC) to give a numerical value of the time delay. This capture happens for each excitation pulse and the time delay of each emitted photon is plotted in a histogram as a function of time and photon count.

Figure 3.9 shows the experimental setup for time-resolved photoluminescence measurements. A Thorlabs Inc. (CV10Q700F) cuvette was used to contain solutions of organic materials dissolved in solvent. Excitation from a 405 nm diode laser (LASOS LGO 1100-04) with a repetition rate of 20 MHz was guided to the cuvette through a series of mirrors. The photoluminescence was collimated and focused into a monochromator (Horiba - MicroHR). This signal could be imaged through the CCD (Princeton instruments ProEM HS:512BX3) or photomultiplier (Becker and Hickl HPM-100-40) for time-resolved measurements.

3.3.5 Amplified Spontaneous Emission

Amplified spontaneous emission (ASE) was measured in thin films using an ASE setup (shown in Figure 3.10). A Teem Photonics pulsed Q-switched 355 nm Nd:YAG (100Hz, 350 ps) laser was expanded using an aspherical UV lens with a focal length of 100 mm. This

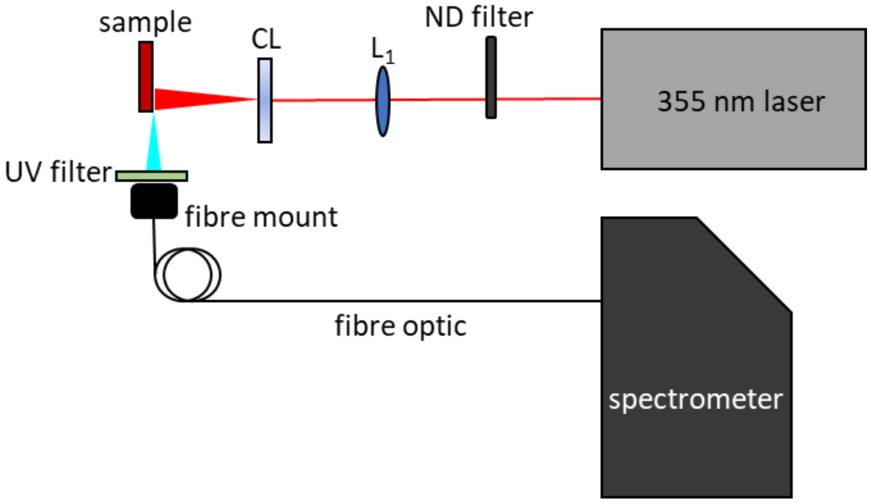

Figure 3.10: Experimental setup for ASE measurements. A cylindrical lens focuses the excitation laser into a stripe onto the sample. A fibre optic cable connected to a spectrometer collects the emission from the edge of the sample.

expanded beam was focused into a stripe using a cylindrical lens (25 mm focal length). The sample of interest was then aligned to the focal point of the laser stripe, so that the stripe overlapped the sample edge. The length of the laser stripe is dependent on the waist of the beam before entering the cylindrical lens. Therefore, the shape of the stripe could be controlled by adjusting the distance between the aspherical lens and cylindrical lens. Emission from the region under the laser stripe was waveguided within the thin film and emitted from the edge of the sample. This emission was then collected using a fibre optic cable connected to an Andor Shamrock SR-303i-A CCD with a 300 mm^{-1} grating and entrance slit set to 50 μm. Power dependent measurements for ASE thresholds were performed by inserting a neutral density wheel in front of the laser. The pump fluence was then measured with a ThorLabs Inc. power meter in series with the neutral density wheel.

3.3.6 Low-temperature Photoluminescence

Low-temperature photoluminescence (PL) was recorded by loading samples into an Oxford Instruments Optistat Dry BLV cryostat. After reducing the temperature to the desired level, samples were then excited with a 405 nm diode laser. The emission was collected at normal incidence with a free space fibre optic cable connected to an Ocean Optics Flame spectrometer.

3.4 References

[1] D. B. Hall, P. Underhill, and J. M. Torkelson, "Spin coating of thin and ultrathin polymer films," Polym. Eng. Sci., vol. 38, no. 12, pp. 2039–2045, Dec. 1998, doi: 10.1002/PEN.10373.

[2] R. Jayaprakash et al., "Two-Dimensional Organic-Exciton Polariton Lattice Fabricated Using Laser Patterning," ACS Photonics, vol. 7, no. 8, pp. 2273–2281, Aug. 2020, doi: 10.1021/acsphotonics.0c00867.

[3] N. C. Greenham et al., "Measurement of absolute photoluminescence quantum efficiencies in conjugated polymers," Chem. Phys. Lett., vol. 241, no. 1–2, pp. 89–96, Jul. 1995, doi: 10.1016/0009-2614(95)00584-Q.

Chapter 4: Investigating Amplified Spontaneous Emission from Organic Semiconductor Materials

4.1 Publication

The study of the copolymer, BN-PFO and the effect of BN content discussed in this chapter is published in the *Journal of Materials Chemistry C:*

Claronino, *et al.* Organic copolymer lasing from single defect microcavity fabricated using laser patterning. ***J. Mater. Chem. C***, 2023, **11**, 8204-8213.

4.2 Introduction

A key requirement for an organic semiconductor to be used as a laser active medium is to be able to undergo stimulated emission so that the light amplification of identical photons is greater than the optical losses. As discussed in Chapter 3, a common technique to identify materials that have potential application for lasing is the measurement of ASE. It has been shown that materials that have a low ASE threshold, give a strong indication for a low lasing threshold, where the lasing threshold is considerably lower than the ASE threshold, due to the increase in the confinement of photons inside the active layer. In this chapter, the ASE behaviour for a range of organic compounds are compared to identify materials for incorporation into a microcavity to achieve low threshold lasing. This chapter begins with the preliminary investigation of a fluorescent small molecule, Fluorescent Orange, that was dispersed into a polystyrene matrix at a range of concentrations. As solution processing limited the maximum concentration of the Fluorescent Orange in the matrix, the reduction in the ASE threshold was also constrained. Grazing incidence wide-angle X-ray scattering

(GIWAXS) was used to investigate the effects of aggregation of the Fluorescent Orange, on the molecular ordering of the film. Thermal evaporation of the pigment and bathocuproine (BCP) were found to further decrease the threshold. However, controlling the rates for the deposition limited the concentration that could be achieved. After this, another material (BN-PFO) was investigated that has been reported to have low lasing thresholds and demonstrates quasi-continuous wave (CW) lasing. Organic materials with reduced triplet formation have been reported to show lasing under quasi-CW conditions and are therefore promising candidates for electrical operation [1-4]. The polymer polyfluorene 2, 7-(9,9-dioctylfluorene (PFO) has been investigated for lasing applications, with modifications to its structure being explored as a means to improve both its lasing characteristics and its charge-carrier mobility [5]. Including binaphthyl (BN) spacer groups between the monomer units has been one of the most promising copolymer variants of PFO, where it is reports indicate that increasing the degree of BN copolymerisation decreases the lasing threshold [6]. It has been reported that the inclusion of BN spacer groups modifies the molecular packing of the polymer chains, causing a suppression in β-phase formation in spin-cast films. The reductions in the formation of the β-phase have been reported to improve its lasing performance [6].

In this chapter we also present a study on a polyfluorene copolymer (BN-PFO), specifically a poly[2,7-(9,9-dioctylfluorene)] with modified degrees (5.2, 9.8, or 12.7 mol%) of 6,6'-(2,2'-dioctyloxy-1,1'-binaphthyl) repeat units. Significantly, this copolymer has been reported to show low lasing thresholds and quasi-CW operation [7]. The current reports regarding lasing from BN-PFO have been with DFBs gratings, containing first and second-order periods [8], together with non-periodic circular gratings [9]. In the work described in this chapter, we investigate how the lasing performance of BN-PFO is affected by the relative concentration of the BN units and intermolecular packing. This study shows that increasing the relative fractions of BN spacer content in polydioctylfluorene (PFO) causes a decrease in its ASE threshold through suppression of intermolecular interactions.

At the end of this chapter one of the most promising organic small molecule laser materials is investigated; 2,4'-Bis(4-(9H-carbazol-9-yl)styryl)biphenyl (BSBCz). Not only has this small molecule demonstrated quasi-CW lasing under pulsed optical pumping due to its excellent triplet management, but it has also been claimed to undergo electrically driven lasing. Compared to the other materials studied in this chapter, BSBCz shows the lowest ASE threshold.

4.3 Amplified Spontaneous Emission

As discussed in Chapter 2, the four-level energy system of an organic semiconductor allows a population inversion when optically pumped. This population inversion allows for the amplification of light through stimulated emission (ASE). This process can be measured by exciting a region of an organic semiconductor with a laser that is focused with a cylindrical lens into a stripe [10]. An exciton within the stripe will emit light via spontaneous emission in a random direction. If this direction coincides with the axis of the excited stripe, the photon can stimulate another excited state to emit an identical photon. These identical photons will then waveguide through the stripe and undergo multiplication. This ASE exits from the edge of the stripe with a narrow linewidth and enhanced intensity.

To induce a population inversion in a film using a laser stripe, the medium needs to be pumped with an energy density that maintains the majority of excitons in an excited singlet state. This can be identified by a clear threshold where the amplification of identical photons occurs. This is evident by spectral narrowing and the increase in intensity of the emission.

For photons to waveguide through the film, a cut-off film thickness condition is defined by the emission wavelength and the refractive index of the film. The cut-off thickness (h_c) for a 0th order mode is given by the following expression where λ is the wavelength of the emission, n_f, n_s and n_a are the film, substrate and air refractive indices [11]:

$$\frac{h_c}{\lambda} = \frac{\tan^{-1}\left(\sqrt{\frac{n_s^2 - n_a^2}{n_f^2 - n_s^2}}\right)}{2\pi\sqrt{(n_f^2 - n_s^2)}} \tag{4.1}$$

Meeting the waveguiding condition is important for confining the emitted light within a thin film. Waveguiding occurs as the refractive index of the organic layer is higher than the substrate and air. Table 4.1shows the optical properties used to calculate the cut-off thickness for each material used in this chapter.

Table 4.1: Material refractive index at their ASE wavelength

Material	λ_{ASE} (nm)	n at λ_{ASE}	n Glass at λ_{ASE}	h_c (nm)
FO in PS	570	1.6	1.46	216
FO in BCP	613	1.7	1.46	114
BN-PFO	445	1.7	1.47	88
BSBCz	478	2	1.47	28

4.4 ASE Characterisation of Organic Semiconductors

4.4.1 Fluorescent Orange Perylene dye

The first material used in this study was the pigment dye, Fluorescent Orange, Anthra[2,1,9-def:6,5,10-d´e´f´]diisoquinoline1,3,8,10(2H,9H)-tetrone,2,9-bis[2,6-bis(1-

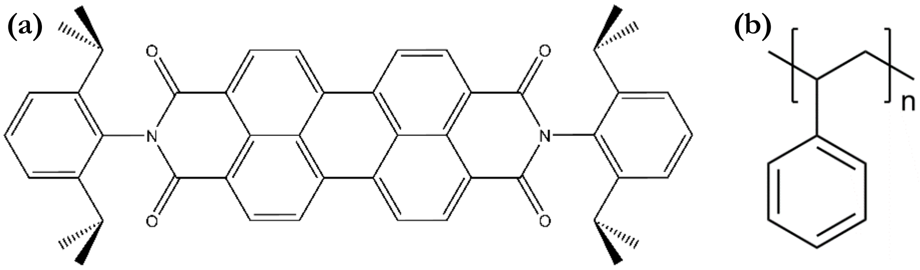

Figure 4.1: Chemical structure of a) Perylenediimide dye, Fluorescent Orange b) polystyrene used as the matrix.

methylethyl)phenyl] purchased from Kremer Pigment GmbH & Co.KG. The chemical structure for this pigment is illustrated in Figure 4.1. Pigment dyes dissolved in an organic matrix have been frequently used as the active medium for organic lasers due to their commercial availability, stability and favourable optical properties [12-15]. The commercial availability and simple processability of this dye made it the ideal laser material.

Solutions were prepared with a concentration of 5%, 10% and 12% Fluorescent Orange in a 35mg/ml solution of polystyrene (PS) in dichloromethane (DCM). Both PS (M = 170 000 g mol^{-1}) and DCM were purchased from Sigma-Aldrich. Solutions were stirred for 1 hour on a hot plate at a temperature of 36°C at 700 rpm. Thin films were cast by spin coating solutions of each concentration onto quartz substrates following the process outlined in Chapter 3, creating films with an approximate thickness of 400 nm. To characterise the photophysical properties, absorption and photoluminescence measurements were performed using a Horiba Fluoromax 4 (more details given in Chapter 3) with thin films consisting of 5% and 10% Fluorescent Orange. As shown in Figure 4.2a the spectral shape of the absorption remains relatively unchanged for both concentrations, but the absorption for the 10% film is around twice that of the 5% film. The PL spectral shape shows a significant change, with the low-concentration Fluorescent Orange film having clear 0-0 and 0-1 vibronic transitions (see Figure 4.2b). This is less evident in the 10% film where typical vibronic progression of

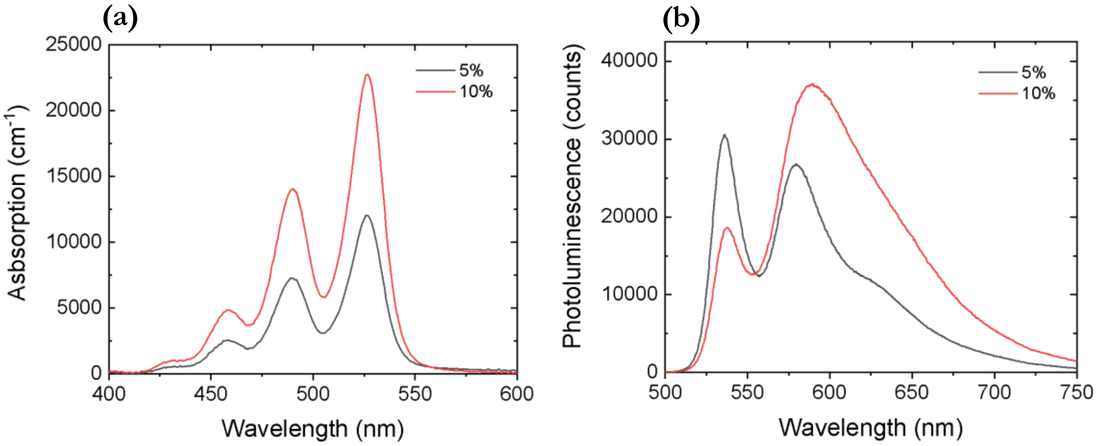

Figure 4.2: (a) Absorption and (b) photoluminescence properties of Fluorescent Orange thin film dispersed in a PS matrix at 5 and 10% wt.

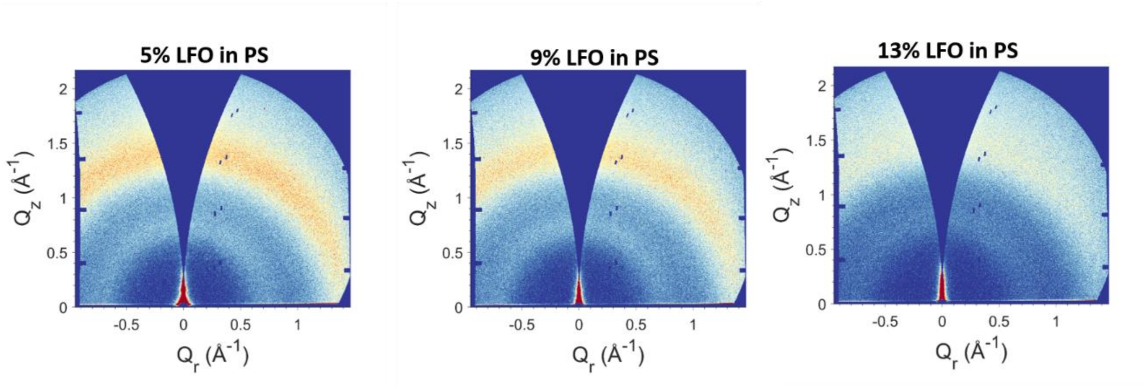

Figure 4.3: 2D GIWAXS patterns for Fluorescent Orange in PS at a concentration of a) 5% b) 9% and c) 12%

a typical isolated molecule is not observed, indicating the formation of excimers due to the increase in Fluorescent Orange aggregation [16].

The aggregation from increasing the concentration of perylene dyes dispersed in a matrix has been widely reported in the literature, with extensive studies using PS and polymethyl methacrylate (PMMA) [13]. In this study, GIWAXS was used to probe the molecular order and packing of the films with concentrations of 13%, 9% and 5% Fluorescent Orange in PS. Figure 4.3 shows 2D GIWAXS patterns of the three concentrations of Fluorescent Orange dispersed in a PS matrix with corresponding 1D azimuthally integrated intensity profiles shown in Figure 4.4. The weak intensity and broad rings in the 2D GIWAXS suggests a random, disordered configuration of the PS with respect to the substrate (see Figure 4.4).

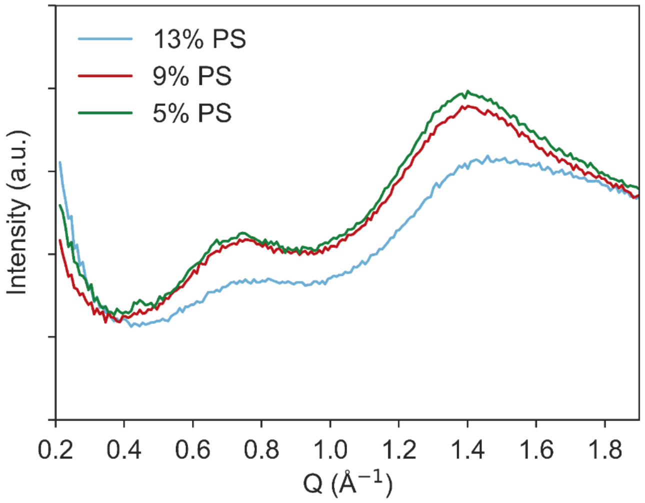

Figure 4.4: Normalised 1D azimuthally integrated intensity profiles of Fluorescent Orange dispersed in PS at concentrations of 13, 9 and 5%

The two weak intensity rings that are present for each concentration are Q = 0.7 Å^{-1} and 1.4 Å^{-1}. The scattering feature at Q = 1.4 Å^{-1} (d = 4.49 Å) can be attributed to the in-plane stacking of the polystyrene. An additional peak at 0.7 Å corresponds to a spacing of 8.98 Å. This most likely results from an out of plane stacking along the molecular long axis. A decrease in the intensity of the scattering rings as the concentration is increased suggests that there is an increase in PS molecular disorder within the films. This increase in disorder indicates that the aggregation of the Fluorescent Orange molecules disrupts the staking of the PS polymer chains.

Studies have shown that an increase in aggregation has a negative effect on photoluminescence, where previous reports show a decrease in the PLQY with an increase in concentration [15]. For 5% and 12% concentration FO/PS films, there is a drop in the PLQY from 26% to 14%. As expected, increasing the dye concentration also has a negative effect on the ASE threshold. To measure this, the ASE setup discussed in Chapter 2 was used to characterise the ASE behaviour for films with 12%, 10% and 5% FO concentration. Samples were excited with a laser stripe from a 355 nm Nd:YAG (100Hz, 350 ps) laser focused with a cylindrical lens. The waveguided emission was collected from the edge of the thin film with a fibre optic cable connected to a spectrometer with a 300 mm^{-1} grating and

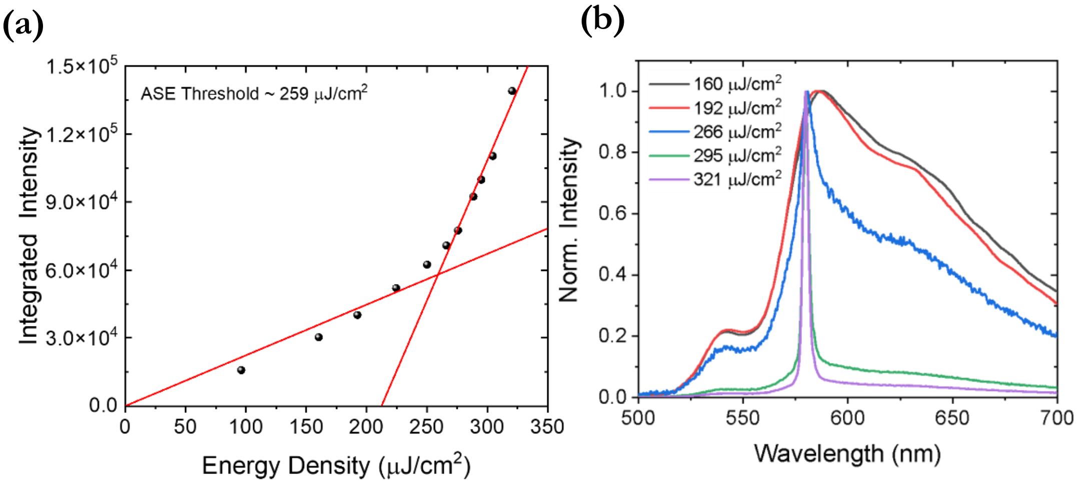

Figure 4.5: ASE characteristic for films containing 5% Fluorescent Orange in a PS matrix (a) Integrated intensity as a function of pump fluence (b) spectral captures showing spectral narrowing as pump fluence was increased.

entrance slit set to 50 μm. All ASE characterisation measurements were carried out in ambient conditions. The spectra captured as a function of pump fluence was integrated to sum all of the emission intensity. To calculate the energy density, the laser stripe area was measured to be 0.3 mm^2. For the 5% concentration films, a pump range from 100 to >300 μJ cm^{-2} was used to capture the change in emission intensity from the edge of the substrate. As the fluence of the pump laser was increased past a threshold of 259 μJ cm^{-2} a sudden increase in emission intensity was observed. Two emission regimes can be identified from the sudden change in the output efficacy; one where spontaneous emission dominates below the pump threshold, and one where stimulated emission dominates after. Two linear fits of these regimes are also shown in Figure 4.5a and the intercept of the two fitted lines was used to determine the threshold. This is supported by changes in spectra shown in Figure 4.5b that illustrates the sudden collapse in linewidth of the emission above threshold. This narrowing is strong evidence of stimulated emission, and signifies a population inversion within the excitation area. The collapse in the emission centred on the 0-1 vibronic transition is typical for ASE and here it is observed at 580 nm.

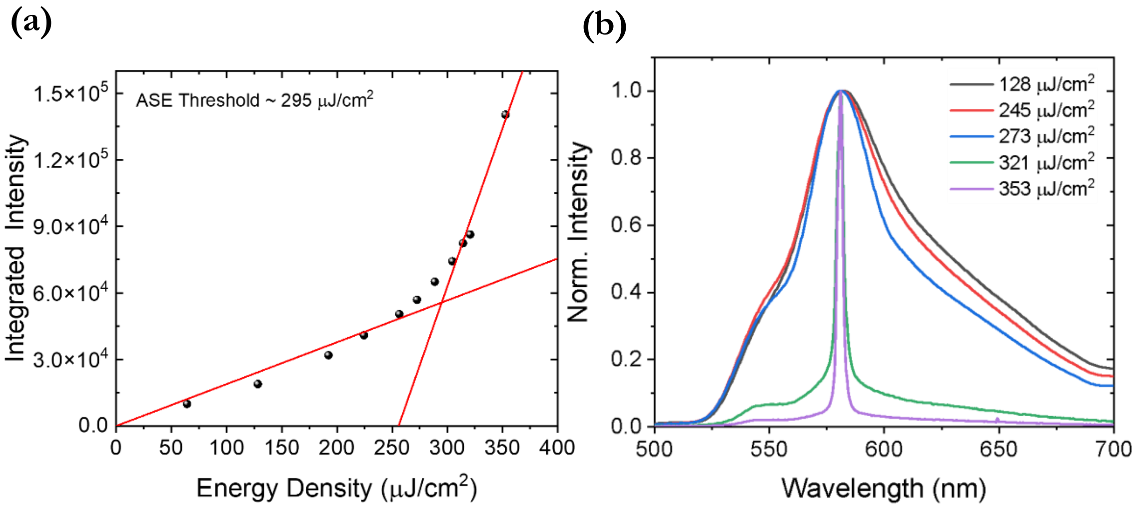

Figure 4.6: ASE characteristic for films containing 9% Fluorescent Orange in a PS matrix (a) Integrated intensity as a function of pump fluence (b) spectral captures showing spectral narrowing as pump fluence was increased.

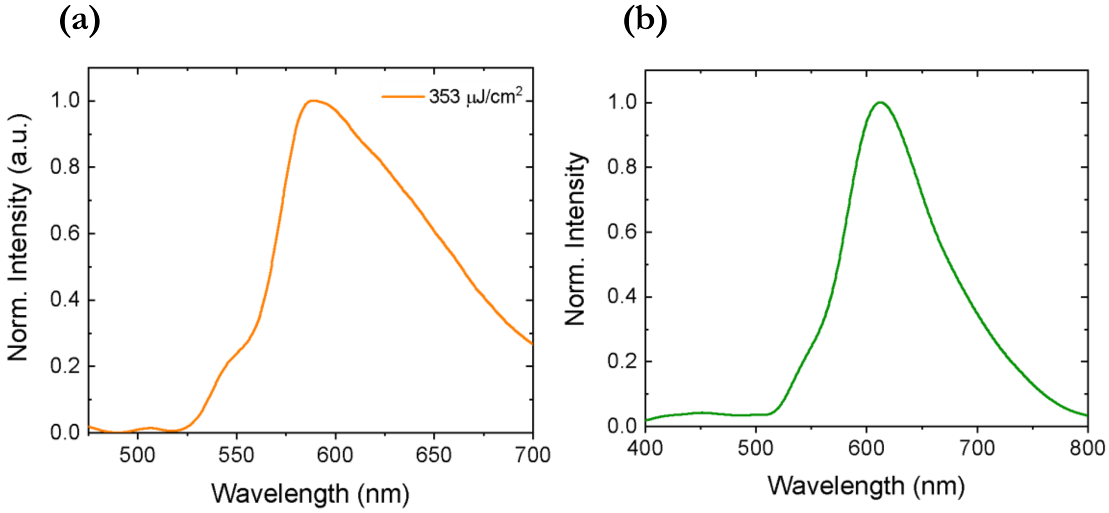

Figure 4.7: Emission spectra for 12% Fluorescence Orange films in a matrix of (a) PS (b) PMMA at a high pump fluence.

Increasing the Fluorescent Orange dye concentration to 9%, there is a significant increase in the ASE threshold. The input-output characteristics for the 9% film is shown in Figure 4.6a were the pump fluence range was 50-350 μJ cm^{-2}. Here it is also a clear that there is a sudden increase in the observed emission intensity above a threshold of 295 μJ cm^{-2}. As expected, this threshold is larger than that in the 5% concentration film (259 μJ cm^{-2}). Again, above threshold there is also clear narrowing in the emission spectra as shown in Figure 4.6b where the spectra collapses to 580 nm.

When the concentration of Fluorescence Orange was increased to 12%, no spectral narrowing was observed, as demonstrated in Figure 4.7a. This figure shows that even when pumping the film with the maximum power output of the pump laser (353 μJ cm^{-2}), there is no evidence of ASE. This suggests that either ASE is not possible, or that its threshold is beyond the capability of the setup. To investigate if changing the matrix would enable ASE to be generated at a 12% concentration, the matrix was changed to PMMA. For this, Fluorescence Orange was dispersed at 12% by mass in a 35 mg/ml solution of PMMA in DCM. Using the ASE setup, Figure 4.7b shows the spectra when pumping at maximum pump power. Again, ASE was also not observed in the PMMA matrix. For both 12%

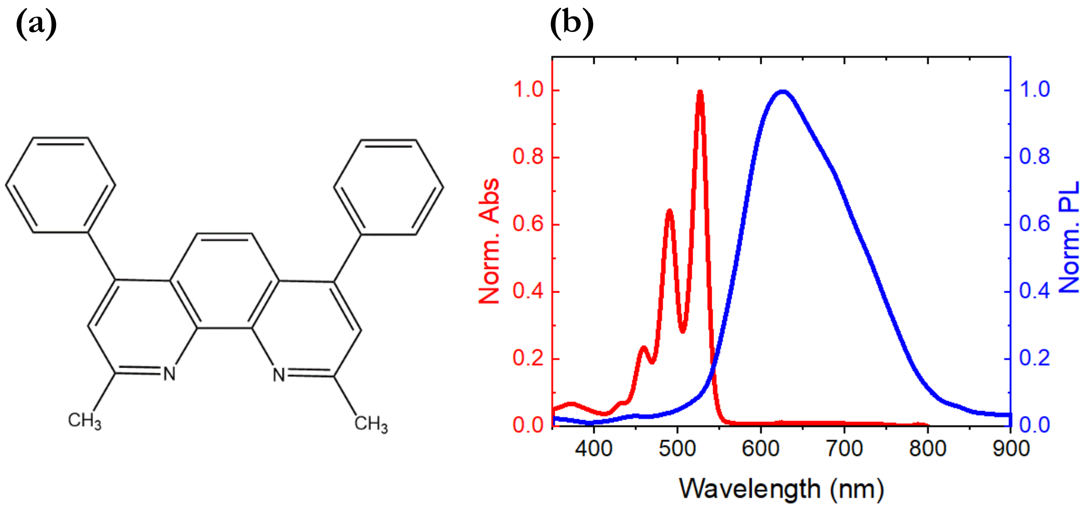

Figure 4.8: (a) Chemical structure of BCP (b) normalised absorption and PL for ~12% Fluorescence Orange in BCP.

concentration in PS and PMMA the solutions appeared cloudy. Due to the observable aggregation in the 12% solution, concentrations above this were not tested.

Increasing the concentration of the FO in solution caused aggregation, and therefore reduced the quality of the films. To avoid this the deposition method was changed to thermal evaporation with a second material. This allowed an increase in Fluorescent Orange concentration without the formation of aggregates as observed in solution. To see if ASE at a 12% concentration is possible, the small molecule bathocuproine was used as a matrix (BCP, Figure 4.8a). The BCP was purchased from Ossila with a 99.5% purity. Both molecules were co-thermally evaporated in a vacuum with the deposition process outlined in Chapter 3. The base pressure for this co-evaporation was 2.6 × 10^{-6} mbar and the rates for BCP and Fluorescent Orange were 1.0 and approximately 0.12 Ås^{-1} respectively to give a final film thickness of 200 nm. The absorption and PL for this ~12% BCP:Fluorescent Orange film is shown in Figure 4.8b. Compared with the PS matrix films, there is a red shift in the PL, by 90 nm creating an increased Stoke Shifts.

The input-output characteristics for the BCP:Fluorescent Orange (12%) film excited with a pump fluence range from 10 – 70 μJ cm^{-2} are shown in Figure 4.9a. This shows an increase in the output intensity and spectral narrowing (Figure 9b). Changing the matrix to a BCP

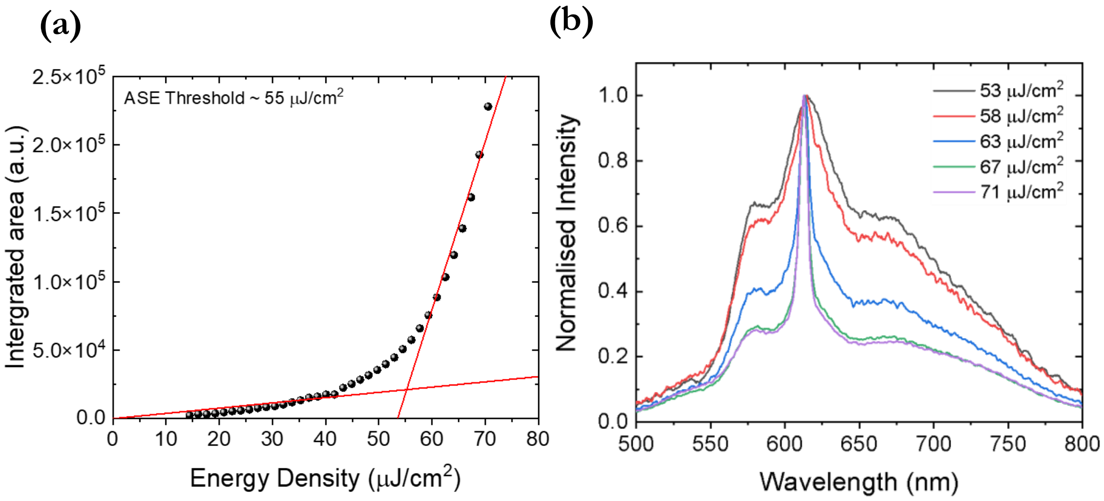

Figure 4.9: ASE characteristic for films containing ~12% Fluorescent Orange in a BCP matrix (a) Integrated intensity as a function of pump fluence (b) spectral captures showing spectral narrowing as pump fluence was increased.

blend led to an ASE threshold of 55 μJ cm^{-2}, this is 4 times lower than the lowest solution processed threshold. Further decreasing the concentration theoretically should result in lower thresholds, however, due to organic film quality being highly dependent on deposition rates, changing the rate for BCP was not considered. As for changing the deposition rate of Fluorescent Orange, the rate used was very low and controlled manually. If this rate was further reduced, it would not be possible to report the film concentration with a measureable degree of confidence.

4.4.2 BN-PFO

BN-PFO was the second material investigated in this study. This copolymer consists of polyfluorene with binaphthyl spacer groups (shown in Figure 4.10) and is in the small group of organic materials that has reported quasi-CW lasing in a grating resonator. Operating in this quasi-CW regime shows that this material has excellent triplet management and therefore,

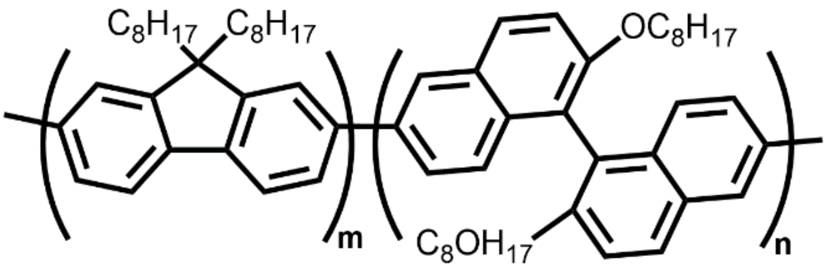

Figure 4.10: Chemical structure of BN-PFO.

makes this material an excellent candidate for electrical operation. The synthesis of BN-PFO was performed by our collaborators (T. Jessewitsch & U. Scherf) using Yamamoto-type coupling with racemic binaphthyl monomer with the corresponding molecular weights: 5.2% (M_n = 94.8 kDa, M_w = 178 kDa), 9.8% (M_n = 68.3 kDa, M_w = 131 kDa), and 12.7% (M_n = 80.7 kDa, M_w=158 kDa). The molecular weights were measured using gel permeation chromatography in solutions with a concentration of 0.5 mg/mL in chloroform. Proton nuclear magnetic resonance (H-NMR) was used to calculate the BN content. The range selected for the BN concentrations was chosen, as it has been reported that for BN concentrations above 12.7%, the backbone of the copolymer was modified to the extent that charge conjugation was lost. To deposit thin films, BN-PFO was dissolved in a solution of toluene at a concentration of 35 mg/mL and stirred on a hotplate for 1 hour at a temperature of 65 °C in air. This solution was then spin-coated at room temperature onto a substrate at spin-speeds of 3000 rpm, creating films having a thickness of approximately 120 nm. The absorption and PL of BN-PFO is shown in Figure 4.11. All concentrations absorb strongly in the UV, with PL showing typical 0-0, 0-1 and 0-2 vibronic transitions at 423, 447 and 478 respectively.

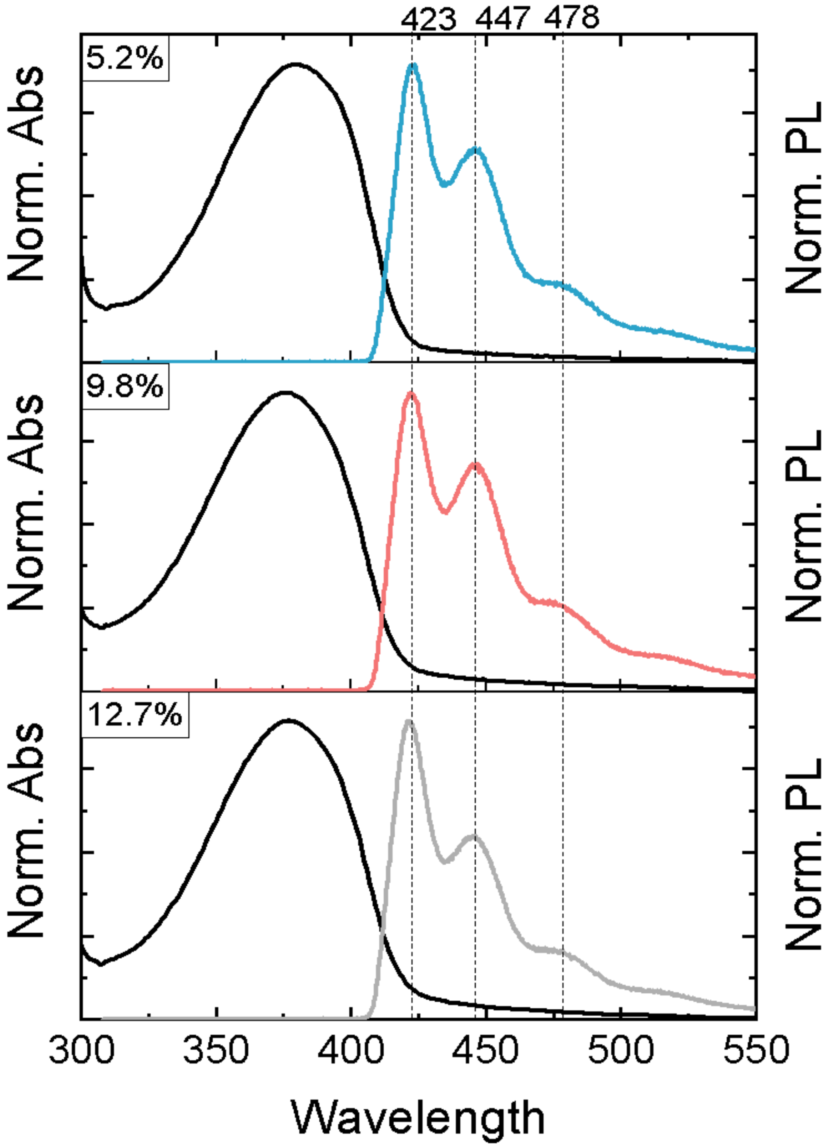

Figure 4.11: Normalised absorption and PL for BN-PFO with BN concentrations of 5.2%, 9.8% and 12.7%

4.4.3 Binaphthyl Spacer Concentration Effect on ASE Threshold

It has been well documented that the molecular packing of PFO thin films show coexisting amorphous (α), crystalline (β) and intermediate (γ) phases as well as nematic liquid crystalline phases [17-22]. Solution deposited PFO films are typically dominated by the α-phase but the more crystalline β-phase can be induced and is controlled through careful choice of casting solvent and post-deposition solvent and thermal treatments [19, 23-25]. In order to understand the impact of the BN spacer content on the molecular packing of neat BN-PFO

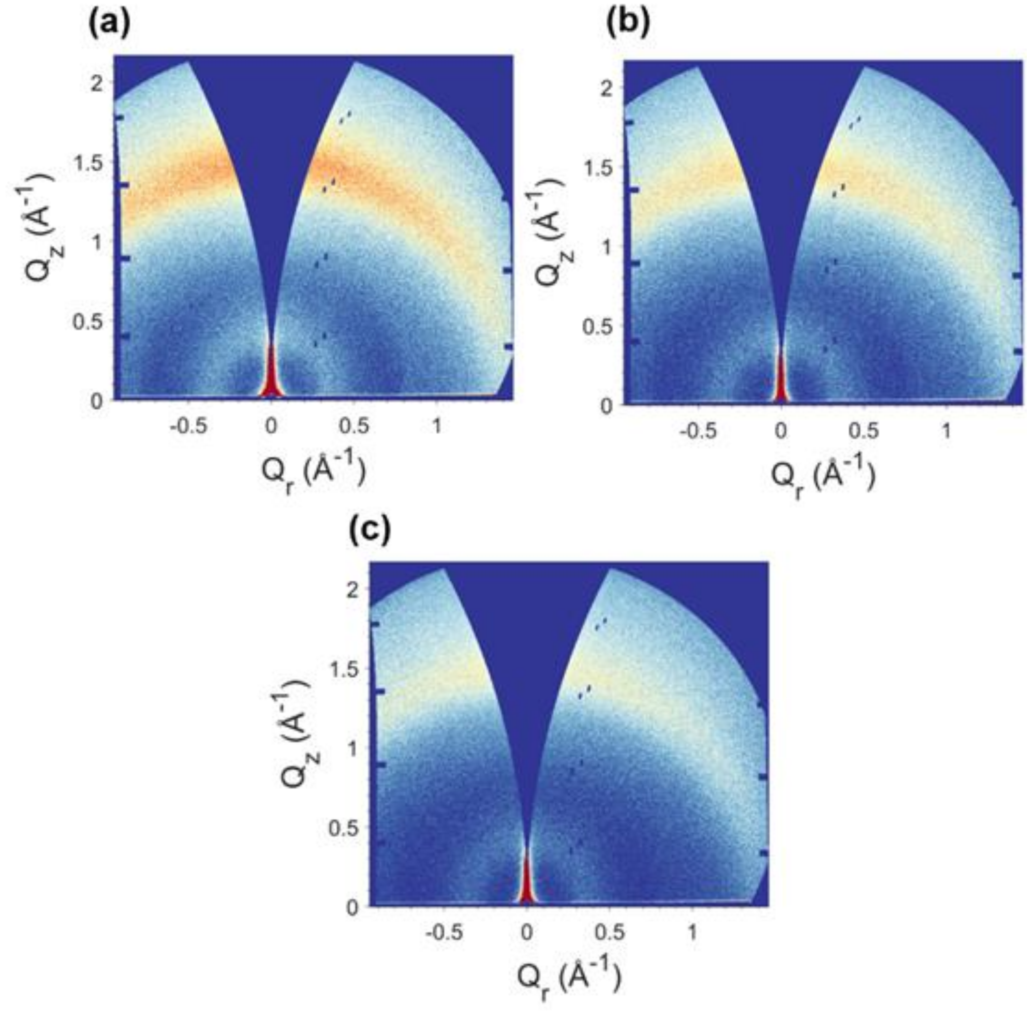

Figure 4.12: 2D GIWAXS patterns of BN-PFO films with binaphthyl (BN) spacer contents of (a) 5.2 Mol%, (b) 9.8 Mol% and (c) 12.7 Mol%.

films, GIWAXS measurements were performed with relative BN fractions of 5.2, 9.8 and 12.7 mol%.

The typical 2D GIWAXS patterns of BN-PFO with varying fractions of BN content are shown in Figure 4.12, along with corresponding azimuthally integrated intensity profiles in Figure 4.13a. Each 2D GIWAXS pattern consists of two, weak intensity rings at $Q = 0.40$ Å^{-1} and $Q = 1.47$ Å^{-1} corresponding to characteristic length scales (*d*-spacing's) of 15.7 Å and 4.3 Å respectively. In Figure 13a a weak-intensity shoulder is also visible in the 1D intensity profiles at $Q \sim 1.1$ Å^{-1} ($d = 5.7$Å). The stronger intensity 4.3 Å scattering feature has previously been assigned to π-π stacking of the PFO octyl side chains in the polymer backbone direction [18]. The larger 15.7 Å signature is similar to values reported for the edge-

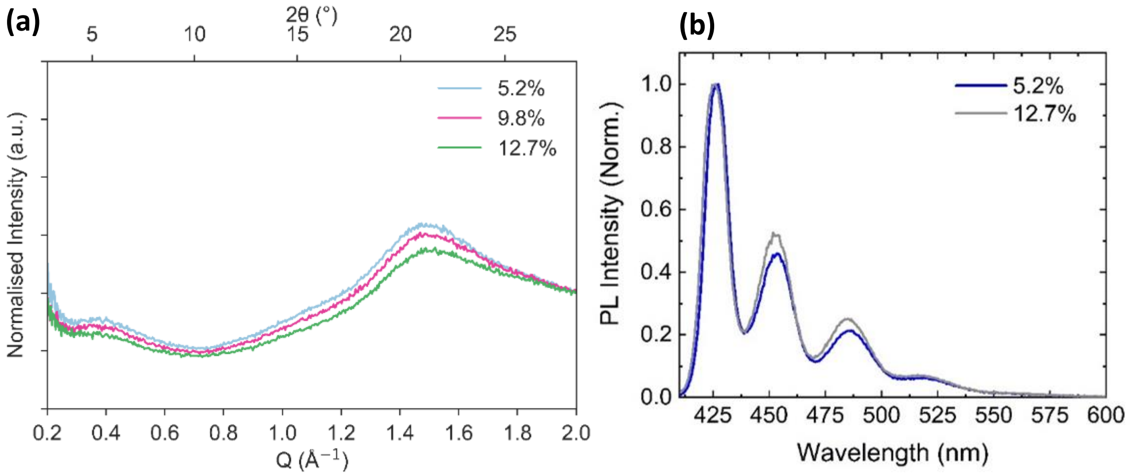

Figure 4.13: (a) Corresponding normalised 1D azimuthally integrated intensity profiles. The higher BN concentration reduces the β-phase formation in the BN-PFO films. (b) Normalised low temperature PL emission for BN-PFO 5.2 Mol% (blue) and 12.7 Mol% (grey) at 30K.

to-edge lateral stacking distance of PFO and its derivatives [18, 26]. The appearance of weak intensity, broad rings and lack of azimuthal dependence suggests BN-PFO adopts a disordered configuration with no preferential molecular orientation with respect to the substrate, and this is characteristic of the amorphous α-phase as expected for spin-coated PFO films. Interestingly, there is a decrease in scattering intensity of the 1.47 Å^{-1} feature with increasing BN spacer content, indicating that the BN moieties suppress π-π stacking and result in increased molecular disorder.

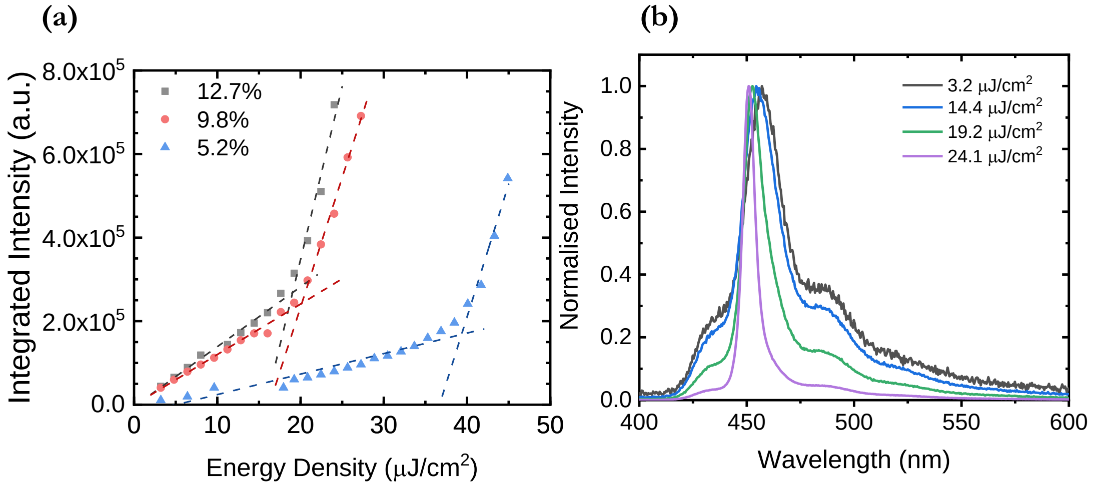

Figure 4.14: (a) ASE integrated intensity as a function of energy density for BN-PFO with different concentrations of BN (b) BN-PFO (12.7%) ASE spectra linewidth narrowing as pump fluence increases.

Previous reports show that the insertion of BN spacer units along the polymer chain suppresses the formation of the PFO β-phase [6]. However, the PL emission from all the BN-PFO samples explored is characteristic of the α-phase (even at low temperatures), suggesting that for the films studied here have almost completely no β-phase (see Figure 4.13b).

The ASE threshold was measured for BN-PFO samples containing 5.2%, 9.8% and 12.7% BN units to investigate the effect of the BN concentration on the lasing threshold. Here, ASE originates from the same processes that generate lasing and is, therefore, a good technique to explore the ability of a material to exhibit optical gain. To measure ASE, thin films of BN-PFO at each BN concentration were measured using the ASE setup detailed in Chapter 3. Figure 4.14a shows the output characteristics as a function of excitation energy density for each BN concentration. For each concentration, it is evident that there is a change of gradient, indicative of a changeover from spontaneous emission regime to stimulated emission. This change can be clearly seen in Figure 4.14b**,** with the linewidth of the emission narrowing as stimulated emission dominates. At this point, a population inversion is created, with net gain exceeding losses. Figure 4.15 plots the ASE threshold for each BN concentration. Here it can be seen that there is an almost 2-times reduction in ASE threshold

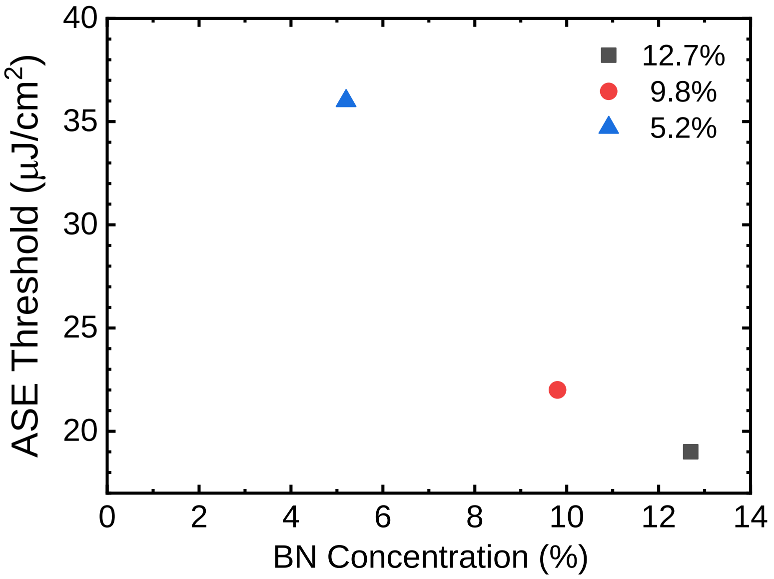

Figure 4.15: ASE threshold as a function of BN concentration (12.7% = 19 μJ cm-2 , 9.8% = 22 μJ cm-2, 5.2% = 36 μJ cm-2).

between the polymers having the 12.7% and 5.2% BN concentrations. This result is consistent with other reports [6] in which similar reductions in lasing threshold are reported for BN-PFO with various concentrations of BN units, where the lower thresholds are attributed to a reduction in β-phase formation. However, from our results, it is not believed that the films contain any appreciable concentration of β-phase and thus a different explanation is needed. Instead, it is suspected that the increased molecular disorder as evidenced by GIWAXS data, in addition to the 'dilution' and conjugation-breaking effects caused by the increased BN-fraction, enhances exciton diffusion at high BN concentration. This results in decreased exciton-exciton interactions that cause quenching of singlet-excited states that are fundamental to the lasing process.

4.4.4 BSBCz

We have also investigated the small molecule 2,4'-Bis(4-(9H-carbazol-9-yl)styryl)biphenyl (BSBCz). The chemical structure for BSBCz is shown in Figure 4.16. BSBCz has been reported to have excellent optical properties, one of the lowest reported lasing thresholds, and is one of the few organic semiconductors to demonstrate quasi-CW lasing in a blend with CBP [1, 27-29]. This material was purchased from LumTec having >99% purity and used without further processing. Thin films of BSBCz were thermally evaporated in a vacuum at a rate of 2 Ås^{-1} at a base pressure of 2.7×10^{-7} mbar to achieve a thickness of 100 nm. To investigate the molecular orientation and packing of BSBCz in thin films, GIWAXS was performed. Figure 4.17a illustrates the 2D GIWAXS pattern of BSBCz with Figure 4.17b showing the corresponding azimuthally integrated intensity profile. Here the 2D GIWAXS

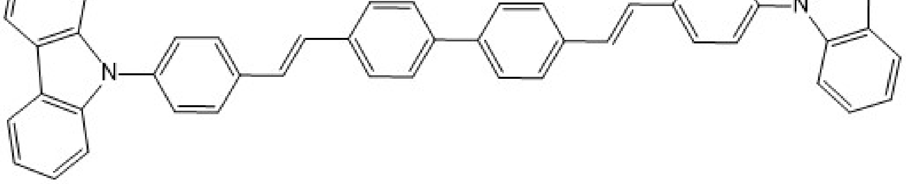

Figure 4.16: Chemical structure of the small molecule BSBCz.

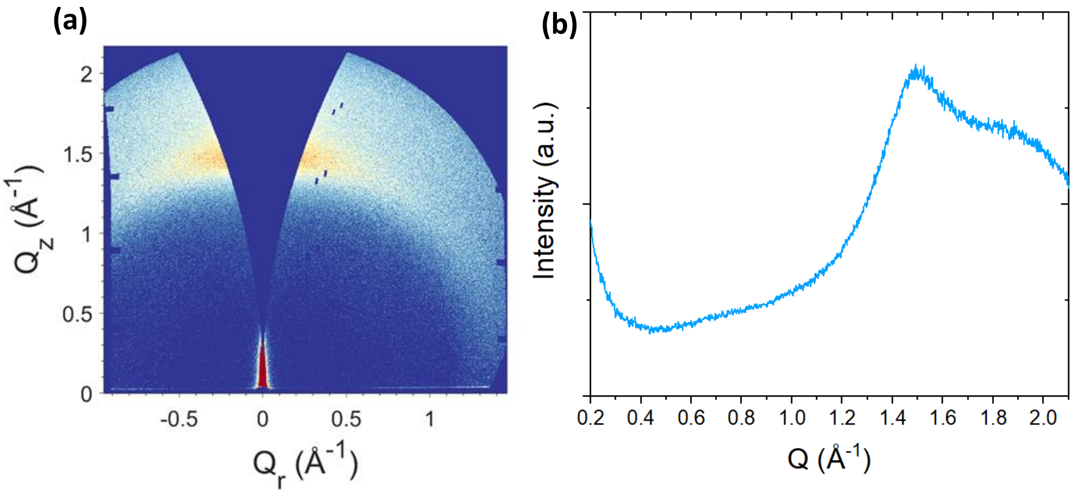

Figure 4.17: (a) 2D GIWAXS patterns of neat BSBCz thin film (b) Corresponding normalised 1D azimuthally integrated intensity profile.

pattern consists of a single intensity ring at Q ~ 1.49 Å^{-1} that corresponds to a characteristic length scale of 4.49 Å. This intensity ring is relatively narrow and suggests that the molecules adopt a face-on orientation. This is in accordance with the literature where neat films of BSBCz molecules were reported to lie parallel to the substrate [30].

The photophysical properties of BSBCz are shown in Figure 4.18 where absorption occurs in the UV and emission is deep blue. Unlike the other materials, this material has a large Stoke Shift, and therefore has minimal losses caused by reabsorption, making this very

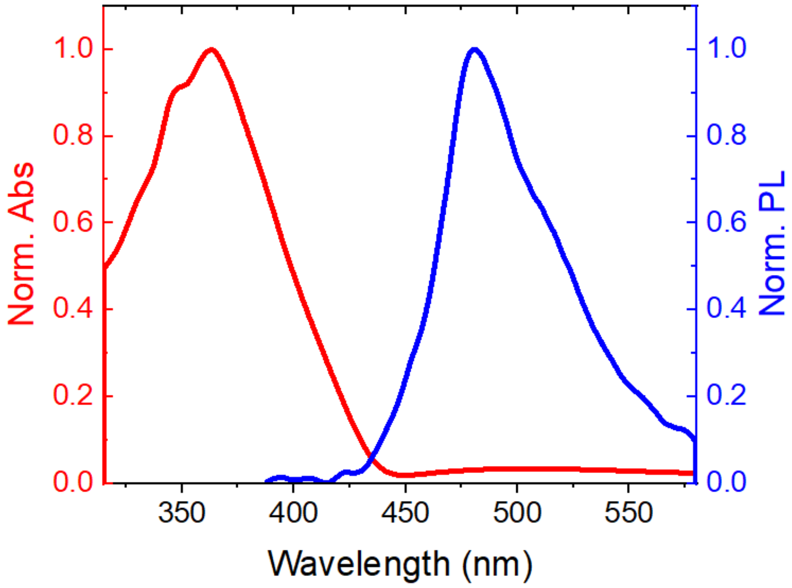

Figure 4.18: Absorption and photoluminescence for BSBCz thin film.

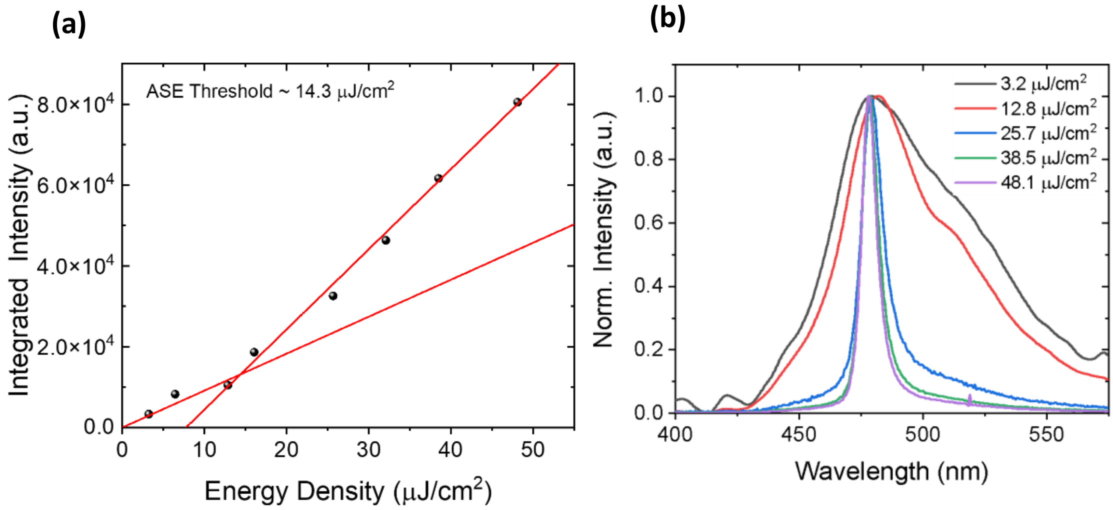

Figure 4.19: (a) ASE integrated intensity as a function of energy density for BSBCz (b) BSBCz ASE spectra linewidth narrowing as pump fluence increases.

favourable for lasing. Using the ASE setup, 100 nm thick films of neat BSBCz were excited with a 355 nm Nd:YAG (100Hz, 350 ps) laser with a pump fluence range of 2 to 50 μJ cm^{-2}. The integrated intensity as a function of pump fluence is shown in Figure 4.19a. Using two linear fits on the spontaneous and stimulated emission regimes, a threshold of 13.8 μJ cm^{-2} was determined. As the sudden increase in output intensity is less well defined than in previous materials, stimulated emission can also be evidenced by the spectral narrowing as shown in Figure 4.19b.

Compared to the literature, ASE thresholds for neat films of BSBCz have been reported to be as low as 0.63 μJ cm^{-2} [31]. The threshold reported in this study is an order of magnitude higher (13.8 μJ cm^{-2}), however, these reported measurements were performed in a nitrogen environment with as laser pulse width of 0.8 nm. The films explored in this study were measured in ambient conditions and the photo-oxidation of the films and longer pulse width (3 ns) possibly accounts for the increase in the threshold.

4.5 Summary

This chapter investigated the ASE behaviour of three different types of organic compounds. The first was Fluorescent Orange, a pigment dye dispersed in a PS matrix that at high concentrations causes aggregation within the matrix and leads to higher ASE thresholds. The lowest threshold from spin coating Fluorescent Orange was 259 μJ cm^{-2}. By using co-evaporation with BCP, the threshold for ASE was reduced to 55 μJ cm^{-2}. ASE from films of the co-polymer BN-PFO was then explored and it was demonstrated that increasing the relative fraction of BN to PFO along the molecular backbone increased molecular disorder. As a result of such enhanced disorder, a reduction in the threshold for ASE by 1.9 times to 19 μJ cm^{-2} was observed. Finally, the ASE of the small molecule BSBCz was studied. This had the lowest ASE threshold (13.8 μJ cm^{-2}) of the compounds measured. This promising material has impressive optical properties, with a large Stokes shift, high PLQY and reported quasi-CW lasing. As BN-PFO (12%) and BSBCz, both have the two lowest observed ASE thresholds, they were chosen for further study in planar microcavity resonators as discussed in the next chapter. A summary of the ASE characteristics for each material is shown below in Table 4.2.

Table 4.2: Summary of the ASE properties of all materials studied in this chapter.

Material	**λ_{ASE} (nm)**	**E_{th}^{ASE} (μJ cm^{-2})**	**literature E_{th}^{ASE} (μJ cm^{-2})**
FO (PS)	570	259	300 [15]
FO (BCP)	613	55	-
BN-PFO (5.2%)	445	36	-
BN-PFO (9.8%)	450	22	-
BN-PFO (12.7%)	450	19	-
BSBCz	478	14	0.63 [31]

4.6 References

[1] A. S. D. Sandanayaka et al., "Quasi-Continuous-Wave Organic Thin-Film Distributed Feedback Laser," Adv. Opt. Mater., vol. 4, no. 6, pp. 834–839, 2016, doi: 10.1002/adom.201600006.

[2] A. S. D. Sandanayaka et al., "Improvement of the quasi-continuous-wave lasing properties in organic semiconductor lasers using oxygen as triplet quencher," Appl. Phys. Lett., vol. 108, no. 22, p. 223301, May 2016, doi: 10.1063/1.4952970.

[3] T. Rabe et al., "Quasi-continuous-wave operation of an organic thin-film distributed feedback laser," Appl. Phys. Lett., vol. 89, no. 8, p. 081115, Aug. 2006, doi: 10.1063/1.2337873.

[4] H. Nakanotani, C. Adachi, S. Watanabe, and R. Katoh, "Spectrally narrow emission from organic films under continuous-wave excitation," Appl. Phys. Lett., vol. 90, no. 23, pp. 4–7, 2007, doi: 10.1063/1.2746958.

[5] B. K. Yap, R. Xia, M. Campoy-Quiles, P. N. Stavrinou, and D. D. C. Bradley, "Simultaneous optimization of charge-carrier mobility and optical gain in semiconducting polymer films," Nat. Mater., vol. 7, no. 5, pp. 376–380, May 2008, doi: 10.1038/nmat2165.

[6] T. Rabe et al., "Threshold Reduction in Polymer Lasers Based on Poly(9,9-dioctylfluorene) with Statistical Binaphthyl Units," Adv. Funct. Mater., vol. 15, no. 7, pp. 1188–1192, Jul. 2005, doi: 10.1002/adfm.200500023.

[7] M. Lehnhardt, T. Riedl, U. Scherf, T. Rabe, and W. Kowalsky, "Spectrally separated optical gain and triplet absorption: Towards continuous wave lasing in organic thin film lasers," Org. Electron., vol. 12, no. 8, pp. 1346–1351, 2011, doi: 10.1016/j.orgel.2011.05.005.

[8] C. Karnutsch et al., “Low threshold blue conjugated polymer lasers with first- and second-order distributed feedback,” Appl. Phys. Lett., vol. 89, no. 20, p. 201108, Nov. 2006, doi: 10.1063/1.2390644.

[9] T. Wellinger et al., “Blue-light-emitting polymer lasers with non-periodic circular Bragg resonators,” in Organic Optoelectronics and Photonics III, P. L. Heremans, M. Muccini, and E. A. Meulenkamp, Eds., Apr. 2008, p. 699907. doi: 10.1117/12.781033.

[10] K. L. Shaklee and R. F. Leheny, “Direct determination of optical gain in semiconductor crystals,” Appl. Phys. Lett., vol. 18, no. 11, pp. 475–477, Jun. 1971, doi: 10.1063/1.1653501.

[11] E. M. Calzado, J. M. Villalvilla, P. G. Boj, J. A. Quintana, and M. A. Díaz-García, “Concentration dependence of amplified spontaneous emission in organic-based waveguides,” Org. Electron., vol. 7, no. 5, pp. 319–329, Oct. 2006, doi: 10.1016/J.ORGEL.2006.04.002.

[12] J. A. Quintana et al., “An Efficient and Color-Tunable Solution-Processed Organic Thin-Film Laser with a Polymeric Top-Layer Resonator,” Adv. Opt. Mater., vol. 5, no. 19, p. 1700238, Oct. 2017, doi: 10.1002/ADOM.201700238.

[13] M. G. Ramírez et al., “Improved performance of perylenediimide-based lasers,” J. Mater. Chem. C, vol. 1, no. 6, pp. 1182–1191, Jan. 2013, doi: 10.1039/C2TC00383J.

[14] Marco Anni. Sandro Lattante, Organic Lasers: Fundamentals, developments, and applications. 2018. Accessed: Nov. 16, 2023. [Online]. Available: https://www.routledge.com/Organic-Lasers-Fundamentals-Developments-and-Applications/Anni-Lattante/p/book/9789814774468

[15] R. Munoz-Mármol et al., “Influence of Blending Ratio and Polymer Matrix on the Lasing Properties of Perylenediimide Dyes,” J. Phys. Chem. C, vol. 122, no. 43, pp. 24896–

24906, Nov. 2018, doi: 10.1021/ACS.JPCC.8B06925/ASSET/IMAGES/LARGE/JP-2018-06925J_0008.JPEG.

[16] R. O. Al-Kaysi, T. Sang Ahn, A. M. Müller, and C. J. Bardeen, "The photophysical properties of chromophores at high (100 mM and above) concentrations in polymers and as neat solids," Phys. Chem. Chem. Phys., vol. 8, no. 29, pp. 3453–3459, Jul. 2006, doi: 10.1039/B605925B.

[17] W. C. Tsoi and D. G. Lidzey, "Raman spectroscopy of fluorene oligomers in the α-, β- and γ-phases," J. Phys. Condens. Matter, vol. 20, no. 12, p. 125213, Mar. 2008, doi: 10.1088/0953-8984/20/12/125213.

[18] M. Grell, D. D. C. Bradley, G. Ungar, J. Hill, and K. S. Whitehead, "Interplay of Physical Structure and Photophysics for a Liquid Crystalline Polyfluorene," Macromolecules, vol. 32, no. 18, pp. 5810–5817, Sep. 1999, doi: 10.1021/ma990741o.

[19] P. Wilhelm, D. Blank, J. M. Lupton, and J. Vogelsang, "Control of Intrachain Morphology in the Formation of Polyfluorene Aggregates on the Single - Molecule Level," ChemPhysChem, vol. 21, no. 10, pp. 961 - 965, May 2020, doi: 10.1002/cphc.202000118.

[20] M. Misaki et al., "Single-Crystal-like Structure of Poly(9,9-dioctylfluorene) Thin Films Evaluated by Synchrotron-Sourced Grazing-Incidence X-ray Diffraction," Polym. J., vol. 39, no. 12, pp. 1306–1311, Dec. 2007, doi: 10.1295/polymj.PJ2007063.

[21] M. Ariu, D. G. Lidzey, M. Sims, A. J. Cadby, P. A. Lane, and D. D. C. Bradley, "The effect of morphology on the temperature-dependent photoluminescence quantum efficiency of the conjugated polymer poly(9, 9-dioctylfluorene)," J. Phys. Condens. Matter, vol. 14, no. 42, pp. 9975–9986, Oct. 2002, doi: 10.1088/0953-8984/14/42/310.

[22] A. L. T. Khan, P. Sreearunothai, L. M. Herz, M. J. Banach, and A. Köhler, “Morphology-dependent energy transfer within polyfluorene thin films,” Phys. Rev. B, vol. 69, no. 8, p. 085201, Feb. 2004, doi: 10.1103/PhysRevB.69.085201.

[23] A. Perevedentsev et al., “Dip-pen patterning of poly(9,9-dioctylfluorene) chain-conformation-based nano-photonic elements,” Nat. Commun., vol. 6, no. 1, p. 5977, Jan. 2015, doi: 10.1038/ncomms6977.

[24] A. Perevedentsev, N. Chander, J. S. Kim, and D. D. C. Bradley, “Spectroscopic properties of poly(9,9-dioctylfluorene) thin films possessing varied fractions of β-phase chain segments: enhanced photoluminescence efficiency via conformation structuring,” J. Polym. Sci. Part B Polym. Phys., vol. 54, no. 19, pp. 1995–2006, 2016, doi: 10.1002/polb.24106.

[25] M. E. Caruso and M. Anni, “Real-time investigation of solvent swelling induced β-phase formation in poly(9,9-dioctylfluorene),” Phys. Rev. B, vol. 76, no. 5, p. 054207, Aug. 2007, doi: 10.1103/PhysRevB.76.054207.

[26] G. C. Faria et al., “A Multitechnique Study of Structure and Dynamics of Polyfluorene Cast Films and the Influence on Their Photoluminescence,” J. Phys. Chem. B, vol. 113, no. 33, pp. 11403–11413, Aug. 2009, doi: 10.1021/jp9043368.

[27] C. Adachi, A. S. D. Sandanayaka, S. A. Yazdani, M. Mamada, and T. Matsushima, “Materials Design of Organic Lasers Aimed at Low Lasing Threshold,” J. Synth. Org. Chem. Japan, vol. 80, no. 11, pp. 1065–1074, Nov. 2022, doi: 10.5059/YUKIGOSEIKYOKAISHI.80.1065.

[28] A. S. D. Sandanayaka et al., “Toward continuous-wave operation of organic semiconductor lasers,” Sci. Adv., vol. 3, no. 4, pp. 1–8, 2017, doi: 10.1126/sciadv.1602570.

[29] Y. Hu, F. Bencheikh, S. Chénais, S. Forget, X. Liu, and C. Adachi, "High performance planar microcavity organic semiconductor lasers based on thermally evaporated top distributed Bragg reflector," Appl. Phys. Lett., vol. 117, no. 15, p. 153301, Oct. 2020, doi: 10.1063/5.0016052.

[30] D. Yokoyama, A. Sakaguchi, M. Suzuki, and C. Adachi, "Horizontal orientation of linear-shaped organic molecules having bulky substituents in neat and doped vacuum-deposited amorphous films," Org. Electron., vol. 10, no. 1, pp. 127–137, 2009, doi: 10.1016/j.orgel.2008.10.010.

[31] M. Mamada, T. Fukunaga, F. Bencheikh, A. S. D. Sandanayaka, and C. Adachi, "Low Amplified Spontaneous Emission Threshold from Organic Dyes Based on Bis-stilbene," Adv. Funct. Mater., vol. 28, no. 32, pp. 1–9, 2018, doi: 10.1002/adfm.201802130.

Chapter 5: High-Performance Small Molecule and Polymer Planar Distributed Bragg Reflector Microcavity Lasers

This chapter investigates the organic materials that had the two lowest ASE thresholds as identified in Chapter 4. Here, we explore integrating both materials into a resonant cavity to create a laser device. The resonator chosen for this study was a planar microcavity that uses highly reflective mirrors to confine light inside the active layer. Microcavities were designed for single-mode confinement to modify the local optical density of states. This results in a greater fraction of spontaneous emission being guided into the lasing mode, resulting in low threshold lasing achieved in both BN-PFO and BSBCz microcavities.

5.1 Introduction

Organic semiconductor lasing has been realised in a variety of resonator architectures, with some of the lowest thresholds being reported from DFB gratings, including a claims for direct and indirect electrical operation [1, 2]. However, the complexity in the fabrication of grating resonators remains a problem for organic light-emitting diode OLED integration. Optical microcavities are an attractive type of optical resonator used to reduce lasing thresholds [3]. Additionally, they readily allow the integration of conventional OLEDs, allowing charge to be injected into the semiconductor gain medium [4]. Optical microcavities are typically made of two highly reflective mirrors placed on either side of a gain medium (as detailed in Chapter 2). Such highly reflective mirrors can be made from reflective metals, however, distributed Bragg Reflectors (DBR) are often used as they can be designed to have a reflectivity above 99%, allowing very low lasing thresholds to be demonstrated [3]. Fine control over cavity mode wavelength can also be achieved through control of the thickness of the cavity. By having the microcavity optical path length on the order of half the lasing wavelength, it is possible to generate single mode confinement which increases the emission of spontaneously emitted photons into a single lasing mode which reduces the lasing threshold [5]. The first polymer microcavity laser was reported in 1996 using poly(*p*–phenylenevinylene) (PPV) as the gain medium, with a DBR bottom mirror and silver top mirror [6]. Follow-on studies now generally use DBRs as both top and bottom mirrors to improve the lasing performance [7].

Although DFB gratings offer impressive low lasing thresholds in optically pumped systems, their structure makes it challenging to implement electrical contacts for charge injection. A planar resonator design is a promising solution to solve this by favouring a stacked layer construction. In this chapter, two state-of-the-art organic semiconductor materials, a copolymer BN-PFO (12.7%) and small molecule BSBCz (which both have reported low threshold and quasi-CW lasing) [8-11] are studied in a DBR-DBR planar microcavity structure. Such structures provide strong confinement and result in low lasing thresholds and offer better light-out coupling than grating structures. The performance of the materials is compared, and we find the BSBCz lasing threshold to be an order of magnitude lower than the BN-PFO microcavity. Finally, we compare the performances of both materials in OLEDs to determine which material has the most potential in an electrically pumped device.

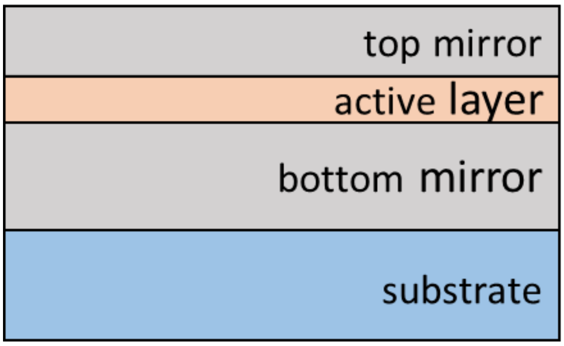

Figure 5.1: Basic planar microcavity structure made from four layers: a supporting transparent substrate, a bottom mirror, active layer and top mirror.

5.2 Design of Microcavity

The basic design of a planar microcavity can be broken into three components: the bottom mirror, the active layer, and the top mirror as shown in Figure 5.1. The active layer is typically a light-emitting material, such as an organic semiconductor. The mirrors that are placed on either side are able to confine light inside the cavity, as they are made of highly reflective metal or a stack of alternating dielectric layers. Such distributed Bragg reflectors (DBRs) are more reflective and have lower absorption than that of a metal. The thickness of the active layer (d_{cav}) determines the wavelengths supported by the microcavity using the following relation:

$$d_{cav} = \frac{m\lambda_0}{2n_{cav}} \tag{5.1}$$

Here n_{cav} is the refractive index of the active layer, λ_0 is the wavelength of the cavity mode, and m is the cavity order, which can take any integer value (1, 2, 3, ...). The length of the cavity is controlled by the thickness of the active layer, which in this work this is defined by the thickness of the organic semiconductor. As a result of this, the cavity length can be easily controlled by adjusting the speed of the spin coater, or for evaporated small molecules, the deposition time. For single-mode confinement, such films are usually around 100 nm thick. Careful control over deposition conditions is therefore required.

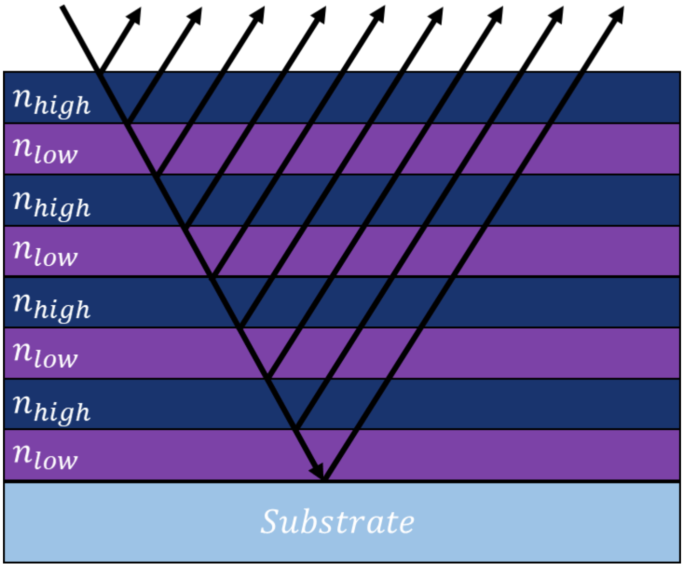

Figure 5.2: Illustration of a DBR mirror comprised of alternating high and low refractive index layers. The black arrows show the incident light reflected and transmitted thorugh the stack.

5.2.1 DBR Design

To generate lasing, it is necessary to fabricate mirrors with high reflectivity to minimise losses associated with absorption and transmission. This will help confine light in the active region and therefore promote simulated emission. For this reason, DBR mirrors (see Figure 5.2) are commonly used in microcavity lasers. The interface at each alternating high and low refractive index layer reflects light, and the spacing between the layers is designed to reflect light so that there is constructive interference. As DBR mirrors have many interfaces that reflect light, the transmitted light from the whole stack is extremely low, and total reflectivity approaches 100%. The thickness of each alternating layer (d_{mirror}) in a DBR mirror is given by:

$$d_{mirror} = \frac{\lambda_0}{4n_{mirror}} \tag{5.2}$$

Where the desired wavelength at the centre of the DBR stop-band is λ_0. DBRs are made by repeating alternating layers on higher and lower refractive index materials (often referred to as pairs). The thickness of each layer is dependent on its refractive index. It is this difference in the refractive index that creates the reflectivity stopband that is centred at λ_0. The reflectivity at the centre of the stopband is given by:

$$R_{DBR} = \left(\frac{1 - \frac{n_o}{n_i}\left(\frac{n_{low}}{n_{high}}\right)^{2N}}{1 + \frac{n_o}{n_i}\left(\frac{n_{low}}{n_{high}}\right)^{2N}} \right)^2 \tag{5.3}$$

Here n_o, n_i, are the index of refraction at incidence and transmission. n_{low} and n_{high} are the refractive index of the lowest and highest refractive index dielectric. N is the number of pairs in the DBR mirror. From this equation, we find that higher reflectivity is achieved when a DBR is made from layers with a larger refractive index contrast. The width of the stopband ($\Delta\lambda$) is also determined by the contrast in the refractive index and is given by:

$$\Delta\lambda = \frac{4\lambda_0}{\pi} \sin^{-1}\left(\frac{n_{high} - n_{low}}{n_{high} + n_{low}}\right) \tag{5.4}$$

where n_{low} and n_{high} are the respective refractive index of the two dielectric layers, and λ_0 is the centre wavelength of the DBR. It is clear that for a DBR mirror to have high reflectivity it must have the highest index contrast with multiple pairs. The reflectivity of such DBR mirrors surpasses 97% reflectivity and allows DBR-DBR microcavities to achieve very high Q-factors. Figure 5.3a illustrates how each of the variables changes the total reflectivity of a DBR mirror using a TMM model [12]. The centre wavelength of the stopband is controlled by the thickness of each of the dielectric layers and Figure 5.3b demonstrates that the centre wavelength of a mirror is shifted when just the relative thickness of the layers is changed. Figure 5.3c indicates the effect of changing the refractive index contrast between the two

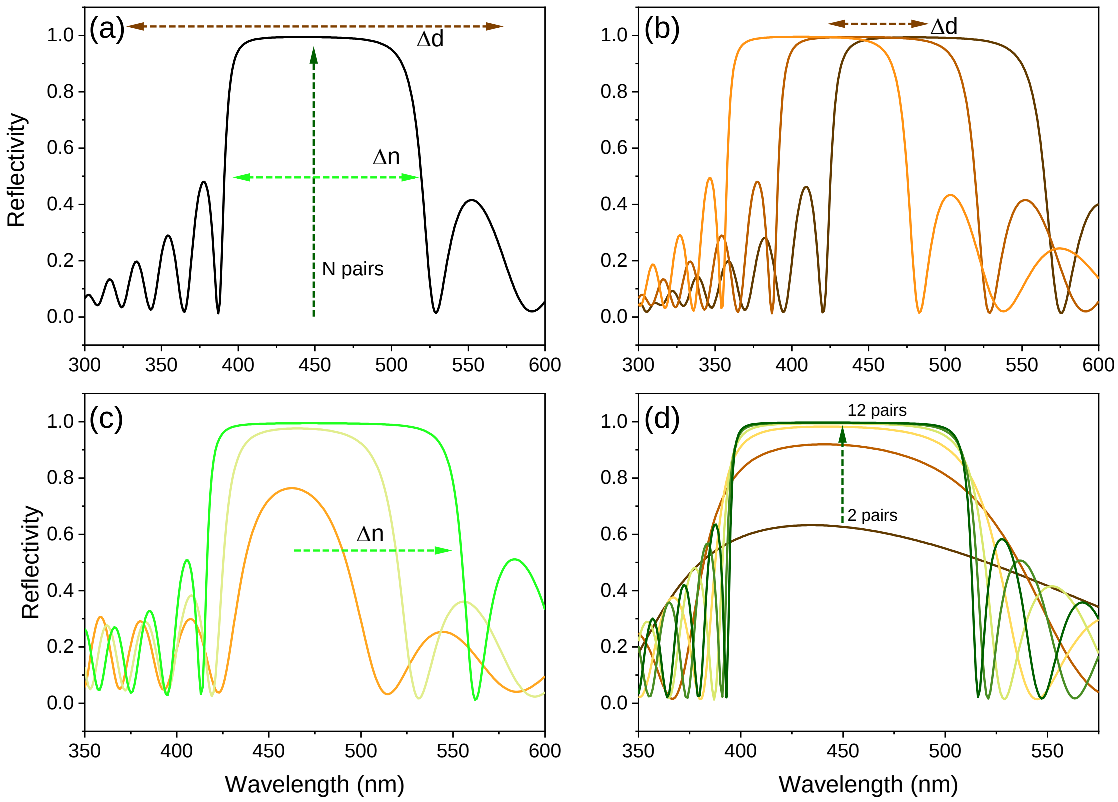

Figure 5.3: Normal incidence reflectivity spectra showing: (a) the effect of changing the number of pairs (dark green), index contrast (light green) and layer thickness (brown) (b) stopband shift due to changing dielectric layer thickness (c) stopband width dependence on the index contrast (d) stopband reflectivity dependence on the number of pairs.

high and low index dielectric layers on its reflectivity. It can be seen that as the difference between the refractive index increases, the width of the stopband of the DBR mirror increases. Figure 5.3d shows that increasing the number of interfaces/pairs (N) from 2 to 12 increases reflectivity across the stop-band.

In this work, the dielectric materials used to fabricate the DBR mirrors were TiO_2 and SiO_2. This combination has been frequently used in microcavities, as both materials can be deposited using evaporation techniques. As shown in Figure 5.4 there is a large contrast between their refractive indices.

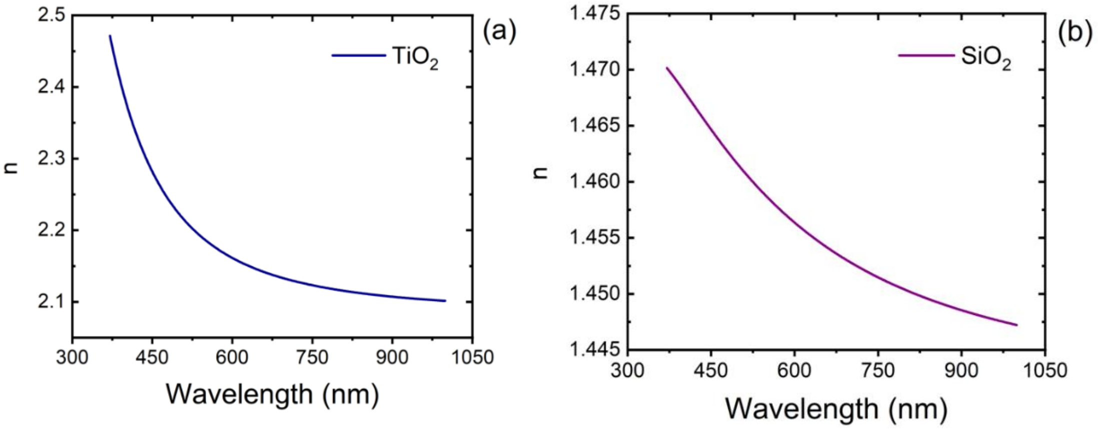

Figure 5.4: Refractive index as a function of wavelength measured using ellipsometry for 100 nm films deposited using electron-beam deposition of (a) TiO_2 (b) SiO_2.

5.2.2 BN-PFO Planar DBR-DBR Microcavity Design and Fabrication

One of the only polymers that has been reported to show quasi-CW lasing is the copolymer BN-PFO, and it is for this reason that the material is of great interest for lasing. Quasi-CW operation alongside low threshold lasing for BN-PFO has been demonstrated in a multitude of different grating architectures [11, 13, 14], with the lowest being reported in a circular grating [15]; however, the work discussed here is the first time that this material has been placed within a microcavity. In the previous chapter, BN-PFO with a BN content percentage of 12.7% was found to have the lowest ASE threshold of all BN-PFO copolymers studied (19 μJ cm^{-2}), and therefore this material was chosen for implementation into a planar microcavity.

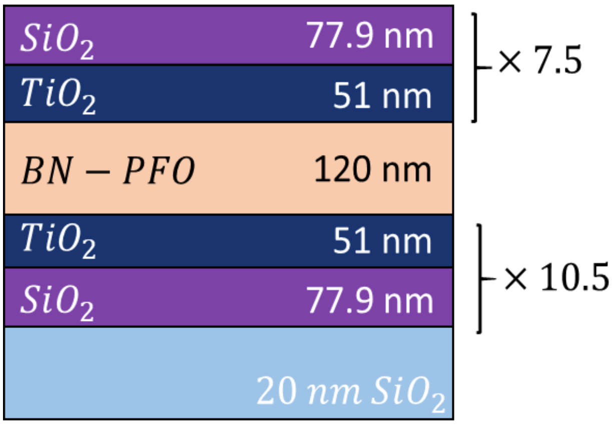

Figure 5.5: Schematic of the full planar microcavity with BN-PFO as the active layer (120 nm), where the DBR mirrors were made from alternating layers of SiO_2 (77.9 nm) and TiO_2 (51 nm). The bottom and top DBR mirrors were comprised of 10.5 and 7.5 pairs.

The planar microcavies designed for this study used highly reflective DBR mirrors, where the BN-PFO active layer thickness determines the wavelength of the modes that are supported by the cavity. In order to optimise the design of the microcavity, numerical simulations were first used to model its structure. The structure of microcavity explored (illustrated in Figure 5.5) was modelled using Transfer Matrix Method (TMM) with the optical constants (measured using ellipsometry) included for TiO_2, SiO_2 and BN-PFO. The wavelength-dependent values of BN-PFO (12.7%) measured using ellipsometry and are shown in Figure 5.6a. ASE measurements indicated that amplification should be maximized around 450 nm, and thus the cavity was designed around this wavelength. A TMM model was first used to design the DBRs. Here, the TiO_2 and SiO_2 layers had thickness of 51 nm and 77.9 nm respectively with the bottom DBR mirror consisted of 10.5 pairs and the top 7.5 pairs. The predicted cavity reflectivity shown in Figure 5.6b was used to adjust the cavity length so that single mode confinement coincided with the peak of maximum gain as observed in the ASE measurements. The TMM model suggested that a total cavity thickness of 120 nm was needed to place the cavity mode at 450 nm. The linewidth of the cavity reflectivity was used to calculate the cavity Q-factor by measuring the full width half maximum (FWHM) of the cavity mode. Q-factor is defined as $Q = \lambda/\Delta\lambda$, where λ is the

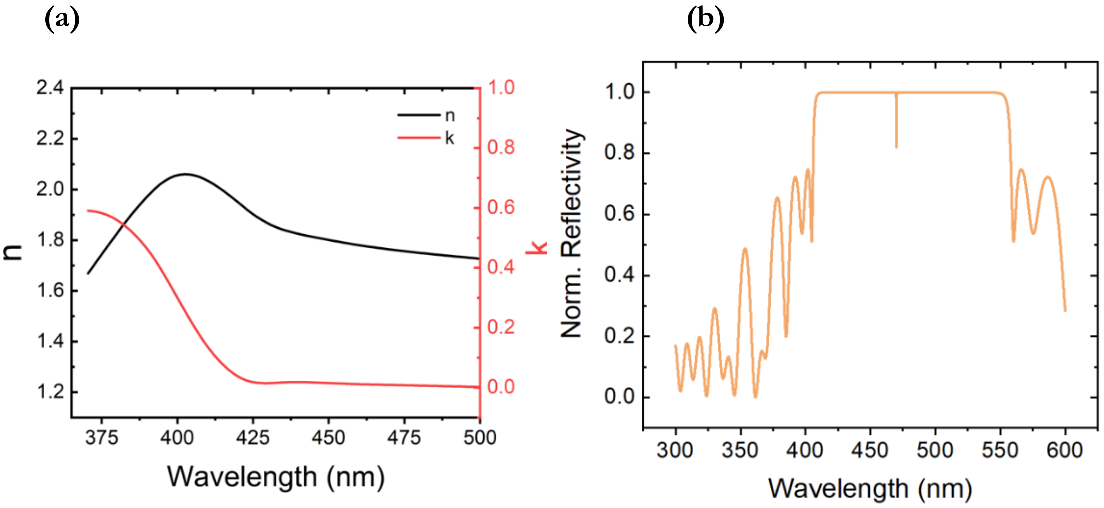

Figure 5.6: (a) BN-PFO 12.7% optical constants measured with ellipsometry (b) Simulated reflectivity for the total BN-PFO microcavity using TMM.

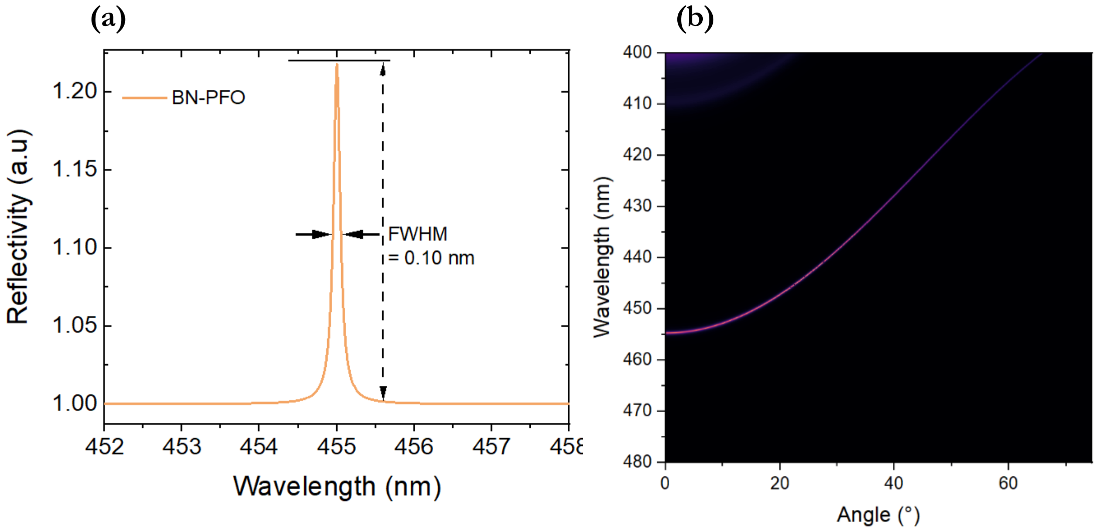

Figure 5.7: (a) Spectra from simulated BN-PFO microcavity reflectivity simulated with TMM. Using the FWHM from this the a simulated value for the Q-factor can be calculated (b) Simulated BN-PFO cavity dispersion using TMM.

centre wavelength, and Δλ is its FWHM. The model suggested a Q-factor of 4550 at a wavelength of 455 nm with a linewidth of 0.1 nm.

The simulated reflectivity at normal incidence is illustrated in Figure 5.7a, where the cavity mode can be seen centred at 455 nm. Figure 5.7b shows the simulated microcavity reflectivity as a function of angle. The wavelength range of this plot covers the stop band of the DBR mirrors with the dark regions corresponding to 99% reflectivity. The light-coloured parabolic curve is the dispersion of the cavity mode as a function of angle.

The fabrication routine of the BN-PFO (12.7%) cavities is illustrated in Figure 5.8. First, substrates were cleaned, with the cleaning process detailed in Chapter 3. A bottom DBR was

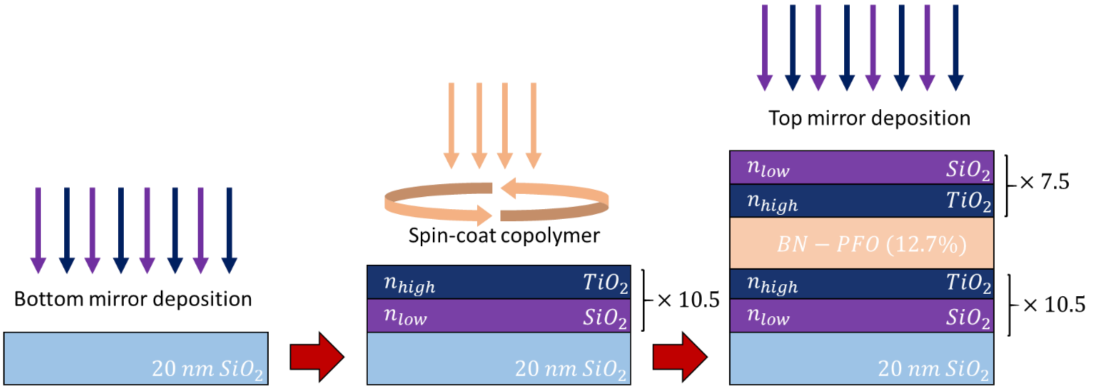

Figure 5.8: Fabrication process for BN-PFO planar microcavity starting with the deposition of the bottom 10.5 pair DBR mirror, followed by spin coating the BN-PFO, and finally depositing the 7.5 pair DBR mirror.

then grown (see Chapter 3) onto the substrate, consisting of 10.5 pairs of alternating TiO_2/ SiO_2 quarter-wave layers having a thickness of 51 nm and 77.8 nm. This resulted in a mirror having a stopband at 455 nm, with TiO_2 as the final layer. As the refractive index of TiO_2 is greater than SiO_2, the final TiO_2 layer results in a larger contrast in refractive index to the organic layer; an effect that increases optical confinement. The samples were then spin-coated with a solution of BN-PFO (12.7%) in toluene as the active layer. This solution was made by dissolving BN-PFO in toluene at a concentration of 35 mg/mL on a hot plate for 1 hour at a temperature of 65 °C in ambient conditions. Solutions were spin-cast at 3000 rpm, creating a film with a thickness of approximately 120 nm. After spin coating the BN-PFO, a top DBR composed of 7.5 TiO_2/ SiO_2 layers was deposited onto the BN-PFO, with TiO_2 being the first layer. In all cases, deposition rates for TiO_2 and SiO_2 were 2 $Ås^{-1}$ at a vacuum chamber base pressure of 4×10^{-6} mBar.

5.2.3 BSBCz Planar DBR-DBR Microcavity Design and Fabrication

The small molecule BSBCz has been reported to have one of the lowest lasing thresholds for an organic semiconductor (0.09 μJ cm^{-2}) [16] and in the previous chapter, it was shown to have a low ASE threshold of 13.8 μJ cm^{-2}. This material has also demonstrated quasi-CW lasing [8] and has the first reported material undergoing electrical pumped lasing in a Bragg grating architecture [1]. This makes it one of the most promising lasing materials to create

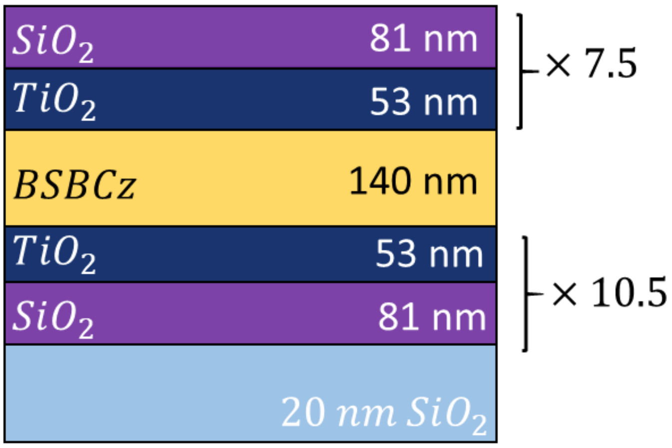

Figure 5.9: Schematic of the full BSBCz planar microcavity, where the mirrors are made from alternating layers of SiO_2 and TiO_2.

the highly sought-after directly driven organic laser diode. This material has been previously studied in a variety of resonators, including in a microcavity with a guest-host active layer [3]. The demonstration of electrically pumped lasing using a pure film of BSBCz as the active layer suggests this to be a promising composition and is therefore adopted here. Thus, studying the neat film in a planar microcavity offers more insight into potential OLED integration. The design of the BSBCz planar microcavity is illustrated in Figure 5.9 and follows the same optimisation used for the BN-PFO microcavities.

BSBCz planar microcavities were designed using the same method discussed in the previous section. This structure used 10.5/7.5 pairs of alternating SiO_2/TiO_2 for the bottom and top DBR mirrors, with TiO_2 placed next to the active layer. The thickness of the TiO_2 and SiO_2 layers were 52 nm and 81.1 nm, creating a stop band that coincided with the ASE wavelength of BSBCz which is approximately at 486 nm. Using the known refractive index of BSBCz at 486 nm (Figure 5.10a, $n = 2$), the cavity length was adjusted to generate single mode confinement around this wavelength. The cavity length was set to 140 nm provide single mode confinement at the lasing wavelength. Figure 5.10b shows the calculated cavity reflectivity where the dip in the centre of the stop band corresponds to the cavity mode.

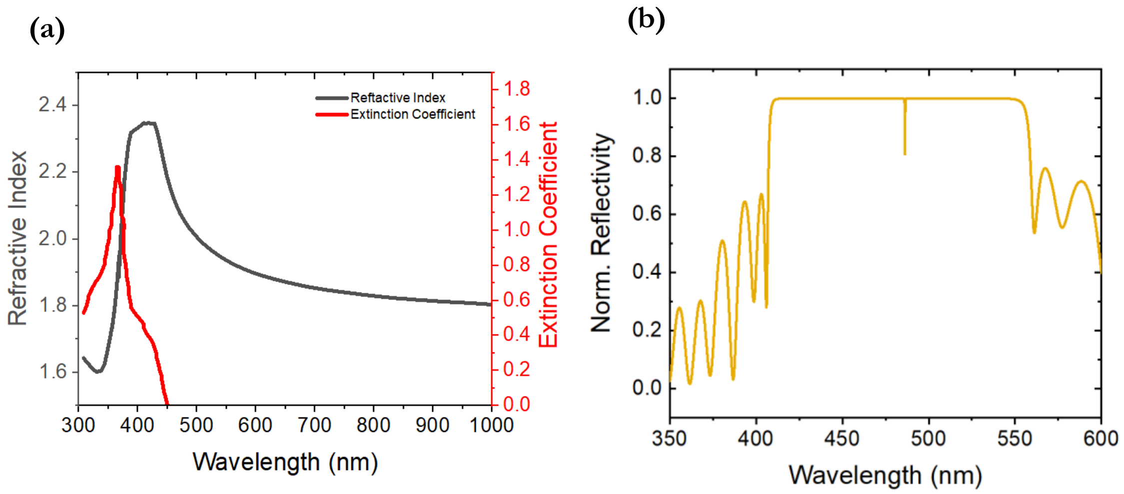

Figure 5.10: (a) BSBCz optical constants measured with ellipsometry (b) Simulated TMM reflectivity BSBCz microcavity.

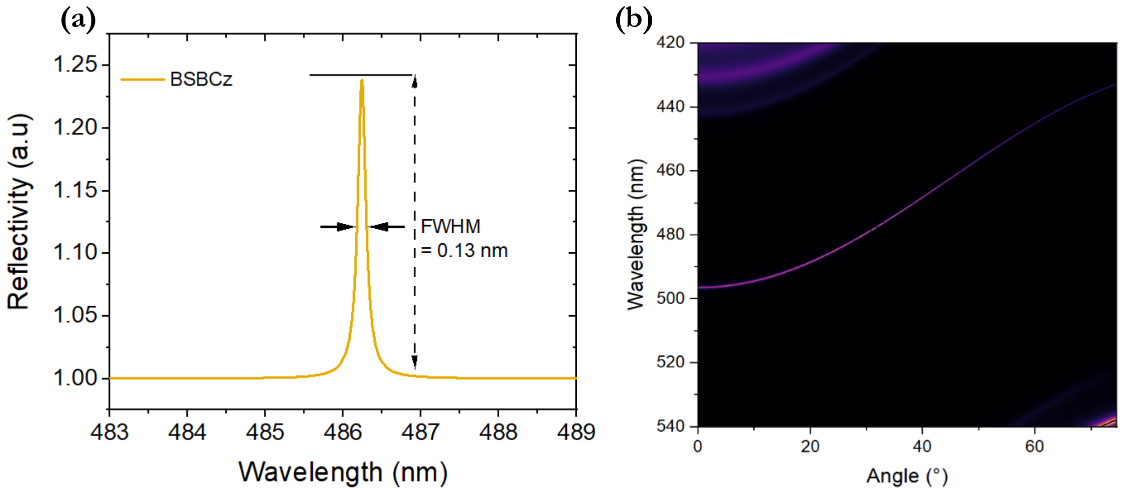

Figure 5.11: (a) TMM BSBCz cavity reflectivity used to simulate the Q-factor (b) Simulated BSBCz cavity dispersion using TMM.

Using the calculated FWHM of the cavity mode (shown in Figure 5.11a), we estimate a Q-factor of 3739. This apparent reduction in Q-factor compared to the BN-PFO microcavity results from a decrease in reflectivity at the cavity mode wavelength from 82% to 80%.

We can model the reflectivity as a function of angle as shown; this has a parabolic dispersion as can be seen in Figure 5.11b. As the wavelength range for this plot spans the stop band of the DBR, the majority of light is 99% reflected (represented by dark regions). At the angle of incidence, there is single mode confinement at the lasing wavelength.

The process to fabricate the cavity again follows that used to create the BN-PFO microcavity as shown in Figure 5.12. Here however, the BSBCz active layer was deposited by thermal evaporation using an Angstrom thermal evaporator at a rate of 1-2 Ås^{-1}, giving a final film

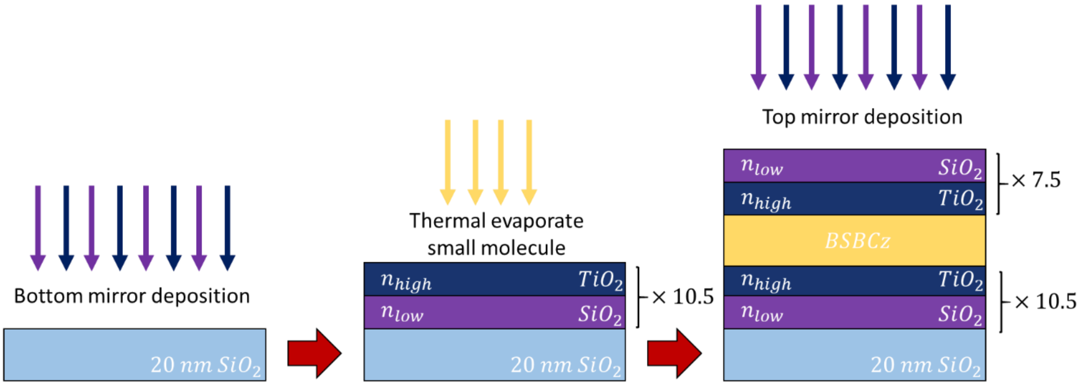

Figure 5.12: Schematic illustrating the fabrication process for BSBCz planar microcavity.

thickness of approximately 140 nm. The start base pressure for the deposition was 2.6 × 10^{-7} mBar and the crucible was heated using a Radak source.

5.3 Results and Discussion

5.3.1 BN-PFO Planar Microcavity

Before characterisation, the surface of the microcavity was cleaned using a nitrogen gun to remove any particulates. All samples were stored and measured in ambient conditions. To investigate the lasing characteristics of the planar microcavities, a Q-switched 355 nm Nd:YAG laser (100Hz, 350 ps) was focused to a spot area of 8.18 × 10^3 μm^2 on the cavity surface. The laser spot size was measured with a Thorlabs, Inc. beam profiler at the focal point and this capture is shown in Figure 5.13. This area was used to calculate the energy density of the pump laser. This calculation also accounted for the pump energy lost via absorption and reflection from the bottom DBR and substrate. This was accounted for by calculating the percentage loss by using a power meter to measure the incident and reflected laser power from a bottom DBR sample. At an incident power of 2 μW, it was found that the reflected power loss was 0.4 μW and the transmission power loss was 0.9 μW. Therefore,

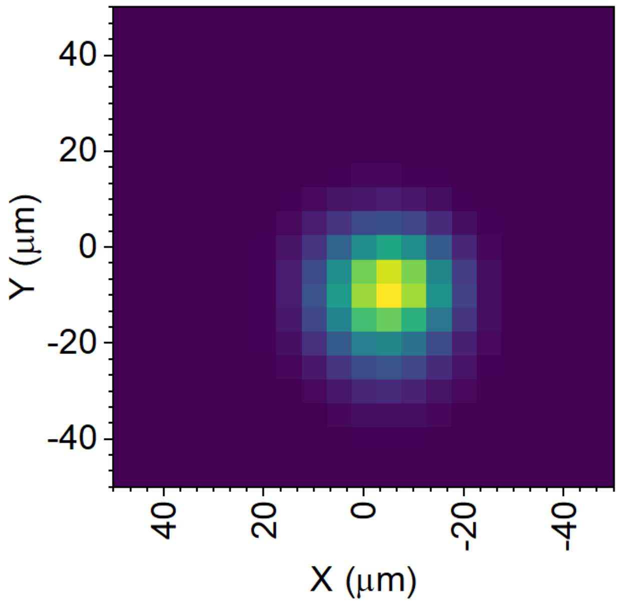

Figure 5.13: 355 nm Nd:YAG laser beam profile image taken with a Thorlabs, Inc. beam profiler.

the pump power lost to reflectivity and transmission is assumed to be 20% and 45%, with only 35% of the pump power absorbed within the cavity active layer.

Characterisation of the BN-PFO microcavity lasing performance was performed using the k-space setup detailed in Chapter 3. Here samples were positioned on an x-y-z axis stage and moved in (z) into the focus of the objective using the white light imaging path of the setup. The x-y stage adjustments allowed of the sample surface to be inspected to find a region free of particulates. For measurements, the beam splitter in front of the charge-coupled device (CCD) camera was removed from the path using a flip mount.

After the sample alignment was complete, it was then excited using a 355 nm Nd:YAG (100Hz, 350 ps) laser. The emission from the microcavity was collected in transmission through the top DBR. A UV filter was placed before the objective to remove the laser signal and prevent damage to the collection optics. The spectrometer CCD used a 1800 mm^{-1} grating with a slit set to 50 μm. Images were captured with an exposure time of 5 s. Dispersion images were captured over a range of pump fluence (3 – 19 μJ cm^{-2}) to analyse the input-output characteristics of the microcavity emission. The pump fluence was changed using a neutral density wheel that was placed in front of the laser. Excitation fluence was

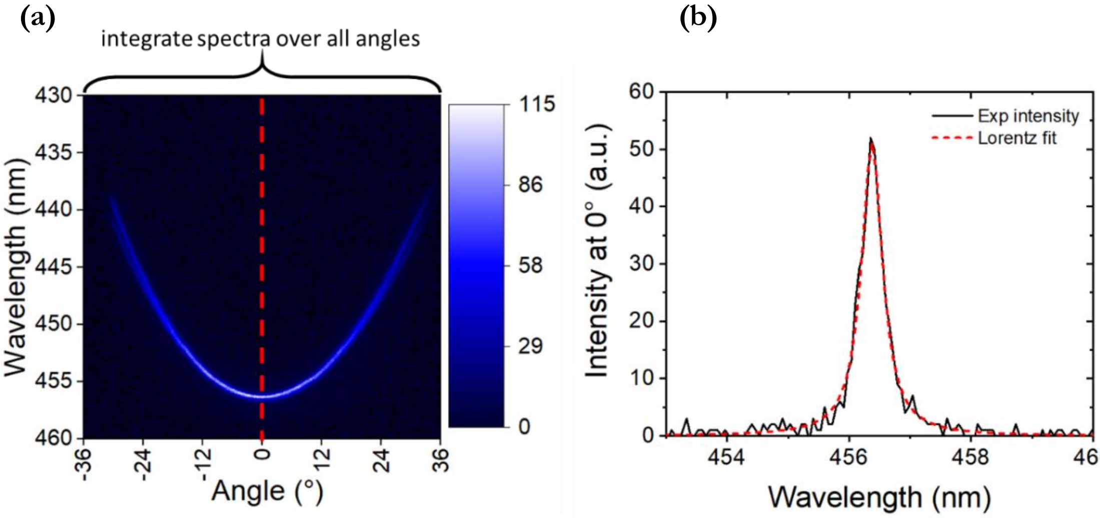

Figure 5.14: (a) Dispersion capture using k-space setup showing how the spectra was extracted over all angles to measure the threshold and linewidth at 0°. The pixel value shows the total counts. (b) Slice of the spectra emitted at 0° (black) and the Lorentz fit (red) to measure the linewidth.

measured with a power meter connected to a flip mount placed before the sample. A typical dispersion is shown in Figure 5.14a; here emission is below the lasing threshold.

To extract the input-output characteristics from the dispersion images, the total intensity over all angles for each fluence was integrated and the spectra at normal incidence was fitted with a Lorentzian function to find its full-width half maximum (FWHM). This is illustrated in Figure 5.14a where the red dashed line at 0° in the dispersion image corresponds to the point at which the spectra in Figure 5.14b was defined. This is then used to measure the linewidth of the emission below threshold which is used to provide an approximation of cavity Q-factor. Here the Q-factor of the BN-PFO planar cavity is estimated to be 1271 using $Q = \lambda/\Delta\lambda$. Compared to the TMM model (4550), the measured Q-factor is much lower as there are additional optical losses associated with the fabricated cavity. Simulations do not take into account factors such as the surface roughness of the cavity mirrors or active layer, and therefore the additional scattering from a rough surface will reduce the Q-factor of the cavity.

As the pump fluence was increased, a clear collapse of the angular emission into a forward cone is observed. This is shown in Figure 5.15 where there the emission at a fluence of 3.4 μJ cm^{-2} and 8.6 μJ cm^{-2} is plotted. Here the angular emission collapses to 0° due to the high density of states at this angle, stimulating the amplification of photons with the same

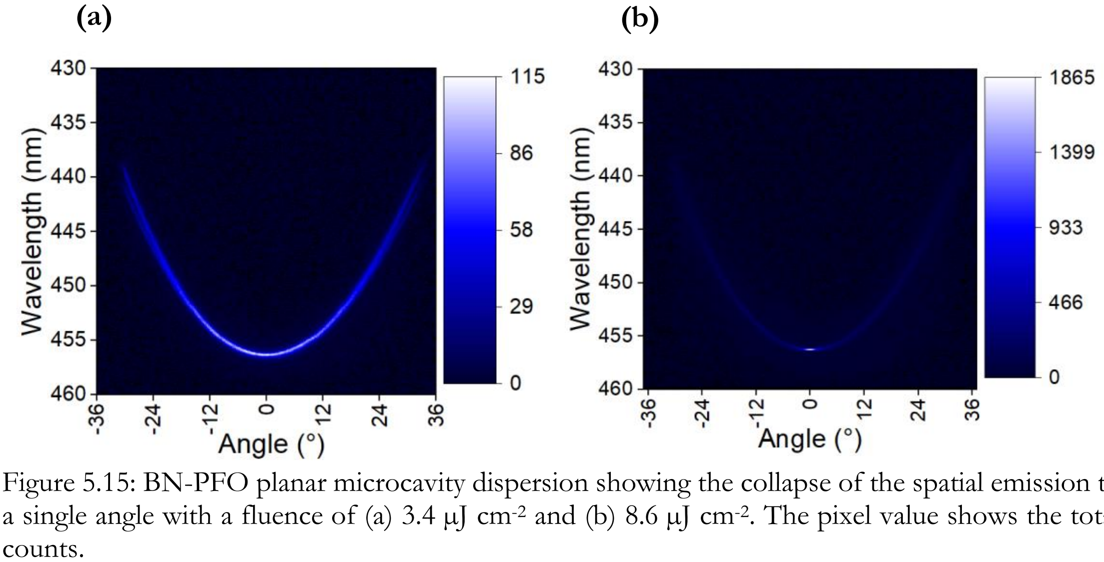

Figure 5.15: BN-PFO planar microcavity dispersion showing the collapse of the spatial emission to a single angle with a fluence of (a) 3.4 μJ cm^{-2} and (b) 8.6 μJ cm^{-2}. The pixel value shows the total counts.

momentum and energy. As spontaneous emission still takes place and escapes the cavity, the random directionality of this is observed in the faint dispersion curve still visible in Figure 5.15b. This fluence dependent spatial collapse is evidence of stimulated emission becoming the dominant emission process.

Using the method detailed in Figure 5.14, the input-output characteristic extracted from the dispersion captures is displayed in Figure 5.16a. As the pump fluence is increased, the integrated intensity dramatically increases at a threshold of (12 ±1.2) μJ cm^{-2}. This is evidence of lasing behaviour as the dominant process of emission changes from spontaneous to stimulated. To determine the threshold, the spontaneous and stimulated emission regimes were fitted with separate linear fits, with the threshold defined at their intercept. We find that the threshold is half that of other reported polymer microcavities [6, 17, 18].

As the planar cavities were designed for single mode confinement, the number of optical modes that are available for BN-PFO to emit into are reduced relative to vacuum. This has the effect of funnelling more of the spontaneous emission into the lasing mode. As more light is now available to promote simulated emission, it results in a reduced lasing threshold. One of the typical characteristics of lasing is the emission having a narrow linewidth (< 1 nm) [19]. However, for microcavities the high Q-factor and single mode confinement results in narrow emission linewidths (< 0.5 nm) even below threshold, as shown in Figure 5.16a.

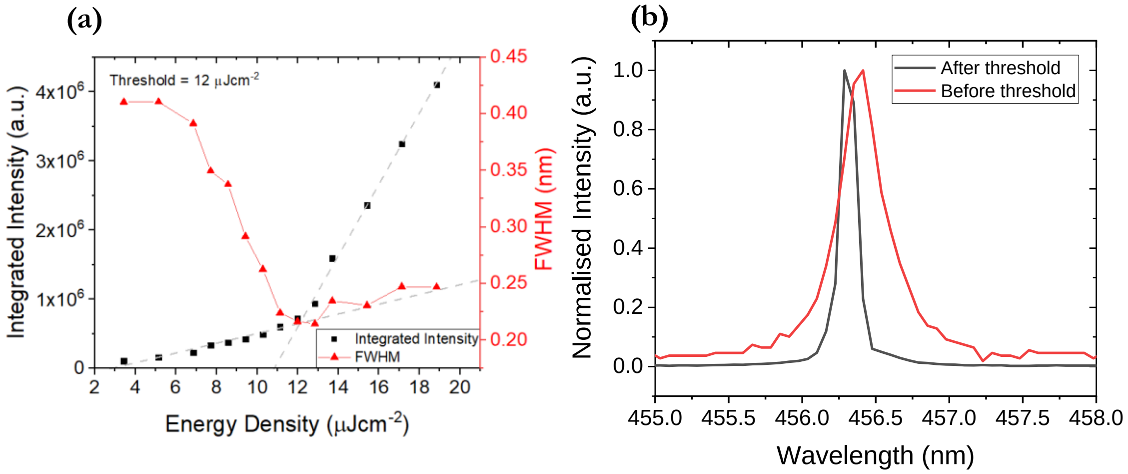

Figure 5.16: (a) Input-output characteristics for BN-PFO microcavity: integrated intensity (black), FWHM (red) (b) Spectral linewidths of emissions.

The sudden narrowing in the spectral linewidth that coincides with the increase in output intensity is evidence for lasing. As shown in Figure 5.16b we see a blue shift in the peak of the lasing emission as the pump fluence was increased. This can be attributed to both reversible and irreversible photobleaching caused the pump laser that reduces the refractive index of the active material.

As the lasing characteristics for a BN-PFO microcavity have not been reported so far we can only compare the threshold measured with other microcavity polymer lasers. We find that the threshold of 12 μJ cm^{-2} to be one of the lowest reported thresholds for a planar polymer microcavity (1120, 84, 20 μJ cm^{-2}) [6, 7, 18].

5.3.2 BSBCz Planar Microcavity

Lasing measurements on BSBCz microcavities were conducted using the same k-space setup that was discussed in the previous section. Both BN-PFO and BSBCz have strong absorption in the UV, therefore, the BSBCz microcavities were also excited with using a 355 nm Nd:YAG (100Hz, 350 ps) laser. Here dispersion captures were taken over a pump fluence range of 0.09 - 1.9 μJ cm^{-2}. Figure 5.17a shows an example dispersion curve below threshold; here the wavelength of the cavity mode at normal incidence was 494 nm. Again, emission spectra at 0° (blue dashed line) was fitted using a Lorentz function to estimate the FWHM.

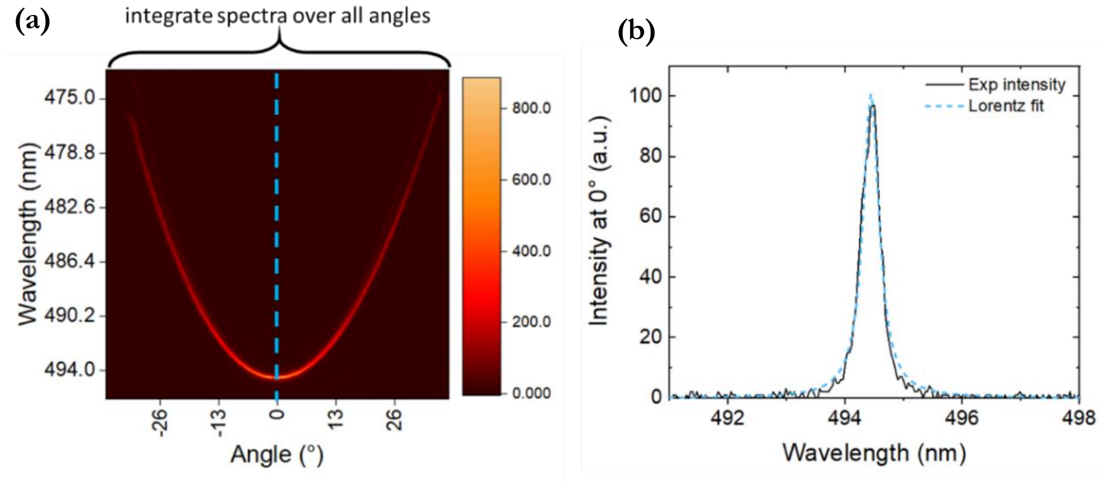

Figure 5.17: (a) Illustration showing how the spectra was extracted to measure the threshold and linewidth at 0° The pixel value shows the total counts. (b) Lorentz fit of the emission at 0°.

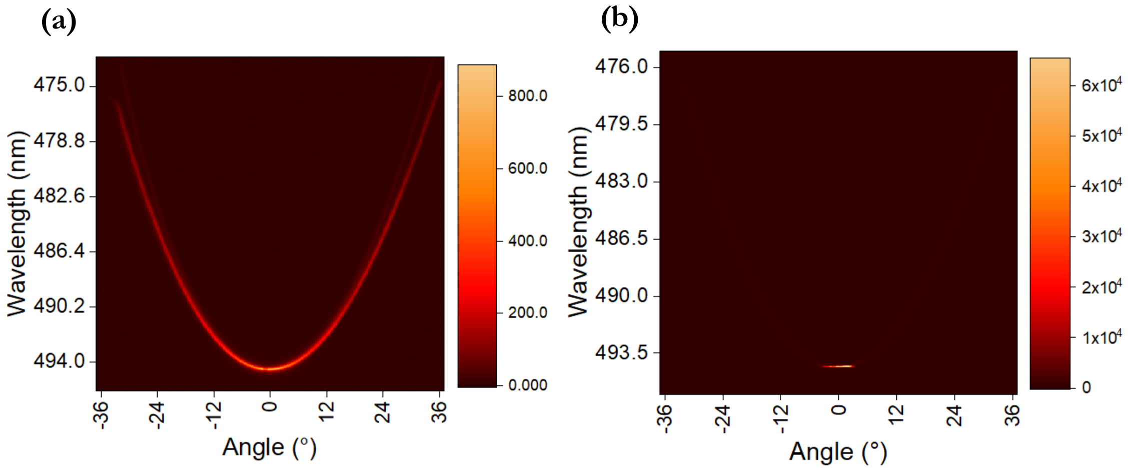

Figure 5.18: BSBCz planar microcavity dispersion (a) before threshold (b) after threshold. The pixel value shows the total counts.

This fitting is shown in Figure 5.17b where the FWHM was determined as 0.35 nm at a wavelength of 494 nm at normal incidence, corresponding to a Q-factor of 1411. This is also significantly lower than the Q-factor (3800) calculated using TMM simulation. When compared to microcavities that also use BSBCz as an active layer, their reported Q-factors are higher with values >2000, but use a longer cavity length of 600 nm [3]. This is a common way to increase the Q-factor of a cavity, as increasing the length of the cavity increases the photon cavity lifetime.

The spatial collapse in the dispersion curve was also observed for the BSBCz microcavities as the pump fluence was increased. This is shown in Figure 5.18, where dispersion curve below and above threshold at pump energy densities of 1.1 μJ cm^{-2} and 1.7 μJ cm^{-2} are shown. Again, Figure 5.18a shows the typical dispersion curve expected for a spontaneous emission from a planar microcavity. Figure 5.18b shows the spectral collapse to normal incidence with increasing pump intensity. This again suggests that the lasing condition has been met.

Using the method detailed in Figure 5.17, the input-output characteristics were extracted from each dispersion capture. The integrated intensity and the FWHM of the emission as a function of pump fluence is plotted in Figure 5.19a. As the pump fluence was increased, there is a sudden change in the output intensity, indicating that the emission is now dominated by stimulated emission. Taking separate liner fits of the two regimes the intercept

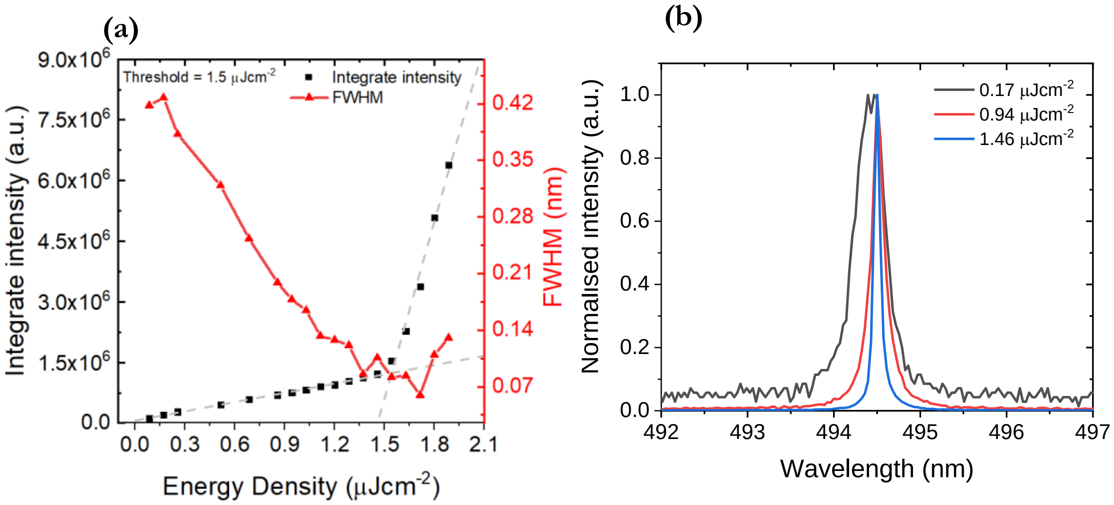

Figure 5.19: (a) Input-output characteristics for BSBCz microcavity: integrated intensity (black), FWHM (red) (b) Spectral linewidths of emissions.

gives a threshold of (1.5 ±0.15) µJ cm^{-2}. This is 8 times lower than the BN-PFO (12.7%) cavity. The narrowing of the emission linewidth is also seen at threshold, as shown in Figure 5.19a where the FWHM reduces from 0.42 nm to <0.20 nm. This is shown in Figure 5.19b where the linewidths at 0.17, 0.94 and 1.46 µJ cm^{-2} are plotted. Here the spectra are normalised and undergo narrowing around at 494.4 nm. Unlike the BN-PFO microcavities, there is no observed blue shift caused by increasing the pump fluence. Compared to the BN-PFO, BSBCz excitation used a pump fluence that was an order of magnitude lower, therefore, the extent of the reversible and irreversible photobleaching effects attributed to the refractive index change was not observed.

The threshold measured in this study is very similar to that reported in the literature (1.5 µJ cm^{-2}) where the active region was comprised from blend of BSBCz and CBP, with the top DBR deposited by thermal evaporation (TeO_x/LiF) [3].

5.4 BN-PFO and BSBCz Planar Microcavity Comparison

If we compare the lasing performance of both materials, a clear difference is seen, as BSBCz has a much lower threshold of 1.5 μJ cm^{-2} compared to BN-PFO 12 μJ cm^{-2}. This is consistant with the results from Chapter 4 where BSBCz had a lower ASE threshold of 13.8 μJ cm^{-2}, compared to 19 μJ cm^{-2} of BN-PFO (12.7%). The lower lasing threshold of BSBCz is therefore to be expected, however the difference between the lasing thresholds is one order of magnitude. This suggests that BSBCz has properties that are more favourable for lasing in a microcavity. This might be attributed to the optical properties of the material or from the physical quality of the film resulting from its deposition by thermal evaporation.

The optical properties of the materials are shown in Table 5.1. Interestingly BSBCz and BN-PFO have PLQYs of 89% and 93.6% respectively. PLQY measurements were carried out using the setup detailed in Chapter 3. BSBCz is reported to have a PLQY of 99% when kept in an inert atmosphere [20]. In this study, PLQY measurements were recorded under ambient conditions. The fact that BSBCz is measured having a PLQY less than that of BN-PFO suggests that BSBCz is more susceptible to degradation under ambient conditions.

The radiative decay lifetimes for each material were measured using a TCSPC experimental setup as detailed in Chapter 3. The measured lifetimes for BSBCz and BN-PFO (12.7%) are 0.219 ns and 0.251 ns respectively. Organic laser materials with reduced radiative decay lifetimes have been reported to correlate strongly with reduced lasing threshold [21].

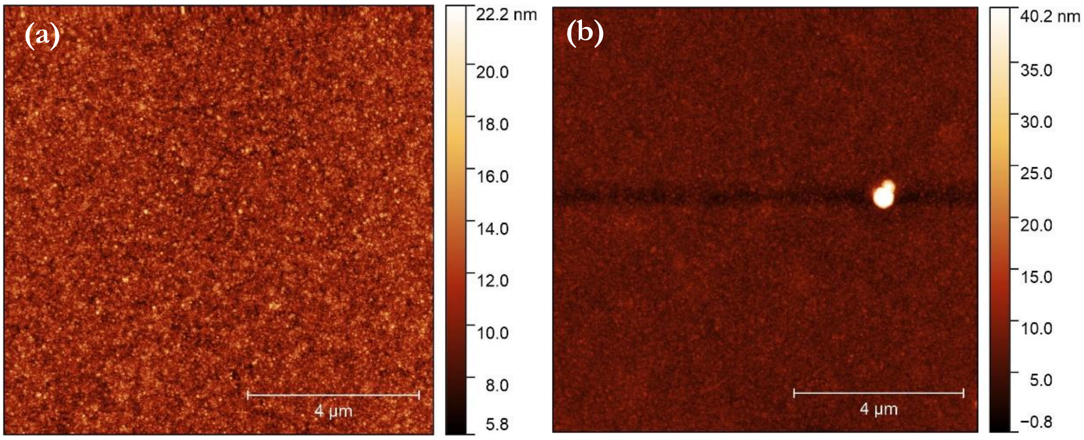

Figure 5.20: AFM scan of a) BSBCz microcavity b) BN-PFO (12.7%) microcavity.

Table 5.1: Planar microcavity lasing comparison for BN-PFO and BSBCz

Material	Lasing wavelength (nm)	E_{th} (µJ cm^{-2})	PLQY (%)	Q-factor	τ (ns)	E_{th} literature-grating (µJ cm^{-2})	E_{th} literature-planar microcavity (µJ cm^{-2})
BN-PFO (12.7%)	445	12	93.6	1271	0.251	1.2 [15]	-
BSBCz	494	1.5	89	1411	0.219	0.09 [16]	1.5 [3]

The Q-factors of each cavity is a measure of the lifetime of photons trapped inside the cavity. Longer cavity photon lifetimes enhance the probability for interaction with excited singlet states and stimulate emission. Therefore, increased photon confinement can reduce the threshold required to reach a population inversion. We suspect that the difference between the Q-factors of the BSBCz and BN-PFO microcavities may cause a reduction in the lasing threshold. One factor that will influence the Q-factor of the cavity is the surface quality of active layer between the DBR mirrors. As BN-PFO was spin-coated, this technique can cause increased surface roughness. AFM scans measuring the top of completed BN-PFO and BSBCz cavities are illustrated in Figure 5.20: AFM scan of a) BSBCz microcavity b) BN-PFO (12.7%) microcavity. Here the root mean square (RMS) roughness for BN-PFO and BSBCz cavities are 2.6 nm and 1.5 nm respectively. This increase in surface roughness at the interface between the active layer and the top DBR mirror may result in an increase in the losses associated with scattering. As more photons will be scattered and removed from the cavity mode, the average photon cavity lifetime is reduced, leading to a reduced Q-factor.

5.4.1 Organic Light Emitting Diode Characterisation

One of the most attractive features of planar microcavities is their simplistic integration with an OLED structure. Consequently, two OLEDs were fabricated with BN-PFO and BSBCz to compare their electrical operation. The layers and corresponding thicknesses deposited in each device are illustrated in Figure 5.21. The current density and luminance for the BSBCz OLED are orders of magnitude higher that the BN-PFO OLED (displayed in Figure 5.22). The electroluminescence from BN-PFO (shown in Figure 5.23) includes additional emission in the green that is not present in the normal PL. This can be attributed to the formation of excimers. Therefore, less light can be efficiently generated at the lasing wavelength. This suggests that further study into electrical operation of planar microcavities should concentrate on devices containing BSBCz.

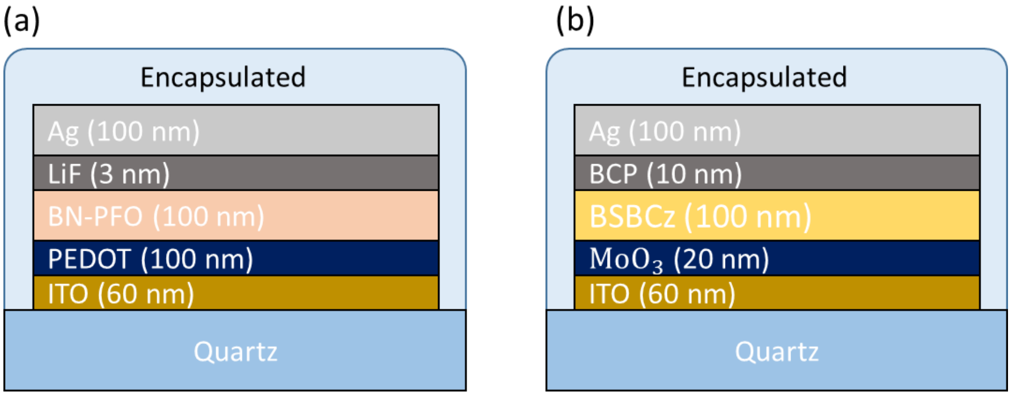

Figure 5.21: OLED device structure for (a) BN-PFO 12.7% and (b) BSBCz

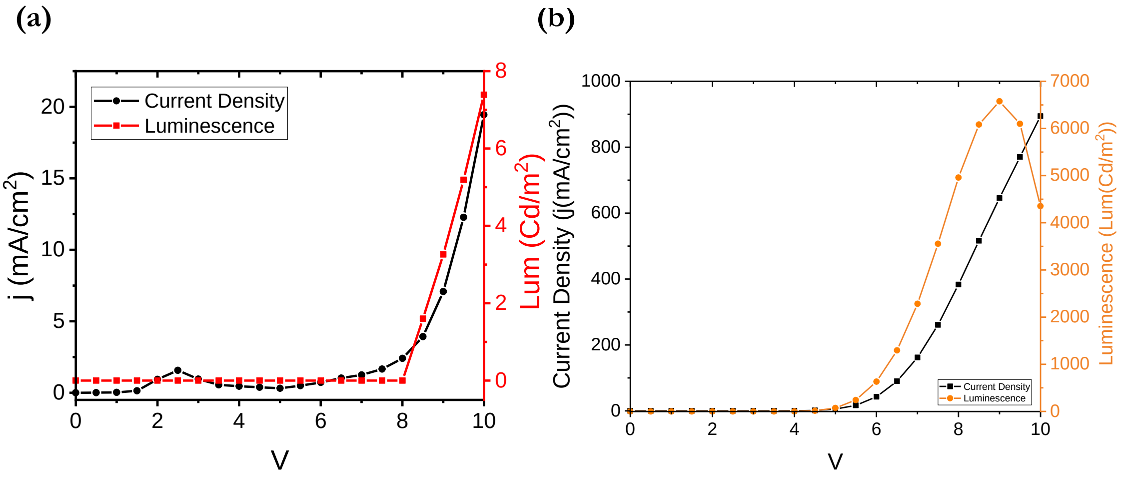

Figure 5.22: OLED current density and luminescence as a function of voltage for a) BN-PFO b) BSBCz

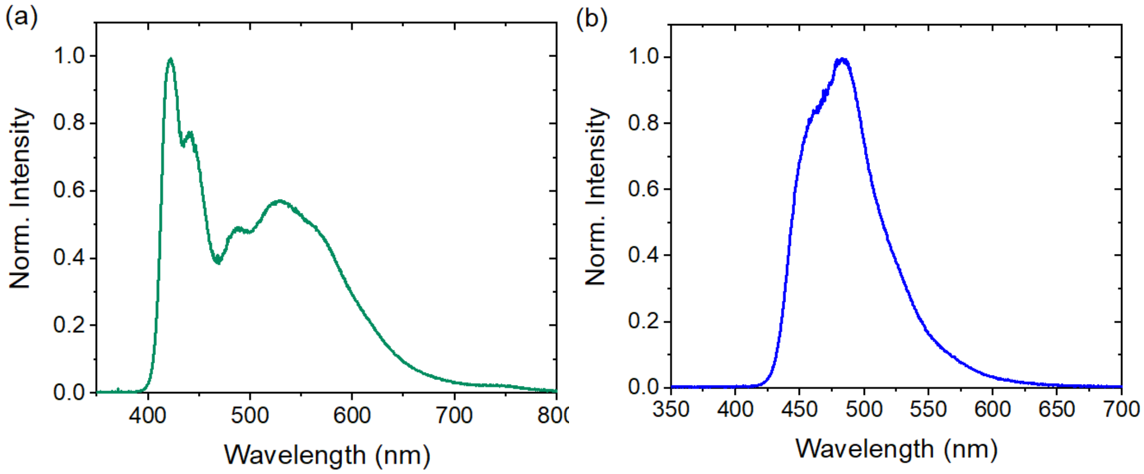

Figure 5.23: Electroluminescence measurements for (a) BN-PFO 12.7% and (b) BSBCz OLEDs.

5.5 Summary

In this chapter, the two organic compounds, BN-PFO 12.7% and BSBCz were explored and integrated into a planar microcavity. DBR mirrors were designed so that the stop band was centred at the lasing wavelength, with the cavity length supporting single mode confinement. Numerical simulation suggested Q-factors of 4550 and 3800 for BN-PFO and BSBCz. Organic microcavity lasers were then fabricated using e-beam deposition to grow the DBR mirror. Spin coating and thermal evaporation was used to deposit BN-PFO and BSBCz. Low lasing thresholds of 12 μJcm^{-2} and 1.5 μJcm^{-2} were measured from both microcavities with Q-factors of 1271 and 1411 determined. Although both materials undergo low threshold lasing, the BSBCz microcavity had 8 times reduction in lasing threshold. This difference in threshold was attributed to the higher Q-factor of the BSBCz cavity, which we suspect is caused by the surface roughness of the BN-PFO being larger.

5.6 References

[1] A. S. D. Sandanayaka et al., “Indication of current-injection lasing from an organic semiconductor,” Appl. Phys. Express, vol. 12, no. 6, p. 061010, Jun. 2019, doi: 10.7567/1882-0786/ab1b90.

[2] K. Yoshida, J. Gong, A. L. Kanibolotsky, P. J. Skabara, G. A. Turnbull, and I. D. W. Samuel, “Electrically driven organic laser using integrated OLED pumping,” Nat. 2023 6217980, vol. 621, no. 7980, pp. 746–752, Sep. 2023, doi: 10.1038/s41586-023-06488-5.

[3] Y. Hu, F. Bencheikh, S. Chénais, S. Forget, X. Liu, and C. Adachi, “High performance planar microcavity organic semiconductor lasers based on thermally evaporated top distributed Bragg reflector,” Appl. Phys. Lett., vol. 117, no. 15, p. 153301, Oct. 2020, doi: 10.1063/5.0016052.

[4] Y. Hu, J. Lin, L. Song, Q. Lu, W. Zhu, and X. Liu, “Vertical Microcavity Organic Light-emitting Field-effect Transistors,” Sci. Rep., vol. 6, no. 1, p. 23210, Mar. 2016, doi: 10.1038/srep23210.

[5] F. P. L. Alexey V. Kavokin, Jeremy J. Baumberg, Guillaume Malpuech, Microcavities, Second Edi. Oxford Science Publications, 2017.

[6] G. J. D. & R. H. F. N. Tessler, “Lasing from conjugated polymer microcavities,” Nature, vol. 382, no. August, pp. 695–697, 1996.

[7] L. Persano et al., “Monolithic polymer microcavity lasers with on-top evaporated dielectric mirrors,” Appl. Phys. Lett., vol. 88, no. 12, p. 121110, Mar. 2006, doi: 10.1063/1.2179611.

[8] A. S. D. Sandanayaka et al., “Toward continuous-wave operation of organic semiconductor lasers,” Sci. Adv., vol. 3, no. 4, pp. 1–8, 2017, doi: 10.1126/sciadv.1602570.

[9] A. S. D. Sandanayaka et al., “Improvement of the quasi-continuous-wave lasing properties in organic semiconductor lasers using oxygen as triplet quencher,” Appl. Phys. Lett., vol. 108, no. 22, p. 223301, May 2016, doi: 10.1063/1.4952970.

[10] T. Rabe et al., “Quasi-continuous-wave operation of an organic thin-film distributed feedback laser,” Appl. Phys. Lett., vol. 89, no. 8, p. 081115, Aug. 2006, doi: 10.1063/1.2337873.

[11] M. Lehnhardt, T. Riedl, U. Scherf, T. Rabe, and W. Kowalsky, “Spectrally separated optical gain and triplet absorption: Towards continuous wave lasing in organic thin film lasers,” Org. Electron., vol. 12, no. 8, pp. 1346–1351, 2011, doi: 10.1016/j.orgel.2011.05.005.

[12] E. Hecht, Optics, Fifth Edit. Essex: Pearson Education, 2017.

[13] C. Karnutsch et al., “Low threshold blue conjugated polymer lasers with first- and second-order distributed feedback,” Appl. Phys. Lett., vol. 89, no. 20, p. 201108, Nov. 2006, doi: 10.1063/1.2390644.

[14] T. Riedl et al., “Polymer lasers: recent advances,” in Organic Light Emitting Materials and Devices XI, Sep. 2007, vol. 6655, no. November 2007, p. 66550V, doi: 10.1117/12.735896.

[15] T. Wellinger et al., “Blue-light-emitting polymer lasers with non-periodic circular Bragg resonators,” in Organic Optoelectronics and Photonics III, Apr. 2008, vol. 6999, no. April 2008, p. 699907, doi: 10.1117/12.781033.

[16] C. A. M. Senevirathne et al., “Markedly Improved Performance of Optically Pumped Organic Lasers with Two-Dimensional Distributed-Feedback Gratings,” ACS Photonics, vol. 8, no. 5, pp. 1324–1334, May 2021, doi: 10.1021/acsphotonics.0c01728.

[17] D. Moses, “High quantum efficiency luminescence from a conducting polymer in solution: A novel polymer laser dye,” Appl. Phys. Lett., vol. 60, no. 26, pp. 3215–3216, Jun. 1992, doi: 10.1063/1.106743.

[18] G. Canazza, F. Scotognella, G. Lanzani, S. De Silvestri, M. Zavelani-Rossi, and D. Comoretto, “Lasing from all-polymer microcavities,” Laser Phys. Lett., vol. 11, no. 3, p. 035804, Mar. 2014, doi: 10.1088/1612-2011/11/3/035804.

[19] I. D. W. Samuel, E. B. Namdas, and G. A. Turnbull, “How to recognize lasing,” Nat. Photonics, vol. 3, no. 10, pp. 546–549, 2009, doi: 10.1038/nphoton.2009.173.

[20] Y. Jiang et al., “Organic solid-state lasers: a materials view and future development,” Chem. Soc. Rev., vol. 49, no. 16, pp. 5885–5944, Aug. 2020, doi: 10.1039/D0CS00037J.

[21] C. Adachi and A. S. D. Sandanayaka, “The Leap from Organic Light-Emitting Diodes to Organic Semiconductor Laser Diodes,” CCS Chem., vol. 2, no. 4, pp. 1203–1216, Aug. 2020, doi: 10.31635/CCSCHEM.020.202000327.

Chapter 6: Organic Copolymer Lasing from Single Defect Microcavity Using Laser Patterning

The previous chapter explored the lasing performance of BN-PFO (12.7%) and BSBCz planar microcavities. This chapter investigates how increasing optical confinement inside a microcavity can reduce its lasing threshold. In optically pumped organic lasers, reducing the lasing threshold is a necessary component to drive the development of an organic laser diode, as this might help overcome the losses associated with electrical contacts and charge injection. Using the low lasing threshold co-polymer BN-PFO, a laser patterning technique was used to write Gaussian-shaped defects (having a diameter of ~ 2.5 μm) within a vertical microcavity. The increased lateral confinement provided by such defect provided a four-fold increase in cavity Q-Factor from 495 (planar microcavity) to 2300, resulting in the reduction in of the lasing threshold from 11 μJ cm^{-2} to 7 μJ cm^{-2}. We argue that the enhanced performance and the layered structure of the defect microcavity presents a promising architecture for an organic laser diode.

6.1 Publication

This chapter is adapted from the work on organic defect lasing published in the *Journal of Materials Chemistry C:*

Claronino, *et al.* Organic copolymer lasing from single defect microcavity fabricated using laser patterning. ***J. Mater. Chem. C***, 2023, **11**, 8204-8213.

6.2 Introduction

Reducing the laser threshold can be achieved by enhancing the Purcell factor (detailed in Chapter 2). This can be accomplished by reducing the mode volume within a microcavity; as previously demonstrated with focused ion beam (FIB) milling to create micropillars [1], or by patterning deformations that add lateral confinement [2-6]. A thermal evaporation technique using a shadow mask with a set of micron-sized rectangular openings has also been used to define such features [7]. Here, an optical patterning method, outlined in more detail in Chapter 3, was used to provide lateral confinement in a microcavity which is also capable of rapidly fabricating large arrays of defects [8]. Such lateral confinement supports additional transverse modes that can be spectrally resolved using k-space imaging.

In the previous chapters, materials that have the lowest ASE thresholds were identified and fabricated into planar microcavities. Here, planar microcavities are fabricated using a laser patterning technique to write physical 'defect' structures inside a microcavity. The emission from a single defect was characterised using a k-space imaging technique that reveals the modified optical mode structure. It was found that the defect structure generated lateral optical-confinement, enhancing the cavity Q-factor and reducing the lasing thresholds from 11 μJcm^{-2} to 7 μJcm^{-2}. This threshold is also consistent with other reports using a DFB grating with the same copolymer (BN-PFO) [9-11], (the lowest reported threshold being 1.2 μJ cm^{-2}) and is lower than thresholds reported for other polymer DBR microcavities with similar structures (84 μJ cm^{-2}) [12].

6.3 Experimental

6.3.1 Microcavity Fabrication and Design

The fundamental microcavity layer design used in the previous chapter was also used in this chapter, the main difference being that a thick PS layer was placed between the substrate and bottom DBR (see Figure 6.1a). Here the microcavity was composed of a bottom mirror made from 10.5 pairs of alternating TiO_2/SiO_2 quarter-wave layers having a thickness of 51 nm and 77.8 nm respectively, and a top mirror composed of 7.5 TiO_2/SiO_2 layers. The TiO_2 and SiO_2 layers were deposited by electron-beam evaporation at a rate of 2 Ås^{-1} in a vacuum

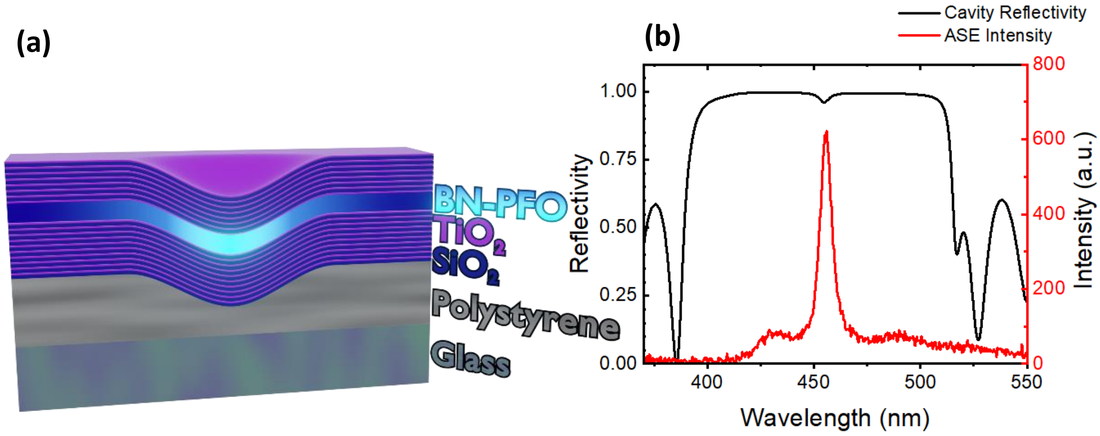

Figure 6.1: (a) Cross-section of defect microcavity structure: quartz/PS (with defect)/10.5 Pair DBR/BN-PFO (12.7 mol% binaphthyl)/7.5 pair DBR. Note that the relative depth of the defect structure is increased significantly for the sake of clarity. (b) Total simulated microcavity reflectivity (black) centred at the peak of ASE spectra (red).

chamber base pressure of 4 x 10^{-6} mBar. The thickness of each dielectric layer was calculated using the equation $\lambda_c/4n_d$, where n_d is the respective refractive index of TiO_2 and SiO_2, and λ_c is the centre wavelength of the reflectivity stop band. The cavity contained a layer of BN-PFO having a thickness of 120 nm, corresponding to $\lambda_c/2n$. The reflectivity of the cavity and ASE of BN-PFO is shown in Figure 6.1b.

6.3.2 Fabrication of Optical Defects Inside Microcavities

To engineer a physical 'defect' within the active layer of a microcavity, the planar microcavity structure was deposited on top of a micro-lattice patterned polystyrene film. The Gaussian shape of the defect patterned into the polystyrene film propagated throughout all the layers in the cavity stack and established a localised region inside the cavity in which a relative modification in the lateral refractive index provided 3D optical confinement. This is illustrated in the schematic shown in Figure 6.1a. Note that in this figure, the relative depth of the defect is enhanced for the purpose of clarity. Fabrication of defect microcavity structures were made by first sequentially cleaning substrates following the process outlined in previous chapters. Polystyrene from Sigma-Aldrich (M_w 350 kDa) was then dissolved in toluene at a concentration of 100 mg/mL by stirring on a hotplate for 24 hours at 65°C. This solution was then spin-coated on top of a quartz substrate at 3500 rpm creating a film having a thickness of 1100 nm.

After all solvent had evaporated from the PS film, the samples were then loaded into a vertical sample holder, illustrated in the laser patterning experimental setup in Chapter 3, Figure 3.4. The sample holder was mounted onto an x-y-z axis translational stage, where the z-axis was controlled by a manual linear stage, that was adjusted to move the sample into the focus of the objective using the imaging path of the setup. After alignment, the motorized x-y axis stages were homed, bringing the centre of the sample into view of the objective. Both the shutter that obstructed the laser path and the motorized stages were automated using MATLAB. Opening the shutter and exposing the PS film to the focussed, frequency-doubled Ti:sapphire (Coherent MIRA) laser caused localised melting. Overexposing the film to the laser resulted in sudden burning. Once an area had been burnt, the motorized stage was moved >30 μm in the y-direction to a new location that was unexposed. The shutter exposure time was then adjusted to induce melting rather than burning the film. It was found that the optimal exposure time was 2.3 s; this caused localised melting and an out-flow of the semi-liquid polystyrene, resulting in the creation of a Gaussian-shaped defect 'dip' having

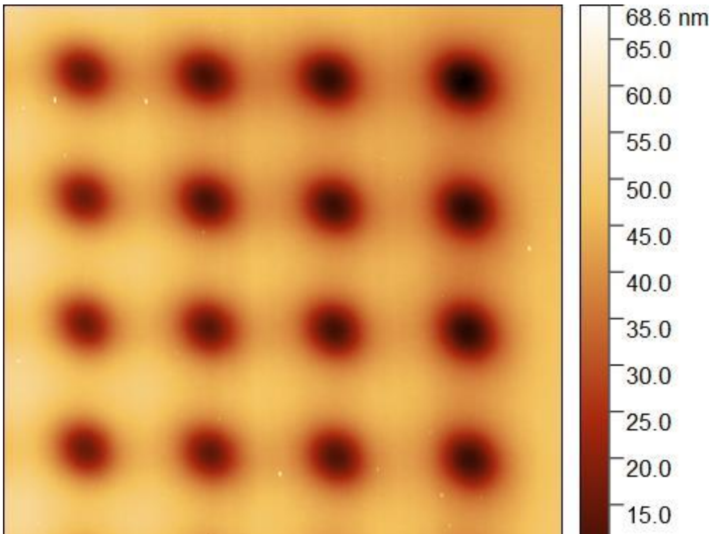

Figure 6.2: AFM scan of patterned defect lattice on PS layer

a diameter of 2.5 μm and a maximum depth of 40 nm. The sample was then displaced in the y-direction and a lattice of defects was written by moving in the x-direction. After a row of defects had been written, the sample was moved in the y-direction to write another line of defects, creating a lattice. The number of defects written in each row and column was controlled along with the spacing between them. Figure 6.2 shows an AFM scan illustrating the typical defect lattice. The main reason why lattices were written was to make finding them easier for subsequent optical characterisation measurements. Once a series of lattices were written, the sample was displaced again in the y-direction. In this final location, the shutter was intentionally opened to burn the PS film, then the sample was continuously displaced in the y-direction. This caused a line to be "burnt" from the region of the defects to the edge of the sample, allowing the defects to be easily located. On top of this, a BN-PFO (12.7%) microcavity was fabricated using the methodology described in the previous chapter. This consisted of a bottom DBR, a BN-PFO (12.7%) film and a top DBR.

6.3.3 Optical Characterisation of Microcavities

Microcavities were characterised using the k-space imaging dispersion setup detailed in Chapter 3. As was used in previous chapters, defect microcavity samples were placed onto the k-space setup sample holder which was mounted onto an x-y-z axis stage. The sample was moved into the focus of the objective by moving in the z-direction, using the white light imaging path. Once in focus, the sample was moved in an x-y plane to find the burned line connecting the defects to the edge of the sample. With the defect area located, the area was excited using a 355 nm Nd:YAG (100Hz, 350 ps) laser at low power. This allowed individual defects to be located, as they had relatively enhanced emission intensity. A spatial filter positioned at the focus of the imaging lens was used to isolate the emission from a single defect by rejecting the unwanted surrounding emission. An f = 125 mm lens then focused emission into an Andor Shamrock SR-303i-A CCD spectrometer with the grating set at 1800 mm^{-1} with an entrance slit of 50 μm, giving a spectral resolution of 0.06 nm.

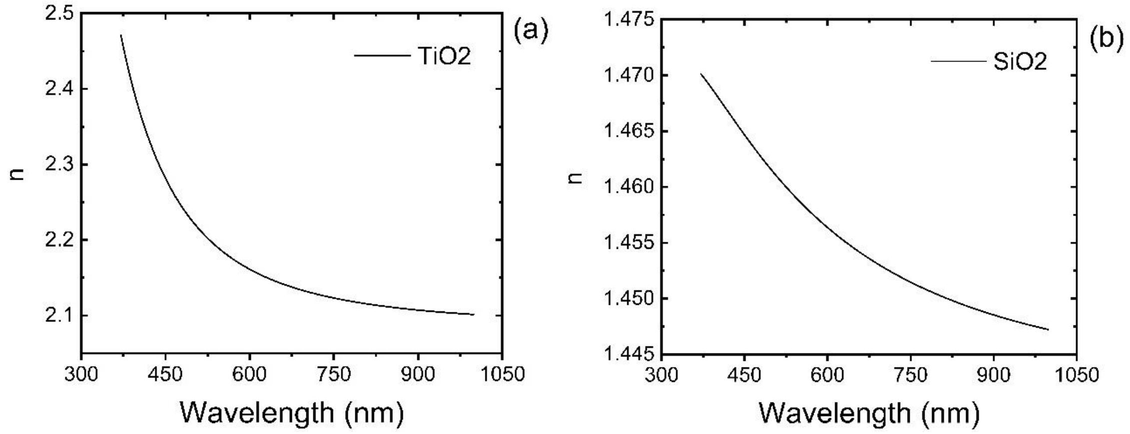

Figure 6.3: Refractive index measured using ellipsometry of (a) TiO_2 (b) SiO_2.

6.3.4 Numerical Simulations

Simulations of the defect cavity were performed in collaboration with Dr Alaina Muravitskaya at the University of Hull. Numerical simulations of the far-field projections were performed using Ansys Lumerical software, that used the Finite Difference Time Domain method. In order to create free field conditions, a perfectly matched layer was set as the boundary conditions of the simulation box, with the mesh size set to 3 nm. The refractive index of the TiO_2 and SiO_2 layers were measured using ellipsometry (see Figure 6.3) with the optical constants of the BN-PFO film shown in Figure 6.4a. The experimentally defined thicknesses of the layers were (similar to Chapter 5) used to model the structure. Specifically, TiO_2, SiO_2 and BN-PFO had thicknesses of 51, 77.8 and 120 nm respectively. The defect was modelled as a cylindrical dip through all the layers, as shown in Figure 6.4b. A dipole source was used to simulate the emission of the BN-PFO and was oriented in-plane of the structure. A top field monitor gave the intensity of the outcoupled emission and its angular distribution. The far-field projections were then averaged for different dipole orientations in-plane of the cavity.

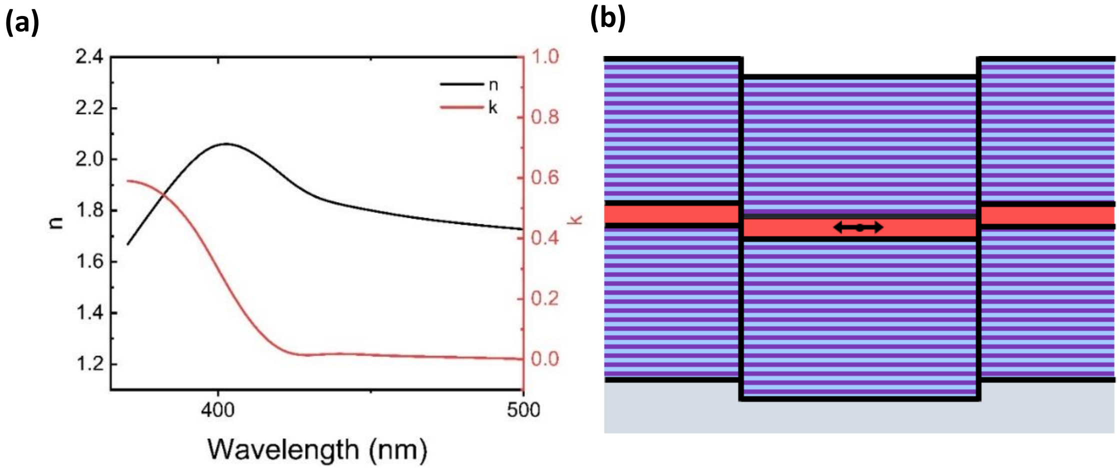

Figure 6.4: (a) Optical constants measured using ellipsometry for BN-PFO with 12.7% BN content (b) design architecture of the structure used in numerical simulations.

6.4 Experimental Results

In order to compare the optical characteristics of the defect and planar cavity, two regions of the sample were measured. As illustrated in Figure 6.5, the defect and planar region on the same sample were excited to determine whether the additional confinement from the defect could reduce the lasing threshold. Unlike the planar microcavities studied in the previous chapter, the planar region for this microcavity was considered a more accurate comparison as it incorporates a bottom PS layer. This results section is split into two parts, first characterisation of the planar PS microcavity, and secondly characterising the defect microcavity.

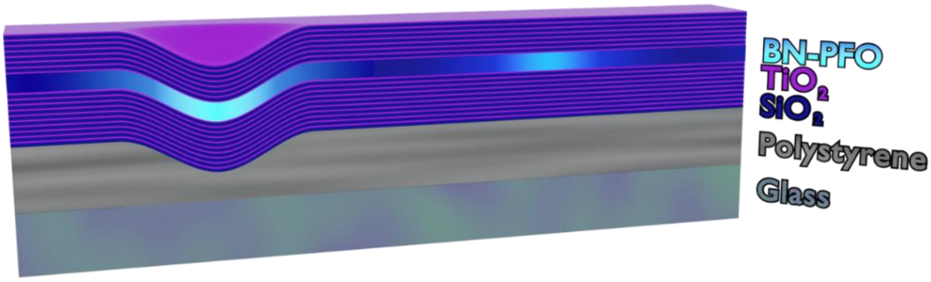

Figure 6.5: Extended defect microcavity where the planar region outside of the defect can be observed. The glowing from the active areas represents the excitation for defect and planar measurements. (defect - planar)

6.4.1 BN-PFO and PS Planar Microcavity

In the previous chapter, a BN-PFO 12.7% planar microcavity was studied. The planar structure studied here is very similar to the previous structures discussed in Chapter 5, however, there was a thick PS layer positioned beneath the microcavity. The structure of the cavities (without a defect) is shown in Figure 6.5. The cavity was pumped optically using a Q-switched 355 nm Nd:YAG (100Hz, 350 ps) laser that was focussed to a spot size with an area of 8.18×10^{-5} cm^{-2} at normal incidence. Emission through the top DBR of the cavity was collected as a function of pump fluence using the k-space imaging PL dispersion set up in a transmission configuration (see details in Chapter 3). At low pump fluence, the emission measured from the planar microcavity region at normal incidence is centred at 445 nm, with a broad angular dependence, having a close to parabolic dispersion as shown in Figure 6.6a. The FWHM was found to be 0.9 nm, corresponding to a cavity Q-factor of 494; a value comparable to other cavities having a similar structure [13].

The planar microcavity was then optically pumped at a range of excitation fluences, with PL emission at normal incidence shown in Figure 6.6b. It can be seen that as the excitation fluence is increased, a reduction in the emission linewidth is also observed. This is more clear in Figure 6.7b where emission linewidth (measured at normal incidence) is plotted as a function of pump intensity. Here a corresponding drop in linewidth is observed at a

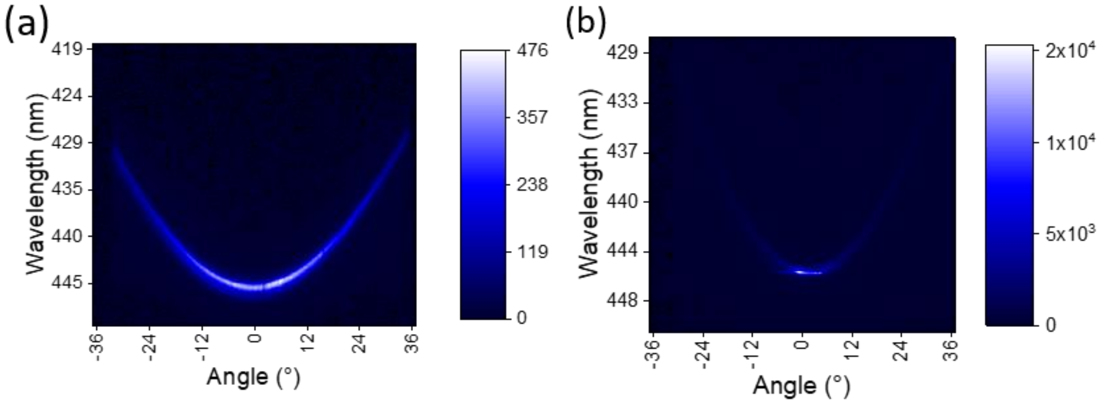

Figure 6.6: Planar microcavity k-space imaging PL dispersion (a) under threshold at 6 μJcm-2 (b) above threshold (11 μJcm-2). The pixel value shows the total counts.

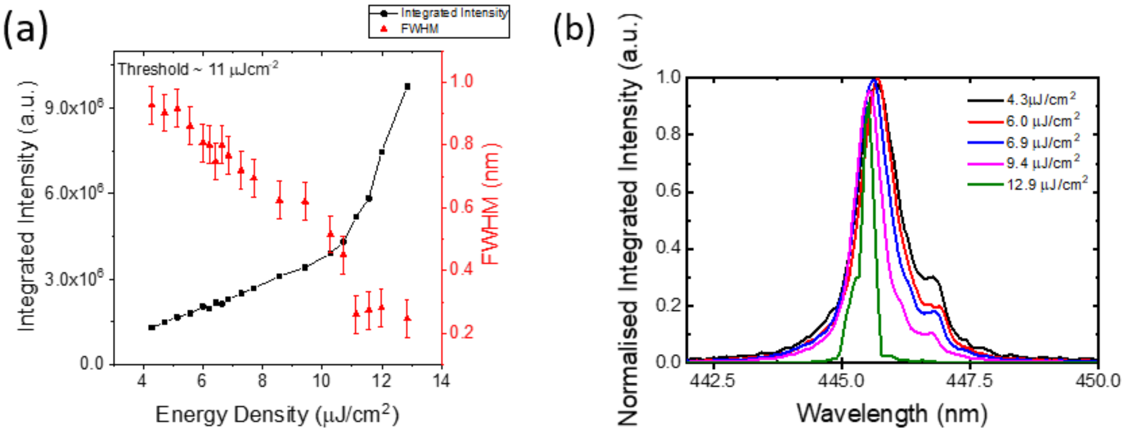

Figure 6.7: (a) Input-output characteristics for planar microcavity, where integrated intensity (left) and (b) FWHM (right) is plotted as a function of energy density.

threshold of 11 μJcm^{-2}; a result consistent with the planar microcavity threshold (12.5 μJ cm^{-2}) reported in Chapter 5. This threshold is lower than previously reported polymer microcavities (84 μJ cm^{-2} and 17 μJ cm^{-2}) [12, 14]. This reduction in linewidth and a non-linear increase in the integrated emission intensity is associated with a lasing threshold. Notably, a sudden change to a normal emission directionality above the lasing threshold is also evidenced. This can be seen in Figure 6.6b where the emission dispersion is plotted at threshold. Here it can be seen that emission is now consolidated into a narrow forward cone having an angular spread of 1.5°. This collapse in angular emission is again consistent with lasing emission.

6.4.2 BN-PFO Defect Microcavity

Here we discuss the effect of generating a localised defect in a planar microcavity on its emission and lasing properties. The structure of the defect characterised using AFM is shown in Figure 6.8. Here, measurements were taken on the patterned region of the PS layer, on a bottom DBR deposited onto the patterned PS layer and finally on the top DBR surface that completed the microcavity stack. From this, it can be clearly shown that typical defects have a near Gaussian shape, with a maximum depth of 40 nm and a diameter of approximately 2.5 μm. Here the diameter of the defects was defined by the beam-waist of the focussed patterning laser on the sample surface, with the depth being chosen to minimise thermally induced damage to the patterned PS layer. These measurements indicate that the defects propagate throughout the whole structure of the microcavity and are not planarized by the BN-PFO copolymer film. This modification to make the microcavities concave results in a relative change in lateral refractive index, effectively adding 3D confinement to a 2D microcavity in order to reduces the mode volume.

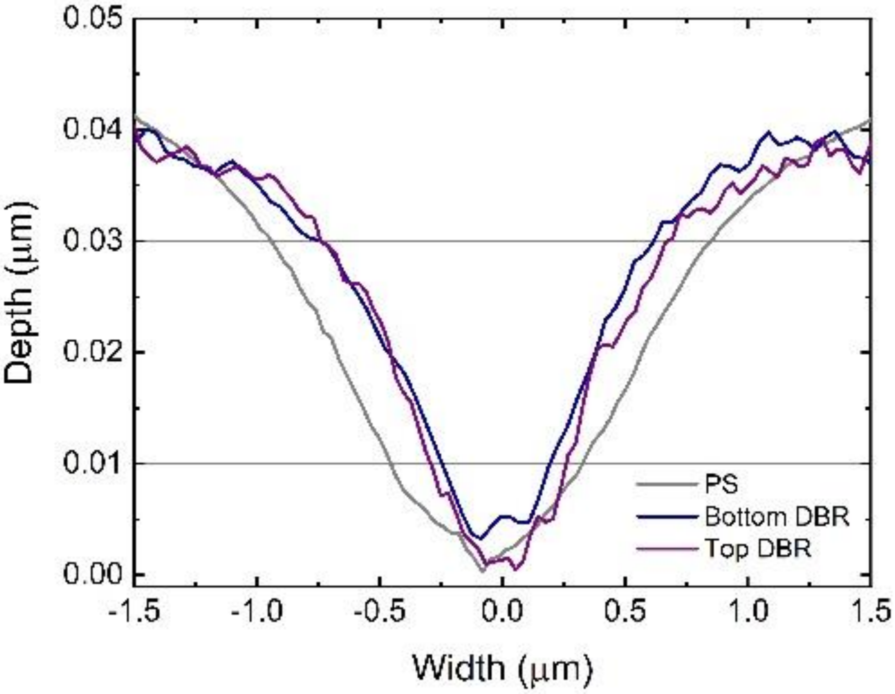

Figure 6.8: Defect profiles for the PS, bottom DBR and top DBR layers of the microcavity, measured with AFM.

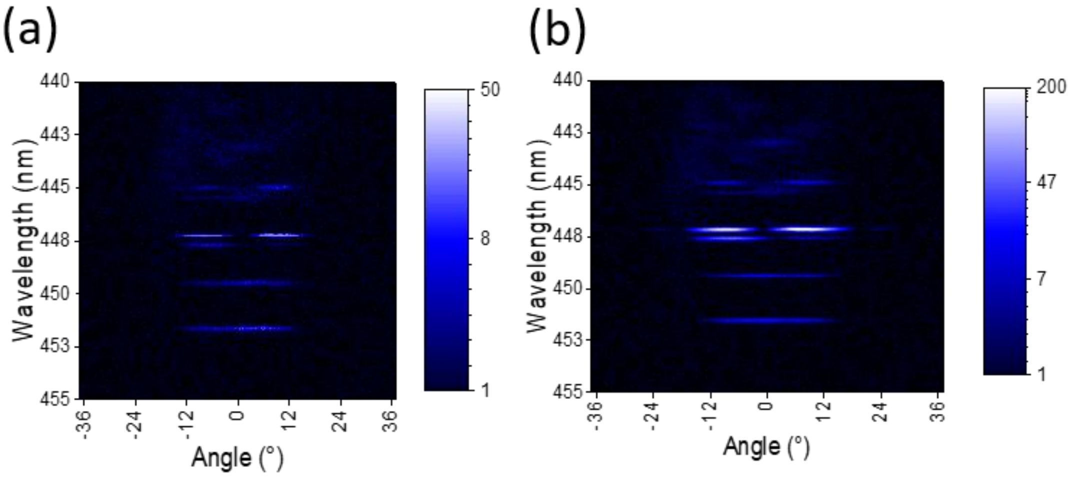

Figure 6.9: k-space image for the defect microcavity dispersion (a) under threshold (7.7 μJcm-2) (b) over threshold (12.0 μJcm-2). The pixel value shows the total counts.

Using the k-space setup detailed in Chapter 3, images of the emission dispersion below and above threshold is shown in Figure 6.9. Here it can be seen that the defect cavity supports additional modes, as the emission is quantised into a series of modes evident at 444.89, 445.37, 447.17, 447.63, 449.46, and 451.55 nm. It is observed that the modes at 444.89, 447.17, and 447.63 nm are split into two maxima which are located at angles of -8.4° and 8.4°, and therefore suggest that at this wavelength, emission is emitted into a 'ring'. Similar mode structures have also been reported for photonic dots that also effectively reduce the mode volume in a microcavity [3, 7].

To describe the structure of the selected defect modes finite-difference time-domain (FDTD) numerical simulations were used. Here a cylinder defect having a diameter of 2.5 μm and a

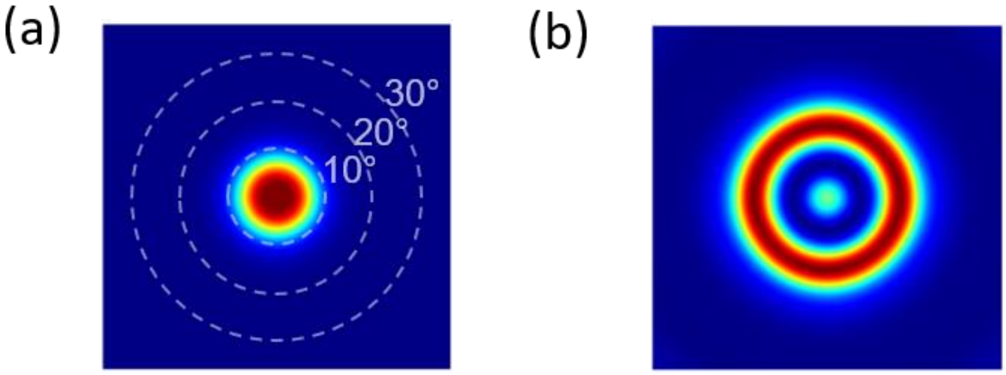

Figure 6.10: Numerical simulation of the far-field projection for cylindrical defect (a) lowest energy mode (b) lasing mode.

depth of 40 nm was used to approximate the microcavity defect (Figure 6.4). The far-field projections of the lowest energy mode and the lasing mode are plotted in Figure 6.10a and Figure 6.10b. In both the numerical and experimental measurements, the field projections for these modes have this observed circular symmetry as a result from the structure of the defect.

The FWHM of the emission of the various modes is around 0.2 nm: a value much narrower than found for the planar microcavity (0.9 nm). Interestingly, it was found that emission originating from the mode at 447.17 nm has the highest intensity. The approximated Q-factor (below threshold) for this mode is 2300, indicating that the enhanced lateral confinement from the defect increases the photon lifetime and therefore results in an increase in Q-factor. The reduced mode volume (V) and high Q-factor are expected to enhance the rate of spontaneous emission into the lasing mode to reduce the lasing threshold [15].

Figure 6.9b shows the dispersion of cavity emission at an excitation fluence of 12.0 μJcm^{-2} (above threshold in the planar microcavity). It is evident that the majority of the emission comes from the ring-like mode at 447.17 nm, with the intensity of other modes being much less. This non-linear increase corresponds with the instigation of lasing – a conclusion that is also supported by comparing the relative input-output behaviour of the different cavity modes. This is shown in Figure 6.11, where the integrated intensity of each of the different optical modes as a function of pump excitation is plotted. Significantly, the mode at 447.17 nm undergoes a large, non-linear increase in intensity with increasing pump-fluence, whilst the emission intensity from the other modes grows only linearly. This is clear evidence of a lasing process, with a threshold of 7 μJcm^{-2} identified. It is worth noting that the mode at 447.63 nm also follows a non-linear increase in emission intensity, however as the intensity

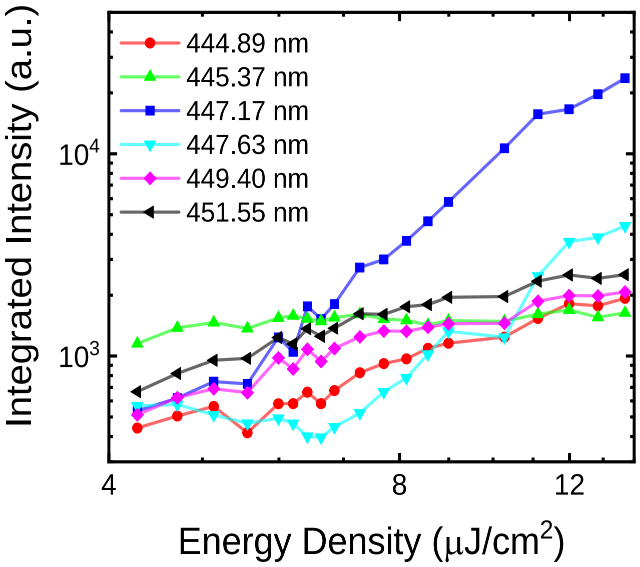

Figure 6.11: (e) Defect profile for each layer of the microcavity, measured with AFM (f) Integrated intensity extracted from the Fourier imaging dispersion as a function energy density for each emitting mode with lasing coming from 447.17 nm.

from this mode is comparable to that of the other non-lasing modes, it is therefore not characterised it as lasing. The recorded threshold of 7 μJ cm^{-2} is also comparable to other organic micro lasers that have reported thresholds of 20 μJ cm^{-2} using a thermal evaporation shadow mask technique [16], and 4.2 μJ cm^{-2} with more complex fabrication processes involving e-beam lithography and FIB [17]. To offer a wider scope for completeness, Figure 6.12 compares the thresholds measured in this study with other polymer laser architectures. It is important to note that the linewidth of the emission for the defect microcavity was below the resolution of the spectrometer both below and above threshold, and it was therefore not possible to evidence the lasing threshold from changes in the mode linewidth alone. When compared to the planar microcavity threshold (11 μJ cm^{-2}), it is found that the defect microcavity cavity gives a 40% reduction in threshold. This suggests that despite the enhanced optical confinement generated by the defect, its effect on optical gain is relatively modest. Indicating that this is due to light emission originating from a higher order mode, suggesting that coupling to higher energy modes is less efficient. This has been demonstrated in photonic dots, where higher energy modes have increased lasing thresholds [7]. As the lasing emission from our defect is not from the lowest mode, this indicates that with further optimisation the threshold for the defect cavity can be reduced.

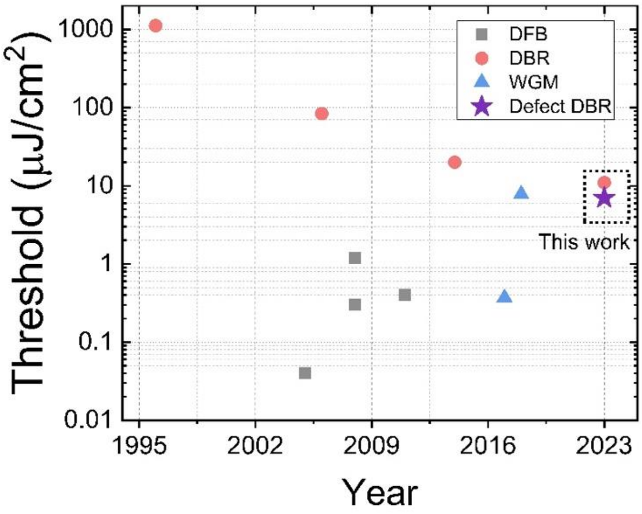

Figure 6.12: Polymer laser threshold comparison for DFB (Grey Square), DBR (red circle), WGM (Blue triangle), and defect cavity (purple star). The dashed square outline the thresholds measured in this study.

Table 6.1: Polymer laser thresholds referred to in Figure 6.12.

Resonator	**Lasing threshold (μJ/cm^2)**			
Microcavity	1120 [18]	84 [12]	20 [19]	11 (this work)
DFB	1.2 [9]	0.4 [20]	0.3 [21]	0.04 [22]
WGM	7.8 [23]	0.37 [24]		
Defect microcavity	7.0 (this work)			

6.5 Summary

In this chapter, lasing from BN-PFO is explored as an active layer for a regular planar microcavity, and a microcavity containing a 2.5 μm wide defect that provides additional localisation of confinement. It is shown that the addition of the defect structure results in enhanced optical confinement, indicated by an increase in cavity Q-factor from 494 in the planar cavity, to over 2300 in the defect cavity. Lasing was observed in both structures, however, despite the additional optical confinement, the thresholds for lasing in both types of structure were similar at 7 μJ cm^{-2} and 11 μJ cm^{-2} in the defect cavity and planar cavity respectively. The fabrication of such defect structures was achieved using an optical patterning technique that melted Gaussian shaped dimples into a PS film and has the potential to be used to write large arrays of defects. With this approach there is potential application in the fabrication of microscale laser devices for integrated photonic circuits and sensors.

6.6 References

[1] A. M. Adawi et al., “Spontaneous Emission Control in Micropillar Cavities Containing a Fluorescent Molecular Dye,” Adv. Mater., vol. 18, no. 6, pp. 742–747, Mar. 2006, doi: 10.1002/adma.200502099.

[2] R. Brückner et al., “Phase-locked coherent modes in a patterned metal–organic microcavity,” Nat. Photonics, vol. 6, no. 5, pp. 322–326, May 2012, doi: 10.1038/nphoton.2012.49.

[3] D. Urbonas, T. Stöferle, F. Scafirimuto, U. Scherf, and R. F. Mahrt, “Zero-Dimensional Organic Exciton–Polaritons in Tunable Coupled Gaussian Defect Microcavities at Room Temperature,” ACS Photonics, vol. 3, no. 9, pp. 1542–1545, Sep. 2016, doi: 10.1021/acsphotonics.6b00334.

[4] F. L. Al-Jashaam, R. Jayaprakash, D. M. Coles, A. J. Musser, K. Georgiou, and D. G. Lidzey, “Optical-Mode Structure of Micropillar Microcavities Containing a Fluorescent Conjugated Polymer,” Adv. Quantum Technol., vol. 3, no. 2, p. 1900067, Feb. 2020, doi: 10.1002/qute.201900067.

[5] F. Ding, T. Stöferle, L. Mai, A. Knoll, and R. F. Mahrt, “Vertical microcavities with high Q and strong lateral mode confinement,” Phys. Rev. B, vol. 87, no. 16, p. 161116, Apr. 2013, doi: 10.1103/PhysRevB.87.161116.

[6] L. Mai, F. Ding, T. Stöferle, A. Knoll, B. Jan Offrein, and R. F. Mahrt, “Integrated vertical microcavity using a nano-scale deformation for strong lateral confinement,” Appl. Phys. Lett., vol. 103, no. 24, p. 243305, Dec. 2013, doi: 10.1063/1.4847655.

[7] M. Langner, M. Sudzius, S. I. Hintschich, H. Fröb, V. G. Lyssenko, and K. Leo, “Sub-nanojule threshold lasing in 5×5 μm 2 organic photonic boxes,” in Organic

Optoelectronics and Photonics III, P. L. Heremans, M. Muccini, and E. A. Meulenkamp, Eds., Apr. 2008, p. 699902. doi: 10.1117/12.781158.

[8] R. Jayaprakash et al., “Two-Dimensional Organic-Exciton Polariton Lattice Fabricated Using Laser Patterning,” ACS Photonics, vol. 7, no. 8, pp. 2273–2281, Aug. 2020, doi: 10.1021/acsphotonics.0c00867.

[9] T. Wellinger et al., “Blue-light-emitting polymer lasers with non-periodic circular Bragg resonators,” in Organic Optoelectronics and Photonics III, P. L. Heremans, M. Muccini, and E. A. Meulenkamp, Eds., Apr. 2008, p. 699907. doi: 10.1117/12.781033.

[10] M. Lehnhardt, T. Riedl, U. Scherf, T. Rabe, and W. Kowalsky, “Spectrally separated optical gain and triplet absorption: Towards continuous wave lasing in organic thin film lasers,” Org. Electron., vol. 12, no. 8, pp. 1346–1351, 2011, doi: 10.1016/j.orgel.2011.05.005.

[11] C. Karnutsch et al., “Low threshold blue conjugated polymer lasers with first- and second-order distributed feedback,” Appl. Phys. Lett., vol. 89, no. 20, p. 201108, Nov. 2006, doi: 10.1063/1.2390644.

[12] L. Persano et al., “Monolithic polymer microcavity lasers with on-top evaporated dielectric mirrors,” Appl. Phys. Lett., vol. 88, no. 12, p. 121110, Mar. 2006, doi: 10.1063/1.2179611.

[13] K. E. McGhee, R. Jayaprakash, K. Georgiou, S. L. Burg, and D. G. Lidzey, “Polariton condensation in a microcavity using a highly-stable molecular dye,” J. Mater. Chem. C, vol. 10, no. 11, pp. 4187–4195, 2022, doi: 10.1039/D1TC05554B.

[14] A. Palatnik and Y. R. Tischler, “Solid-State Rhodamine 6G Microcavity Laser,” IEEE Photonics Technol. Lett., vol. 28, no. 17, pp. 1823–1826, Sep. 2016, doi: 10.1109/LPT.2016.2573200.

[15] F. P. L. Alexey V. Kavokin, Jeremy J. Baumberg, Guillaume Malpuech, Microcavities, Second Edi. Oxford Science Publications, 2017.

[16] M. Sudzius, M. Langner, S. I. Hintschich, V. G. Lyssenko, H. Fröb, and K. Leo, “Multimode laser emission from laterally confined organic microcavities,” Appl. Phys. Lett., vol. 94, no. 6, p. 061102, Feb. 2009, doi: 10.1063/1.3080689.

[17] P. B. Deotare, T. S. Mahony, and V. Bulović, “Ultracompact Low-Threshold Organic Laser,” ACS Nano, vol. 8, no. 11, pp. 11080–11085, Nov. 2014, doi: 10.1021/nn504444g.

[18] G. J. D. & R. H. F. N. Tessler, “Lasing from conjugated polymer microcavities,” Nature, vol. 382, no. August, pp. 695–697, 1996.

[19] G. Canazza, F. Scotognella, G. Lanzani, S. De Silvestri, M. Zavelani-Rossi, and D. Comoretto, “Lasing from all-polymer microcavities,” Laser Phys. Lett., vol. 11, no. 3, p. 035804, Mar. 2014, doi: 10.1088/1612-2011/11/3/035804.

[20] A. J. C. Kuehne et al., “Sub-Micrometer Patterning of Amorphous- and β-Phase in a Crosslinkable Poly(9,9-dioctylfluorene): Dual-Wavelength Lasing from a Mixed-Morphology Device,” Adv. Funct. Mater., vol. 21, no. 13, pp. 2564–2570, Jul. 2011, doi: 10.1002/adfm.201002553.

[21] B. K. Yap, R. Xia, M. Campoy-Quiles, P. N. Stavrinou, and D. D. C. Bradley, “Simultaneous optimization of charge-carrier mobility and optical gain in semiconducting polymer films,” Nat. Mater., vol. 7, no. 5, pp. 376–380, 2008, doi: 10.1038/nmat2165.

[22] A. Rose, Z. Zhu, C. F. Madigan, T. M. Swager, and V. Bulović, “Sensitivity gains in chemosensing by lasing action in organic polymers,” Nature, vol. 434, no. 7035, pp. 876–879, Apr. 2005, doi: 10.1038/nature03438.

[23] S. Tang et al., “A Tunable Optofluidic Microlaser in a Photostable Conjugated Polymer,” Adv. Mater., vol. 30, no. 50, p. 1804556, Dec. 2018, doi: 10.1002/adma.201804556.

[24] S. Kushida, D. Okada, F. Sasaki, Z.-H. Lin, J.-S. Huang, and Y. Yamamoto, “Low-Threshold Whispering Gallery Mode Lasing from Self-Assembled Microspheres of Single-Sort Conjugated Polymers,” Adv. Opt. Mater., vol. 5, no. 10, p. 1700123, May 2017, doi: 10.1002/adom.201700123.

Chapter 7: Conclusion and Future Work

Organic semiconductors have been an attractive area of research due their ease of processability, flexibility and wavelength tunability. This has already been realised by the commercial success in OLED display technology. The high optical gain of organic semiconductors also makes them promising gain materials and over the past 60 years major breakthroughs have been made in the development of an electrically driven organic laser diode. A large majority of research has been focused on DFB gratings as the resonator structure. This thesis has investigated the ASE threshold for a range of organic semiconductor lasing materials for their potential for integration into a planar microcavity. From this, one of the lowest lasing polymer microcavities was achieved. The low-lasing threshold of the planar microcavity was reduced even further by enhancing confinement by implementing defect structures into the cavity.

In the first experimental chapter the ASE threshold was measured for a range of materials. First the pigment dye, Fluorescent Orange (FO), Anthra[2,1,9-def:6,5,10-d´e´f´] diisoquinoline1,3,8,10(2H,9H)-tetrone,2,9-bis[2,6-bis(1methylethyl)phenyl] was dispersed in an inert polystyrene (PS) matrix. Reducing the FO concentration relative to the PS matrix reduced the ASE threshold, the lowest being 259 μJ cm^{-2}. This is attributed to the increase in aggregation of the FO molecules that occurs at higher concentrations. The matrix was then change to PMMA where no ASE was observed. Co-thermal evaporation was then used with bathocuproine (BCP) as the matrix, effectively separating the FO, reducing the ASE threshold to 55 μJ cm^{-2}.

The next material investigated was the polymer polyfluorene 2, 7-(9,9-dioctylfluorene (PFO) that including binaphthyl (BN) spacer groups between the monomer units (BN-PFO). The relative concentration of BN spacer units to the PFO was altered (5.2%, 9.8% and 12.7%). Using low-temperature and GIWAXS measurements it was observed that the molecular disorder of the film was increased by increasing the BN spacer concentration. The lowest threshold observed was 19 μJ cm^{-2}, attributed to the enhanced disorder in the 12.7% BN-PFO. The last material studied was the small molecule 2,4'-Bis(4-(9H-carbazol-9-yl)styryl)biphenyl (BSBCz). This material was thermally evaporated as a neat film and produced the lowest ASE threshold of all the materials studied (14 μJ cm^{-2}).

The work in chapter 4 highlighted both the physical and optical properties for organic lasing materials. With this approach further understanding between the molecular packing and the ASE behaviour can be developed. Future studies should conduct GIWAXS measurements on thermally evaporated BCP:FO films in order to understand this more favourable molecular packing.

Planar microcavity lasers made with the two lowest ASE threshold materials (BN-PFO 12.7% and BSBCz) were then studied in Chapter 5. Both planar microcavities were optically pumped and produced deep blue lasing with BN-PFO and BSBCz having lasing wavelengths of 445 and 494 nm. Low threshold lasing was observed for each material, due to the high Q factor of the planar microcavity. Using BN-PFO (12.7%), one of the lowest thresholds for an organic polymer microcavity laser was reported (12 μJ cm^{-2}). The BSBCz microcavity produces the lowest lasing threshold of 1.5 μJ cm^{-2}.

The low-threshold lasing reported in this chapter emphasises the need for a wider study on organic microcavities. Further studies should expand these results with time-resolved measurements as both materials used here have been reported to show quasi-CW lasing in DFB gratings. Additionally, the BSBCz OLED design outlined at the end of the chapter should be integrated into the planar microcavity to characterise it under electrical operation.

In the final experimental chapter, Chapter 6, a laser patterning setup was developed to write defects into a PS film. Growing the BN-PFO planar microcavity over this structure, the total microcavity structure conformed to the profile of the defect. This gaussian shape defect within the cavity active layer added a refractive index difference in the lateral direction, enhancing the cavity confinement. The resulted in a high Q factor of 2300, further reducing the lasing threshold from 11 μJ cm^{-2} to 7 μJ cm^{-2}.

The laser patterning technique outlined in this chapter offers a simple and effective way to increase the confinement of a planar microcavity. An almost quadruple enhancement to the Q factor caused a further reduction to the lasing threshold. Further studies should apply the same technique to the BSBCz cavity with the potential to achieve the lowest lasing threshold for an organic microcavity laser.